

# Channel estimation techniques for next generation mobile communication systems

Author:

Kun Chen Hu

in partial fulfillment of the requirements for the degree of Doctor in  
Multimedia and Communication  
Universidad Carlos III de Madrid

Supervisor:

Ana García Armada

Leganés, July 2019



Esta tesis se distribuye bajo licencia “Creative Commons **Reconocimiento – No Comercial – Sin Obra Derivada**”



# Abstract

We are witnessing a revolution in wireless technology, where the society is demanding new services, such as smart cities, autonomous vehicles, augmented reality, etc. These challenging services not only are demanding an enormous increase of data rates in the range of 1000 times higher, but also they are real-time applications with an important delay constraint. Furthermore, an unprecedented number of different machine-type devices will be also connected to the network, known as Internet of Things (IoT), where they will be transmitting real-time measurements from different sensors. In this context, the Third Generation Partnership Project (3GPP) has already developed the new Fifth Generation (5G) of mobile communication systems, which should be capable of satisfying all the requirements. Hence, 5G will provide three key aspects, such as: enhanced mobile broad-band (eMBB) services, massive machine type communications (mMTC) and ultra reliable low latency communications (URLLC).

In order to accomplish all the mentioned requirements, it is important to develop new key radio technologies capable of exploiting the wireless environment with a higher efficiency. Orthogonal frequency division multiplexing (OFDM) is the most widely used waveform by the industry, however, it also exhibits high side lobes reducing considerably the spectral efficiency. Therefore, filter-bank multi-carrier combined with offset quadrature amplitude modulation (FBMC-OQAM) is a waveform candidate to replace OFDM due to the fact that it provides extremely low out-of-band emissions (OBE). The traditional spectrum frequencies range is close to saturation, thus, there is a need to exploit higher bands, such as millimeter waves (mm-Wave), making possible the deployment of ultra broad-band services. However, the high path loss in these bands increases the blockage probability of the radio-link, forcing us to use massive multiple-input multiple-output (MIMO) systems in order to increase either the diversity or capacity of the overall link.

All these emergent radio technologies can make 5G a reality. However, all their benefits can be only exploited under the knowledge and availability of the channel state information (CSI) in order to compensate the effects produced by the channel. The channel estimation process is a well known procedure in the area of signal processing for communications, where it is a challenging task due to

---

the fact that we have to obtain a good estimator, maintaining at the same time the efficiency and reduced complexity of the system and obtaining the results as fast as possible. In FBMC-OQAM, there are several proposed channel estimation techniques, however, all of them required a high number of operations in order to deal with the self-interference produced by the prototype filter, hence, increasing the complexity. The existing channel estimation and equalization techniques for massive MIMO are in general too complex due to the large number of antennas, where we must estimate the channel response of each antenna of the array and perform some prohibitive matrix inversions to obtain the equalizers. Besides, for the particular case of mm-Wave, the existing techniques either do not adapt well to the dynamic ranges of signal-to-noise ratio (SNR) scenarios or they assume some approximations which reduce the quality of the estimator.

In this thesis, we focus on the channel estimation for different emerging techniques that are capable of obtaining a better performance with a lower number of operations, suitable for low-complexity devices and for URLLC. Firstly, we proposed new pilot sequences for FBMC-OQAM enabling the use of a simple averaging process in order to obtain the CSI. We show that our technique outperforms the existing ones in terms of complexity and performance. Secondly, we propose an alternative low-complexity way of computing the precoding/postcoding equalizer under the scenario of massive MIMO, keeping the quality of the estimator. Finally, we propose a new channel estimation technique for massive MIMO for mm-Wave, capable of adapting to very variable scenarios in terms of SNR and outperforming the existing techniques. We provide some analysis of the mean squared error (MSE) and complexity of each proposed technique. Furthermore, some numerical results are given in order to provide a better understanding of the problem and solutions.



# Acknowledgment

The underlying work would have been impossible to complete without receiving support and help in a number of different ways.

First of all, I would like to express my sincere gratitude to my advisor Prof. Ana García Armada for the continuous support of my Ph.D study and research, for her extraordinary scientific guidance and for showing perpetual confidence in my skills. I could not have imagined having a better advisor and mentor for my Ph.D study.

Besides my advisor, I would like to thank the rest of my thesis committee for their encouragement, insightful comments and questions.

My sincere thanks also goes to Prof. Maria Julia Fernández-Getino García, Prof. Víctor P. Gil Jiménez, Prof. Dirk T. M. Slock and Dr. Raquel Pérez Leal, for providing their patience, motivation and a invaluable knowledge for my research.

I thank my fellow lab-mates Juan Carlos Estrada Jiménez and Borja Genovés Guzmán for the stimulating discussions, for the stressful days we were working together before deadlines, and for all the fun we have had in the last years.

Last but not the least, I would like to thank my family and friends supporting me spiritually throughout my life.

# Published contents

All the material from all the sources included in this thesis are singled out with typographic means and explicit references.

## Journal articles

- **K. Chen-Hu**, J. C. Estrada-Jiménez, M. J. F. García and A. G. Armada, "Continuous and Burst Pilot Sequences for Channel Estimation in FBMC-OQAM," in IEEE Transactions on Vehicular Technology, vol. 67, no. 10, pp. 9711-9720, Oct. 2018.  
DOI: 10.1109/TVT.2018.2861995  
URL: <http://ieeexplore.ieee.org/stamp/stamp.jsp?tp=&arnumber=8424058&isnumber=8492481>  
It is fully included in Chapter 4.
- J. C. Estrada-Jiménez, **K. Chen-Hu**, M. J. F. García and A. G. Armada, "Power allocation and capacity analysis for FBMC-OQAM with superimposed training," in IEEE Access, vol. 7, no. 1, pp. 46968-46976, May. 2019.  
DOI: 10.1109/ACCESS.2019.2909405  
URL: <https://ieeexplore.ieee.org/stamp/stamp.jsp?tp=&arnumber=8681505>  
It is mentioned in Chapter 3.

## Conference articles

- **K. Chen-Hu** and A. G. Armada, "Low-complexity computation of zero-forcing equalizers for massive MIMO-OFDM," 2019 IEEE 89th Vehicular Technology Conference (VTC-Spring), Kuala-Lampur, 2019, pp. 1-5.



---

DOI: Accepted

URL:

It is fully included in Chapter 5.

- **K. Chen-Hu**, D. T. M. Slock and A. G. Armada, "Low-Rank Channel Estimation for mm-Wave Multiple Antenna Systems using Joint Spatio-Temporal Covariance Matrix," 2019 IEEE International Conference on Communications Workshops (ICC Workshops): Workshop on Millimeter-Wave Communications for 5G and B5G, Shanghai, 2019, pp. 1-6.

DOI: Accepted

URL:

It is fully included in Chapter 6.

- **K. Chen-Hu** and A. G. Armada, "SINR analysis of OFDM and f-OFDM for machine type communications," 2016 IEEE 27th Annual International Symposium on Personal, Indoor, and Mobile Radio Communications (PIMRC), Valencia, 2016, pp. 1-6.

DOI: 10.1109/PIMRC.2016.7794702

URL: <http://ieeexplore.ieee.org/stamp/stamp.jsp?tp=&arnumber=7794702&isnumber=7794546>

It is mentioned in Chapter 2.

- **K. Chen-Hu**, R. P. Leal and A. G. Armada, "Reducing the Interference by Adapting the Power of OFDM for mMTC," 2018 IEEE 87th Vehicular Technology Conference (VTC Spring), Porto, 2018, pp. 1-5.

DOI: 10.1109/VTCSpring.2018.8417533

URL: <http://ieeexplore.ieee.org/stamp/stamp.jsp?tp=&arnumber=8417533&isnumber=8417457>

It is mentioned in Chapter 2.

- **K. Chen-Hu**, F. Kaltenberger and A. Garcia Armada, "Implementation and Measurement of Power Adapted-OFDM Using OpenAirInterface," 2018 IEEE 19th International Workshop on Signal Processing Advances in Wireless Communications (SPAWC), Kalamata, 2018, pp. 1-5.

DOI: 10.1109/SPAWC.2018.8445894

URL: <http://ieeexplore.ieee.org/stamp/stamp.jsp?tp=&arnumber=8445894&isnumber=8445765>

It is mentioned in Chapter 2.

- **K. Chen-Hu**, J. C. Estrada-Jimenez, M. J. F. Garcia and A. G. Armada, "Superimposed Training for Channel Estimation in FBMC-OQAM," 2017 IEEE 86th Vehicular Technology

---

Conference (VTC-Fall), Toronto, ON, 2017, pp. 1-5

DOI: 10.1109/VTCFall.2017.8287938

URL: <http://ieeexplore.ieee.org/stamp/stamp.jsp?tp=&arnumber=8287938&isnumber=8287863>

It is mentioned in Chapter 3.

- **K. Chen-Hu** and A. G. Armada, "Non-Coherent Multiuser Massive MIMO-OFDM with Differential Modulation," 2019 IEEE International Conference on Communications (ICC), Shanghai, 2019, pp. 1-6.

DOI: Accepted

URL:

It is mentioned in Chapter 3.

# Contents

<b>Contents</b>	<b>ix</b>
<b>List of Figures</b>	<b>xiii</b>
<b>List of Tables</b>	<b>xvii</b>
<b>List of Abbreviations</b>	<b>xix</b>
<b>List of Notations</b>	<b>xxiii</b>
<b>1 Introduction</b>	<b>1</b>
1.1 Motivation . . . . .	1
1.2 Contributions . . . . .	4
1.3 Thesis organization . . . . .	5
<b>2 Emerging techniques for mobile communications</b>	<b>7</b>
2.1 Waveform design . . . . .	8
2.1.1 FBMC-OQAM . . . . .	8
2.1.2 f-OFDM . . . . .	9
2.1.3 UFMC . . . . .	9
2.1.4 GFDM . . . . .	11
2.1.5 PA-OFDM . . . . .	12
2.2 Massive MIMO . . . . .	13
2.3 Millimeter wave for mobile communications . . . . .	14
<hr/>	
Channel estimation techniques for next generation mobile communication systems	ix

<b>3</b>	<b>Channel estimation for emerging techniques for mobile communications</b>	<b>17</b>
3.1	OFDM . . . . .	17
3.2	MIMO and massive MIMO combined with OFDM . . . . .	18
3.3	FBMC . . . . .	21
3.4	Millimeter wave . . . . .	22
3.5	Other approaches . . . . .	23
3.5.1	ST . . . . .	23
3.5.2	Non-coherent demodulation scheme . . . . .	24
3.6	System model . . . . .	25
3.7	Channel model . . . . .	26
<b>4</b>	<b>New pilot schemes for channel estimation in FBMC-OQAM</b>	<b>29</b>
4.1	System model . . . . .	30
4.1.1	FBMC-OQAM . . . . .	30
4.1.2	Effects of the channel in FBMC-OQAM . . . . .	32
4.2	Continuous pilot sequence (CPS) . . . . .	33
4.3	Burst pilot sequence (BPS) . . . . .	35
4.4	Channel equalization for CPS and BPS . . . . .	36
4.5	Analysis the of estimation error . . . . .	37
4.6	Analysis of the complexity . . . . .	39
4.7	Numerical results . . . . .	40
4.7.1	Simulation Parameters . . . . .	40
4.7.2	Definition of SNR . . . . .	41
4.7.3	Results . . . . .	41
4.8	Conclusions . . . . .	46
<b>5</b>	<b>Low-complexity channel estimation for massive MIMO-OFDM</b>	<b>47</b>
5.1	System model . . . . .	48
5.1.1	OFDM . . . . .	48
5.2	Channel estimation and equalization using linear interpolation . . . . .	49

---

5.2.1	Traditional scheme . . . . .	50
5.2.2	Proposed low-complexity schemes . . . . .	50
5.3	Asymptotic analysis of the average square euclidean distance (ASED) . . . . .	51
5.4	Analysis of the complexity . . . . .	52
5.5	Numerical results . . . . .	52
5.5.1	Verification of the theoretical analysis of the ASED . . . . .	53
5.5.2	Verification of the complexity . . . . .	53
5.5.3	Performance comparison . . . . .	54
5.6	Conclusions . . . . .	56
<b>6</b>	<b>Low-rank channel estimation for mmWave</b>	<b>57</b>
6.1	System model . . . . .	58
6.2	Estimation of the joint ST covariance matrix . . . . .	59
6.3	Estimation of DoA and ToA . . . . .	60
6.3.1	MUSIC-1D method . . . . .	61
6.3.2	Iterative MLE method . . . . .	62
6.3.3	Hybrid method . . . . .	64
6.4	Automatic-rank selector (ARS) . . . . .	66
6.5	Numerical results . . . . .	68
6.5.1	Simulation parameters . . . . .	68
6.5.2	Results and discussion . . . . .	69
6.6	Conclusions . . . . .	73
<b>7</b>	<b>Conclusions</b>	<b>75</b>
7.1	Conclusions . . . . .	75
7.2	Future work . . . . .	76
	<b>Bibliography</b>	<b>79</b>



# List of Figures

1.1	New services in 5G. . . . .	2
1.2	Prototype of massive MIMO equipped with 128 antennas at University of Lund. . .	3
1.3	Frequency bands usage in 5G. . . . .	4
2.1	OBE comparison among different waveform candidates. . . . .	8
2.2	Issues related to the use of FIR filter. . . . .	10
2.3	Block diagram of UFMC. . . . .	10
2.4	Block diagram of GFDM. . . . .	11
2.5	Frame comparison between OFDM and GFDM. . . . .	11
2.6	Comparative of scheduling schemes. . . . .	12
2.7	Mockup. . . . .	13
2.8	mmWave scenario. . . . .	15
3.1	Example of pilot transmission in MIMO-OFDM for DL (two antennas at BS) or UL (two UEs). . . . .	19
3.2	Example of pilot contamination. . . . .	20
3.3	MU-MIMO scenario. . . . .	26
3.4	Example of wireless propagation environment . . . . .	26
3.5	Example of wireless propagation environment . . . . .	27
4.1	Transmitter baseband model of FBMC-OQAM. . . . .	32
4.2	Receiver baseband model of FBMC-OQAM. . . . .	32
4.3	Layout of the pilot symbols in the time-frequency grid. . . . .	36

*LIST OF FIGURES*

---

4.4	MSE comparative of AP and CPS for different values of $N_g$ and $7 \times 10^3$ channel realizations without any Doppler effects. . . . .	42
4.5	SER comparative of AP and CPS for different values of $N_g$ and $7 \times 10^3$ channel realizations without any Doppler effects. . . . .	43
4.6	SER comparative of AP, CPS and BPS with $\nu = 0.5$ and $7 \times 10^3$ channel realizations without any Doppler effects. . . . .	43
4.7	SER comparative of AP, CPS and BPS under CFO effects with $\epsilon = 0.04, \nu = 0.5$ and $7 \times 10^3$ channel realizations without any Doppler effects. . . . .	44
4.8	SER comparative of AP, CPS and BPS with $\nu = 0.5$ in the presence of 100Hz Doppler frequency. . . . .	44
4.9	SER comparative of CPS and BPS in the presence of 100Hz Doppler frequency. . .	45
4.10	SER comparative of CPS and BPS with $N_g = 14$ in the presence of 5KHz Doppler frequency. . . . .	45
5.1	ASED between traditional scheme and low-complexity schemes for $N_u = 2, 4$ and 8 when $\Delta \mathbf{H}_k = \mathbf{0}_{N_v \times N_u}$ . . . . .	54
5.2	Comparison of complexity in terms of NCM for $K_p = 8$ and $N_u = 2$ and 8. . . . .	54
5.3	SER performance results for $\sigma_{\Delta \mathbf{H}}^2 = \sigma_w^2$ and $N_v = 10$ . . . . .	55
5.4	SINR performance results for $\sigma_{\Delta \mathbf{H}}^2 = \sigma_w^2$ and $N_v = 10$ . . . . .	55
5.5	SINR performance results for $\sigma_{\Delta \mathbf{H}}^2 = \sigma_w^2$ and $N_v = 100$ . . . . .	56
6.1	Multiple antenna scenario. . . . .	58
6.2	Multiple antenna scenario. . . . .	59
6.3	MUSIC 1D algorithm. . . . .	63
6.4	Iterative MLE algorithm. . . . .	65
6.5	Accelerated search algorithm. . . . .	66
6.6	ARS algorithm. . . . .	68
6.7	MSE of MUSIC-1D algorithm. . . . .	70
6.8	MSE of iterative MLE algorithm. . . . .	70
6.9	MSE of hybrid algorithm. . . . .	71
6.10	Comparison of the MSE among FR and LR estimated channel using $\mathbf{S}$ and $\hat{\mathbf{S}}$ . . . .	71
6.11	Comparison of the MSE between our proposal and the reference. . . . .	72



6.12 Comparison of the MSE among simulation and theoretical analysis results for FR and LR assuming perfect $\mathbf{S}$ . . . . .	72
6.13 MSE of the ARS algorithm. . . . .	73



# List of Tables

2.1	Requirements for 5G. . . . .	7
4.1	Intrinsic interference caused to data placed at $[\mathbf{\Gamma}]_{k_0, m_0}$ using the PHYDYAS prototype filter. . . . .	34
4.2	Number of real operations per subcarrier. . . . .	40
4.3	Simulation parameters for CPS and BPS. . . . .	41
5.1	Comparison of the complexity in terms of NCM . . . . .	52
5.2	Simulation parameters for low-complexity ZF equalization. . . . .	53
6.1	Simulation parameters for LR channel estimation. . . . .	69
6.2	PDP . . . . .	69



# List of abbreviations

<b>3GPP</b>	Third Generation Partnership Project
<b>4G</b>	Fourth Generation of broadband mobile communication system
<b>5G</b>	Fifth Generation of broadband mobile communication system
<b>AFB</b>	Analysis Filter-Bank
<b>AP</b>	Auxiliary Pilot
<b>ARS</b>	Automatic-Rank Selector
<b>ASED</b>	Average Square Euclidean Distance
<b>ASK</b>	Amplitude Shift Keying
<b>AWGN</b>	Additive White Gaussian Noise
<b>BPS</b>	Burst Pilot Sequence
<b>BS</b>	Base Station
<b>CDF</b>	Cummulative Distribution Function
<b>CDL</b>	Clustered Delay Line
<b>CFO</b>	Carrier Frequency Offset
<b>CLT</b>	Central Limit Theorem
<b>CP</b>	Cyclic Prefix
<b>CPP</b>	Composite Pilot Pair
<b>CPS</b>	Continuous Pilot Sequence
<b>CSI</b>	Channel State Information
<b>DDP</b>	Dual-Dependant Pilot
<b>DNS</b>	Diagonal Neumann Series
<b>DPSK</b>	Differential Phase Shift Keying
<b>DL</b>	Down-Link
<b>DVB-T</b>	Digital Video Broadcasting - Terrestrial

<b>eNB</b>	Evolved Node B
<b>EPA</b>	Extended Pedestrian A
<b>EPC</b>	Evolved Packet Core
<b>ETU</b>	Extended Typical Urban
<b>EVA</b>	Extended Vehicular A
<b>EVM</b>	Error Vector Magnitude
<b>FBMC</b>	Filter-Bank Multi-Carrier
<b>FDD</b>	Frequency Division Duplex
<b>FDS</b>	Frequency Domain Scheme
<b>FFT</b>	Fast Fourier Transform
<b>FIR</b>	Finite Impuse Response
<b>f-OFDM</b>	filtered-Orthogonal Frequency Division Multiplexing
<b>GFDM</b>	Generalized Frequency Division Multiplexing
<b>GJ</b>	Gauss Jordan
<b>IDPOP</b>	Interference-Dependant Pair Of Pilots
<b>IFFT</b>	Inverse Fast Fourier Transform
<b>IoT</b>	Internet of Things
<b>ISI</b>	Inter-Symbol Interference
<b>LS</b>	Least Square
<b>LZF</b>	Low-complexity Zero-Forcing
<b>LTE</b>	Long Term Evolution
<b>MIMO</b>	Multiple Input Multiple Output
<b>ML</b>	Maximum Likelihood
<b>MMSE</b>	Minimum Mean Square Error
<b>mMTC</b>	massive Machine Type Communications
<b>mmWave</b>	Millimeter Wave
<b>MRC</b>	Maximum ratio combining
<b>MSE</b>	Mean Square Error
<b>NB</b>	Narrow-Band
<b>NCM</b>	Number of Complex Multiplication
<b>NR</b>	New Radio
<b>NS</b>	Neumann Series

<b>OBE</b>	Out-of-Band Emission
<b>OAI</b>	Open Air Interface
<b>OFDM</b>	Orthogonal Frequency Division Multiplexing
<b>OQAM</b>	Offset Quadrature Amplitude Modulation
<b>PA</b>	Power Adapted
<b>PAPR</b>	Peak-to-Average Power Ratio
<b>PDF</b>	Probability Density Function
<b>PDP</b>	Power Delay Profile
<b>POP</b>	Pilot Of Pilots
<b>PSAM</b>	Pilot Symbol Assisted Modulation
<b>RB</b>	Resource Block
<b>RF</b>	Radio Frequency
<b>SER</b>	Symbol Error Rate
<b>SFB</b>	Synthesis Filter-Bank
<b>SIC</b>	Successive Interference Cancellation
<b>SNR</b>	Signal to Noise Ratio
<b>SINR</b>	Signal to Interference plus Noise Ratio
<b>SISO</b>	Single Input Single Output
<b>SIMO</b>	Single Input Multiple Output
<b>SC-FDMA</b>	Single Carrier-Frequency Division Multiple Access
<b>TDD</b>	Time Division Duplex
<b>TDL</b>	Tapped Delay Line
<b>TDS</b>	Time Domain Scheme
<b>TNS</b>	Tri-diagonal Neumann Series
<b>UE</b>	User Equipment
<b>UFMC</b>	Universal Filtered Multi-Carrier
<b>UL</b>	Up-Link
<b>URLLC</b>	Ultra Reliable Low Latency Communications
<b>ZF</b>	Zero Forcing





# List of notations

$a$	scalar
$\mathbf{a}$	vector
$\mathbf{A}$	matrix
$[\mathbf{a}]_n$	the $n$ -th element of $\mathbf{a}$
$[\mathbf{A}]_{m,n}$	the $m$ -th row and $n$ -th column element of $\mathbf{A}$
$\mathbf{A}^H$	Hermitian of $\mathbf{A}$
$\mathbf{A}^T$	transpose of $\mathbf{A}$
$\mathbf{A}^*$	conjugate of $\mathbf{A}$
$\mathbf{A}^\dagger$	pseudo-inverse of $\mathbf{A}$
$\det(\mathbf{A})$	determinant of $\mathbf{A}$
$\text{adj}(\mathbf{A})$	adjugate matrix of $\mathbf{A}$
$\text{tr}(\mathbf{A})$	trace of $\mathbf{A}$
$\text{diag}(\mathbf{A})$	vector of diagonal elements of $\mathbf{A}$
$\text{diag}(\mathbf{a})$	matrix whose of diagonal elements correspond to $\mathbf{a}$
$\mathbf{I}_M$	identity matrix of size $(M \times M)$
$\mathbf{0}_{M \times N}$	zero matrix of size $(M \times N)$
$\mathbf{1}_{M \times N}$	one matrix of size $(M \times N)$
$\otimes$	Kronecker product
$\odot$	Khatri-Rao product
$\circ$	Hadamard product
$*$	convolution operation

$\text{Re}\{\cdot\}$	real part
$\text{Im}\{\cdot\}$	imaginary part
$\mathcal{CN}(\mu, \sigma^2)$	circularly-symmetric complex normal distribution with mean $\mu$ and variance $\sigma^2$
$\mathbb{E}\{\cdot\}$	expected value
$\text{Var}\{\cdot\}$	variance
$\mathbb{E}_N\{\cdot\}$	average value over $N$ elements
$\ \cdot\ _F^2$	squared Frobenius norm
$[\mathbf{a}]_{\downarrow\alpha}$	downsampling by decimation factor $\alpha$

# Chapter 1

## Introduction

The vertiginous deployment of mobile communications has drastically changed our way of living and our habits. Several decades ago, nobody could think that today with our handset we are able to be connected to our relatives with a simple call or some text messages, we are also capable of determining our geographic location with a great accuracy, or we can look for any information of our interest anywhere and anytime. All these benefits have brought to the humanity a great value and easiness, as a consequence of constant evolution of the mobile communications. Nowadays, the Fourth Generation (4G) of mobile communications [1] is already providing a great coverage all over the world, however, a new Fifth Generation (5G) [2] is being developed in order to take us to explore new wireless experiences and open new frontiers.

### 1.1 Motivation

We are witnessing a revolution in wireless technology, where the society is demanding new services, such as: smart cities, autonomous vehicles, augmented reality, etc. These challenging services not only are demanding an enormous increase of data rates in the range of 1000 times higher, but also they are real-time applications with an important delay constraint. Furthermore, an unprecedented number of different machine-type devices will be also connected to the network, known as Internet of Things (IoT), where they will be transmitting real-time measurements from different sensors. The Third Generation Partnership Project (3GPP) has already identified these requirements, and it has classified them into three groups: enhanced mobile broad-band (eMBB) services, massive machine type communications (mMTC) and ultra reliable low latency communications (URLLC) (see Fig. 1.1 [3]).

As a transitory solution, the 3GPP has modified the existing 4G, known as Long Term Evolu-

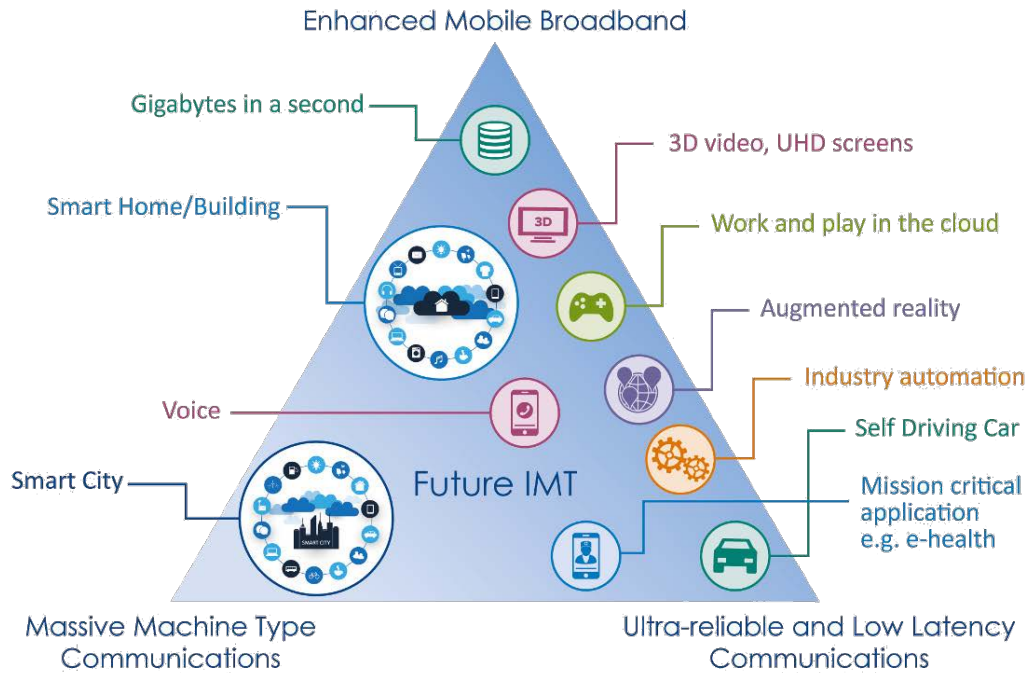


Figure 1.1: New services in 5G.

tion (LTE) [1], in order to satisfy, as far as possible, the mentioned demands of the users. Carrier aggregation was introduced to increase the data rate up to 100MHz, where different LTE bands can be jointly used as a single one. Later, it proposed to integrate MTC in LTE, known as NarrowBand-IoT (NB-IoT), placing the narrow-band signal in either the middle or the edge of the band. However, all these minor modifications hardly cover the high expectation of the society.

The new promising 5G [2] will be capable of providing all the requested services with a great performance. In the first stage, the 3GPP has recently defined a New Radio (NR) [2], satisfying only the eMBB services, leaving the other two goals for the following releases. Focusing in the physical layer, some key technologies that will make possible all these requirements are: new waveform design, massive multiple-input multiple-output (MIMO) and millimeter waves (mmWave).

Currently, orthogonal frequency division multiplexing (OFDM) [4] is the waveform candidate adopted for NR in the first release. Despite its advantages such as robustness against multipath fading and ease of implementation, it also has severe drawbacks, such as: high peak-to-average power ratio (PAPR) and high side lobes in frequency domain, among others. Given these drawbacks, there exists a need to find a new waveform candidate capable of fulfilling all the 5G requirements for its evolution. Additionally, the industry expects that the new waveform can-

didate could be as far as possible similar to OFDM in order to keep the backward compatibility. Several new waveforms have already been proposed for 5G, such as: filter-bank multi-carrier combined with offset quadrature amplitude modulation (FBMC-OQAM), generalized frequency division multiplexing (GFDM), universal filtered multi-carrier (UFMC), filtered-OFDM (f-OFDM), power adapted-OFDM (PA-OFDM), etc. The main objective of all these modulations is to reduce the out-of-band emissions (OBE) and take advantage of those gap bands either allowing narrow-band communication to be carried out in the resources left unused, or increasing the frequency spectrum used by the own signal by reducing the guard-bands.

MIMO [5] is a well-known technique based on either transmission or reception of signals using multiple antennas. With this technique, we are capable of obtaining multiplexing and diversity gain, improving the capacity and performance of the overall link as the number of antennas is increased. Therefore, massive MIMO [6] has been proposed for 5G, not only due to the significant increase of all the benefits that we have just mentioned, but also it allows a great reduction of complexity by making the sub-optimal precoding/postcoding techniques have approached the performance of the optimal one. Note that, the number of antennas at the base station (BS) has been increased from eight antennas to thirty two [2], and it will keep increasing in the future releases as we see in Fig. 1.2.



Figure 1.2: Prototype of massive MIMO equipped with 128 antennas at University of Lund.

The traditional radio spectrum is close to saturation, thus, the increase of available bandwidth for transmission will necessarily imply exploring new bands. Therefore, 5G [7] will use two key frequency ranges to support heterogeneous services (see Fig. 1.3 [8]). The first band corresponds

to the frequencies below 6GHz, whose objective is to provide a full coverage in urban, suburban, and rural areas; and to support massive MTC and transportation services. The second band corresponds to the spectrum above 6GHz, known as mmWave [9], which will be used to provide ultra high broad-band services. However, the transmission at these bands suffers from new physical effects that were not so severe in the traditional low-frequency bands, such as a significantly higher path loss and susceptibility to blockage, among others. Therefore, MIMO technique is a must in order to compensate these effects improving the coverage as mentioned before.

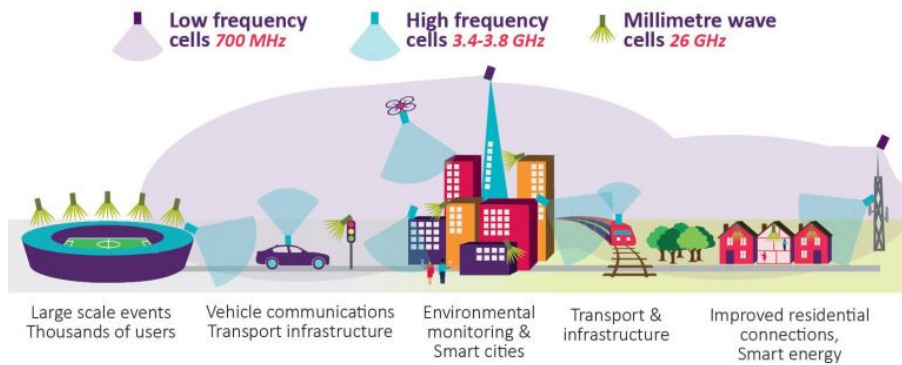


Figure 1.3: Frequency bands usage in 5G.

These challenging technologies require new signal processing techniques in order to allow a successful demodulation of the transmitted information. Often, the traditional ones cannot be straightforwardly applied, as for example for time-frequency estimation, channel estimation, hardware calibration, etc. New developments are needed to make possible the deployment of 5G.

## 1.2 Contributions

In this thesis, we mainly focus on the channel estimation process using preamble or pilot-based estimation for the different adopted technologies in 5G. The contributions are:

- Understanding of the environment of the evolution from 4G [1] to the NR of 5G [2]. In [10], we studied the new requirements of the society and we performed the integration of MTC over the guard-bands of the existing LTE signal using the new waveform f-OFDM. In [11], we proposed a new waveform in order to replace the f-OFDM, which has the same capability of reducing the OBE and avoiding the interference enhancement. Furthermore, in [12], we also implemented a testbed in order to verify our analytical results.
- FBMC-OQAM is a waveform candidate that can be considered in the future releases of 5G, due to the fact that it has the lowest OBE among others. In [13], we propose some

novel channel-adaptable pilot sequences and a new channel estimation method which has a lower complexity and better performance than the existing techniques, which is suitable for low-cost battery powered devices and/or low-latency communications.

- MIMO-OFDM is a very well-known combination which is already adopted by different communication standards. In [14] we propose an alternative way of computing the precoding/postcoding matrices for very large number of antennas, capable of significantly reducing the overall complexity and keeping a good performance at the same time.
- mmWave combined with very large MIMO system is challenging. In order to demodulate the signal, channel estimation is needed to be performed before the equalization. In [15], we propose a low-rank channel estimation method using a subspace method with the assumption of a non-parametric approach for the antenna array response at the BS, where channel calibration is no longer needed. Our proposal outperforms the existing techniques in terms of quality of the estimators.
- Additionally we also explored some alternative channel estimation techniques. In [16], we combined the FBMC-OQAM with superimposed training (ST), where we also analyzed its capacity in [17] against the well-known OFDM; and in [18], we used a non-coherent detection technique avoiding the channel estimation process for massive MIMO-OFDM.

### 1.3 Thesis organization

The present thesis is organized as follows:

- In Chapter 2, a detailed description of the different new techniques to be adopted in 5G is provided.
- In Chapter 3, we describe the state of the art related to channel estimation methods for different key technologies for 5G, and a general signal and channel model.
- In Chapter 4, we propose new pilot sequences and a low-complexity estimation method for FBMC-OQAM under both slow and fast-varying channel models.
- In Chapter 5, a low-complexity channel estimation and equalization technique for massive MIMO-OFDM is introduced.
- In Chapter 6, a novel low-rank channel estimation technique for mmWave scenario is provided.
- In Chapter 7, some conclusions and future work are pointed out.





## Chapter 2

# Emerging techniques for mobile communications

The new generation of mobile communications will provide a huge technical improvement in terms of speed, latency, mobility, etc. (see Table 2.1 [19]). All these features are possible thanks to the new adopted radio technologies mentioned in the previous chapter. In this chapter, we describe each technique pointing out their strengths and how to fight against their weaknesses, as they have been analyzed by the scientific community and the industry.

Table 2.1: Requirements for 5G.

Capability	5G target	Usage scenario
Peak data rate	20Gbit/s	eMBB
User experienced data rate	1Gbit/s	eMBB
Latency	1ms	URLLC
Mobility	500 km/h	eMBB/URLLC
Connection density	$10^6/\text{km}^2$	mMTC
Battery life	10 years	mMTC
Spectrum efficiency	3-4 x 4G	eMBB
Area traffic capacity	1000 Mbps/m <sup>2</sup>	eMBB

## 2.1 Waveform design

OFDM [4] is the traditional waveform adopted in many communication standards, such as: Digital Video Broadcasting-Terrestrial (DVB-T) [20], WiMax [21], Wi-Fi [22], 4G [1] and 5G [2]; which is capable of elegantly combating the frequency selective channels and improving the spectrum efficiency. However, it poses several limitations, such as high PAPR and OBE.

Focusing on the OBE aspect, OFDM is a multi-carrier waveform whose prototype filter is a rectangular one. Thanks to this feature, OFDM can be easily implemented by a fast Fourier transform (FFT). However, the rectangular filter in the frequency domain corresponds to a "sinc" function which possesses several high side lobes, responsible of causing the undesirable OBE. For example, LTE [23] must leave 10% of the spectrum as guard-band in order to avoid interfering the adjacent bands. Indubitably, this corresponds to a reduction of efficiency by wasting the precious frequency resources, which should be solved using a better waveform in the future releases.

Both the industry and the scientific community have dedicated a significant effort in order to find out a new waveform candidate capable of replacing OFDM in order to reduce the OBE. Several proposals are: FBMC-OQAM [24], f-OFDM [25], UFMC [26], GFDM [27], etc. (see Fig. 2.1 [25]). In the following subsections, we provide more details for all of them.

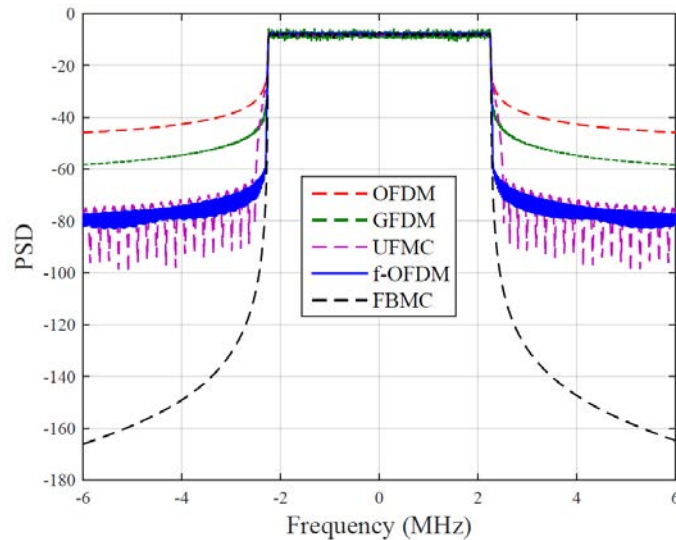


Figure 2.1: OBE comparison among different waveform candidates.

### 2.1.1 FBMC-OQAM

FBMC-OQAM [24] is the waveform candidate with the lowest OBE due to the use of a well-designed prototype filter, instead of using the rectangular one by OFDM. Therefore, FBMC-

OQAM can make a better use of the available spectrum, and allows to significantly reduce the existing guard-bands. Furthermore, it does not use the cyclic prefix (CP), increasing the time efficiency.

However, FBMC-OQAM has some disadvantages, such as: higher complexity in the transmitter and receiver blocks, the orthogonality only holds in the real domain and the presence of inter-symbol interference (ISI) and inter-carrier interference (ICI) due to the lack of CP [28]. Hence, any existing signal processing techniques designed for OFDM cannot be straightforwardly applied in FBMC-OQAM, where the new methods must deal with all the mentioned drawbacks. Note that, a detailed description of FBMC-OQAM is given in Chapter 4.

### 2.1.2 f-OFDM

One of the most appealing waveform candidates is f-OFDM [25], due to the fact that it is fully backward compatible with the current OFDM system. Unlike FBMC-OQAM, this candidate only needs an additional digital filter after the OFDM signal processing chain, capable of reducing the OBE of the entire broad-band signal. Hence, this is a low-complexity solution and it is suitable for the down-link (DL) scenario of mobile communication systems.

However, the use of the filter increases the ISI and the length of the CP should be increased in order to mitigate this effect (see Fig. 2.2a [25]). Thus, we are increasing the frequency efficiency by the reduction of time efficiency. An alternative way of avoiding the negative effect of ISI, without increasing the length of the CP, consists in the reduction of the length (order) of the filter. However, the order reduction implies an extra attenuation in the edge subcarriers of the signal (see Fig. 2.2b), causing their deterioration in terms of performance. Therefore, a good choice of the filter is crucial in the operations of f-OFDM waveform.

In order to provide a better understanding of this proposal and under the need of integrating the MTC signal with the existing LTE network, in [10], we performed a detailed study of the coexistence of these two signals (MTC and LTE). The interference is analyzed for both types of signals and the expression of the signal to interference plus noise ratio (SINR) is found allowing us to compare the behavior of OFDM and f-OFDM in these circumstances, where the latter provides a lower OBE enabling the integration of MTC in the guard-bands of LTE.

### 2.1.3 UFMC

Instead of filtering the entire band or changing the prototype filter of each subcarrier, UFMC [26] is a waveform candidate which filters sub-bands of the signal (see Fig. 2.3 [26]). This solution trades off between OBE and complexity reduction of FBMC-OQAM and f-OFDM. Furthermore,

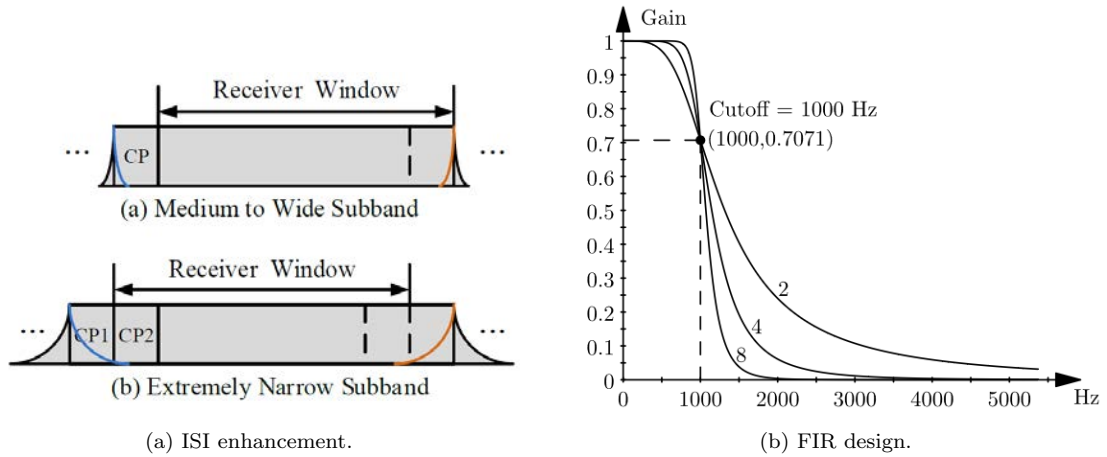


Figure 2.2: Issues related to the use of FIR filter.

this candidate is capable of keeping the backward compatibility for the up-link (UL) scenario of mobile communication systems. For example, in LTE, the entire band is split in several resource blocks (RB) which correspond with 12 subcarriers each. Each user equipment (UE) only transmits in those RBs scheduled by the BS. Hence, before transmission, each RB is filtered by a tunable filter capable of reducing the OBE of each RB.

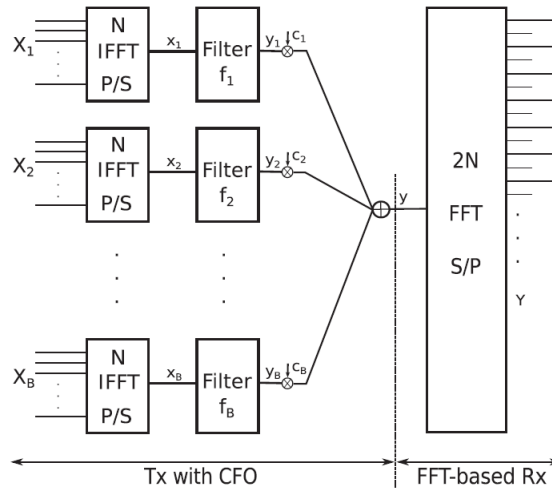


Figure 2.3: Block diagram of UFMC.

The main drawback of UFMC is not only the design of the bank of filters, which is very important to keep the overall performance, similar to f-OFDM; but also the presence of transient intervals of the filters force us to omit the CP (appearance of ISI and ICI) and double the number of points of the FFT at the receiver, in order to obtain the full transmitted signal.

### 2.1.4 GFDM

GFDM [27] is also a filtered waveform candidate which is very similar to FBMC-OQAM. However, unlike FBMC-OQAM, GFDM performs a circular convolution (see Fig. 2.4 [27]) instead of a linear one. Thanks to the circular convolution, it removes the prototype filter transient intervals, making possible that a continuous data stream can be split into blocks of data and a CP can be added in order to mitigate the ISI effects. If we compare GFDM with OFDM, GFDM is more efficient than OFDM due to the fact that there are less CP blocks (see Fig. 2.5).

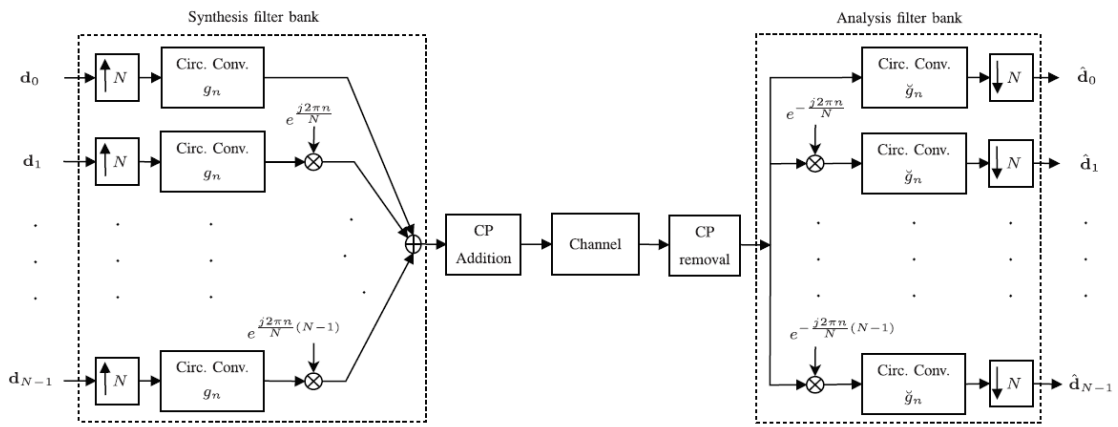


Figure 2.4: Block diagram of GFDM.

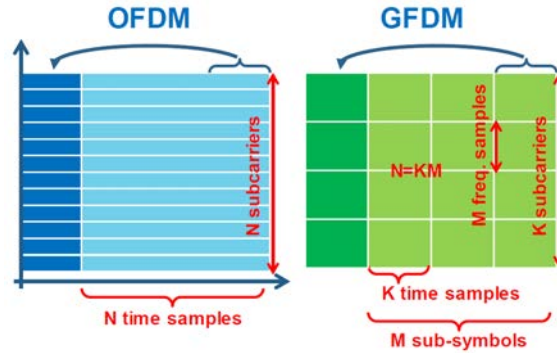


Figure 2.5: Frame comparison between OFDM and GFDM.

The advantages of GFDM come at the expense of an increase error rate compared with the well-known OFDM. This degradation is due to the fact that it is a non-orthogonal waveform, causing an ISI and ICI. Consequently, non-orthogonality of the neighboring subcarriers and time slots results in self-interference, increasing the complexity of the equalization stage.

### 2.1.5 PA-OFDM

We propose power adapted-OFDM (PA-OFDM) [11] as an alternative of f-OFDM which is capable of reducing the OBE, keeping the backward compatibility and avoiding the ISI enhancement. Our new technique consists in adapting the power of the OFDM signal with a spectral mask, which is dynamically designed by the scheduler according to the demanded rates and the channel quality of the served UEs. The scheduler will allocate the edge subcarriers to those users that require a lower power. Therefore, the undesirable OBE are reduced while the performance is guaranteed.

In Fig. 2.6, we show an example of scheduling. A traditional scheduling scheme is plotted in Fig. 2.6a, where all UEs are allocated with the same power. Fig. 2.6b provides the result of executing our proposed method, where the scheduler will consider the SINR of the UEs in order to perform the resource allocation and power optimization to decrease the OBE and fulfill their data rate requirements.

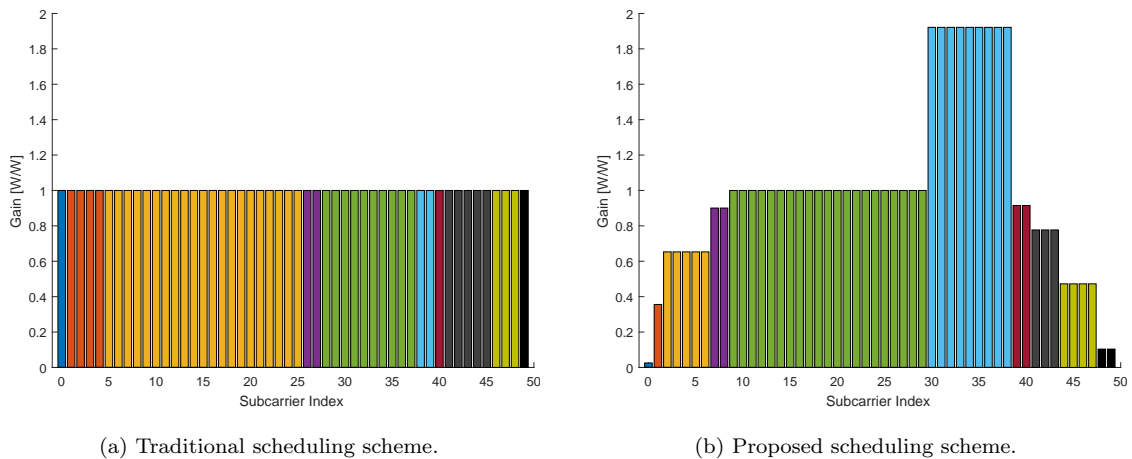


Figure 2.6: Comparative of scheduling schemes.

Additionally, we tested our proposed technique in a mock-up (see Fig. 2.7 [12]), where we implemented a fully compliant LTE 5MHz signal with our PA-OFDM scheme (denoted as evolved-LTE), using an open source platform Open Air Interface (OAI), which is capable of implementing a realistic Evolved Packet Core (EPC) and an Evolved Node B (eNB). In order to check the backward compatibility, we established a connection between our BS and a commercial UE, we verified that the UE is able to connect to Internet. Later, in order to check the reduction of OBE, we also placed a NB-IoT signal implemented using LabVIEW in the guard-band of the LTE signal. When PA-OFDM is enabled, the performance of the NB-IoT signal is much better in terms of error vector magnitude (EVM) and symbol error rate (SER).

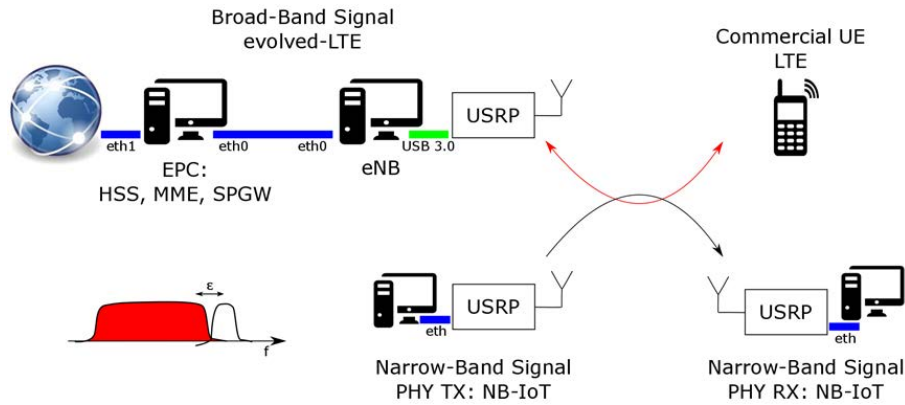


Figure 2.7: Mockup.

## 2.2 Massive MIMO

MIMO [5] is a popular radio technique that has also been widely included in several wireless standards during the last decades, as OFDM, where it can significantly increase the capacity and reliability of the radio links. In a realistic scenario, MIMO is exploited under the multi-user scenario, where typically the BS is equipped with multiple antennas that simultaneously serve a group of single-antenna UEs. Hence, multiplexing gain can be shared by all of them. In order to fully exploit its advantages, precoding/postcoding matrices must be computed in order to compensate some undesirable effects such as: noise, multi-user interference, hardware and channel effects, among others. However, in order to be able to compute these matrices, a channel estimation process is required, where the complexity of this process linearly depends on the number of antennas.

Last years, multi-user massive MIMO is proposed [6], where the number of antennas at BS is increased far beyond the actual usage. The random matrix theory [29] shows that the effects of small-scale fading, interference and noise can be effectively suppressed when the number of antennas is very large. Hence, using linear detection schemes, such as maximum ratio combining (MRC), will provide an optimal performance. However, when the number of antennas is not large enough, equalizers based on zero-forcing (ZF) or minimum mean square error (MMSE) criterion must be used in order to keep the performance. However, these equalizers require a matrix inversion which is a very hard operation in terms of complexity, increasing the delay of the link. Furthermore, channel estimation is also a challenging task when the number of antennas is very large, due to high number of different channels that must be estimated. This fact requires a long training period, where the BS and the UEs must exchange a great amount of pilot-sequences, decreasing the overall efficiency of the system.

## 2.3 Millimeter wave for mobile communications

The next generation of mobile communication networks should bring us an ambitious throughput. In order to meet this demanding requirement, new spectrum bands that have not been used yet by mobile communications must be explored, such as mmWave band. This band corresponds to frequencies higher than 30GHz, whose wavelengths belong to the order of millimeters. In the frame of 5G it is usual to refer to frequencies "below 6GHz" as conventional and "above 6GHz" when referring to the mmWave. The availability of resources at such high frequencies will provide ultra-high broad-band services. However, it also causes new challenges which will reduce the overall performance. These new issues are mainly related to the high propagation loss and the high probability of blockage from different materials that may contribute to the propagation channel.

In order to solve all the issues that we mentioned, very large number of antennas is a must in order to provide directional communications. Note that in mmWave, large antenna arrays can be easily manufactured due to the small wavelengths. Directional links will take advantage of the beam-forming gain in order to improve the link budget and provide an acceptable communication quality. However, it additionally requires a fine alignment of the beams among the BS and UEs. The process of seeking the best beam for either BS or UEs is known as beam management [30]. In Fig. 2.8 [31], we provide an example where the BS transmits some synchronization sequences using some beams with predefined directions and time slots. Each UE measures the received energy of each transmitted beam and they feed their best beam back to the BS. Then, the same process is performed again exchanging the roles among BS and UEs in order to seek the best beams for each UE. Once discovered the initial beams for each element of the network, a radio link can be established. However, these beams only correspond to a coarse estimation of the relative location among the BS and UEs. Later, the channel estimation process is not only needed in order to perform the precoding/postcoding equalization, but also it is required to improve the direction of the beams. Furthermore, if any UE is moving, a continuous location tracking is crucial in the overall performance of the link.

Moreover, another limitation in massive MIMO is related to the radio-frequency (RF) chains. Traditionally, there is one RF chain for each antenna of the array. However, under the scenario of very large number of antennas implies a high number RF chains, which is not feasible due to the increase of the cost and energy consumption. Recently, a promising solution to this issue corresponds to the concept of hybrid transceivers [32], which use of the combination of analog phase shifters in the RF domain with digital precoding/postcoding in the baseband, connected to a smaller number of RF chains.



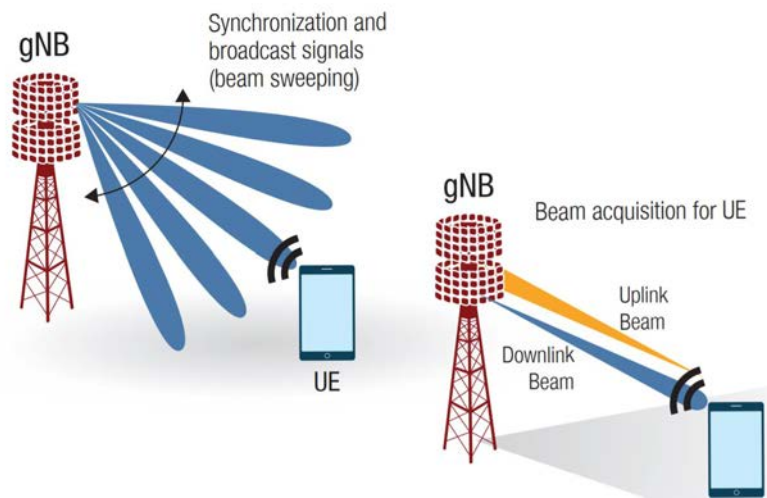


Figure 2.8: mmWave scenario.



## Chapter 3

# Channel estimation for emerging techniques for mobile communications

In coherent demodulation schemes, channel estimation and equalization represent two key aspects in wireless communication systems. The channel estimation procedure allows us to know how is the propagation environment of our transmitted signal, and then, compensate its effects by equalization, which is crucial for achieving reliable communication with high data rates.

In order to obtain the channel state information (CSI), the most used method is based on pilot symbol assisted modulation (PSAM), where the transmitter exclusively sends a known preamble or pilot-sequences, and the receiver can obtain the CSI through some minimization criterion, such as least squares (LS) or MMSE. These methods have some significant advantages, namely small error and low-complexity. However, the transmission of pilot sequences reduces the overall efficiency of the system. Moreover, note that there are also some alternatives to PSAM, which will be briefly described later.

In this chapter, we will provide a general overview of channel estimation methods used in the different radio technologies that we mentioned in the previous chapter.

### 3.1 OFDM

In OFDM, there are two alternatives for PSAM scheme: preamble-based or scattered-pattern based. The former case transmits a known preamble sequence before the data, which typically

is not only used for obtaining the CSI, but also it is used for time-frequency synchronization. In the latter case, the pilot symbols are placed over time-frequency resources following a scattered-pattern in order to increase the efficiency of the frame. Focusing on the second case, according to [33], the number of recommended pilots placed in the frequency domain should be around the double of the number of taps of the channel, and they must be equally spaced in order to fully characterize its selectivity. In the time domain, the distance between two consecutive pilots should be at most the number of OFDM symbols that corresponds to the coherence period of the channel, computed from the Doppler shift [34]. This constraint will make efficient the channel tracking over the time.

On the receiver side, knowing the transmitted pilots, we only can obtain the channel estimation (using LS or MMSE criterion) at those resources where the pilots were placed. Then, an interpolation process is needed in order to obtain the channel response at all time-frequency resources. Depending on the requirements of the link (performance or delay), the interpolation method could be done in one dimension (1D) (frequency domain) or two dimensions (2D) (time-frequency domain), based on different algorithms, such as: linear, quadratic, cubic, etc.

Finally, given the estimated CSI for all time-frequency resources, the received data are equalized by applying typically ZF or MMSE criterion.

## 3.2 MIMO and massive MIMO combined with OFDM

In a mobile communication scenario, typically the BS is equipped with an array of antennas and it is serving several single-antenna UEs. In the DL, the BS may transmit data using all the antennas in the same time-frequency resource; and in the UL, many UEs may also be scheduled to transmit their information in the same time-frequency resource in order to exploit the multiplexing gain. Under this situation, a new channel estimation procedure must be developed in order to successfully obtain all the CSI among all UEs and antennas of the BS. In order to provide a better understanding of the procedure, we use an example based on LTE [1] (see Fig. 3.1). Assuming a DL scenario where the BS is equipped with two antennas and there are two UEs, the procedure is the following:

- In the first training period, the antenna #1 transmits its pilot sequence, and the other antenna does not transmit. All UEs compute their CSI from antenna #1.
- In the second training period, the antenna #2 transmits its pilot sequence, and the other antenna does not transmit. All UEs compute their CSI from antenna #2.

The UL scenario is similar to the DL, where the roles of antennas and UEs are exchanged.

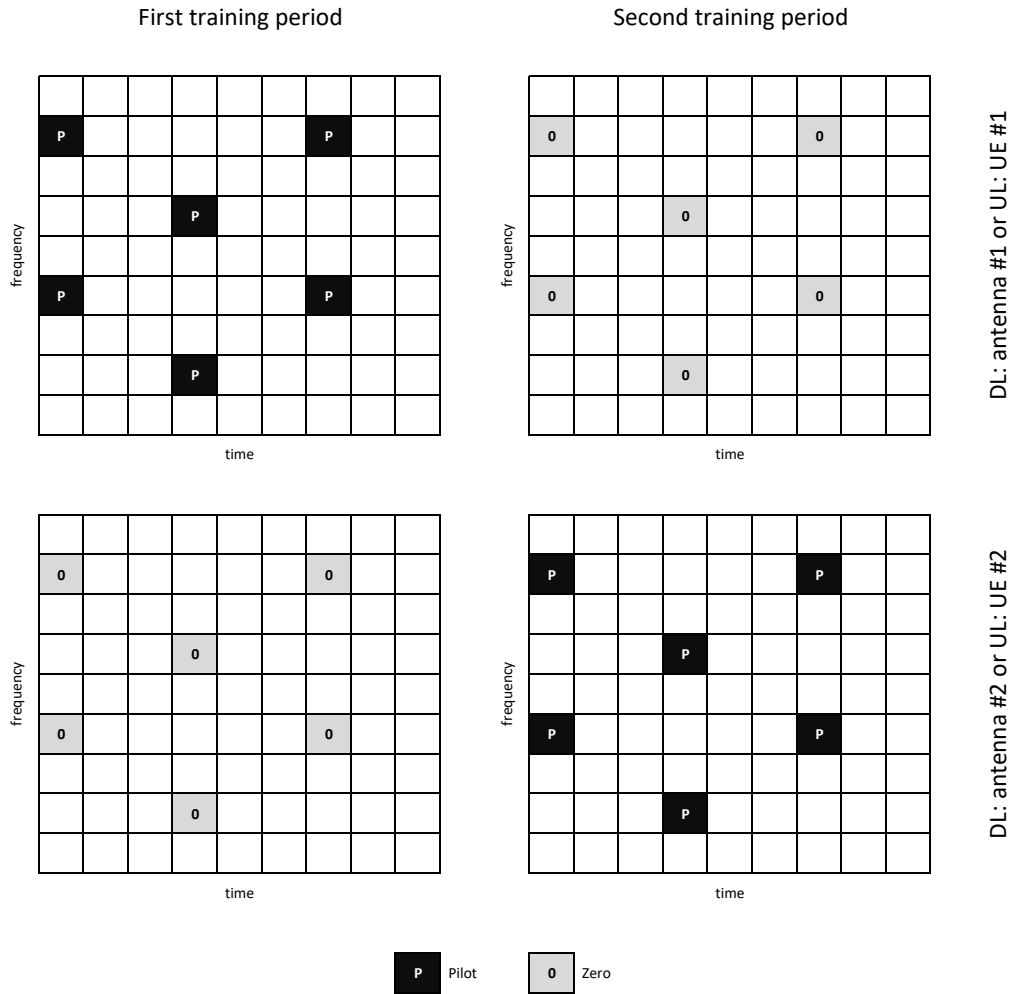


Figure 3.1: Example of pilot transmission in MIMO-OFDM for DL (two antennas at BS) or UL (two UEs).

When the number of antennas or UEs is large, the described procedure in Fig. 3.1 is not efficient, due to the high number of required training periods. Under this situation, it is proposed the use of orthogonal sequences, such as Zadoff–Chu [1]. However, the number of orthogonal sequences is limited for a given sequence length, and it is very important to use short sequences in order to also constrain the delay. Hence, a set of orthogonal sequences must be shared by all the antennas of the BS or UEs of the same cell, and assuming universal frequency reuse scenario adopted in 5G, it may cause the well-known pilot contamination issue [35]. An example of pilot contamination is illustrated in Fig. 3.2, where the UE #2 may receive the same orthogonal sequence from its BS and the BS of the adjacent cell; and the BS #1 may receive the same orthogonal sequence from its UE and another UE from the adjacent cell. In both situations, the undesirable interference source will affect in the performance of the computation of CSI due to

the fact that the frequency selective channel among all BSs and UEs are completely uncorrelated. There are many proposed schemes to solve this issue, however, we are not going to analyze them because it is out of the scope of this thesis.

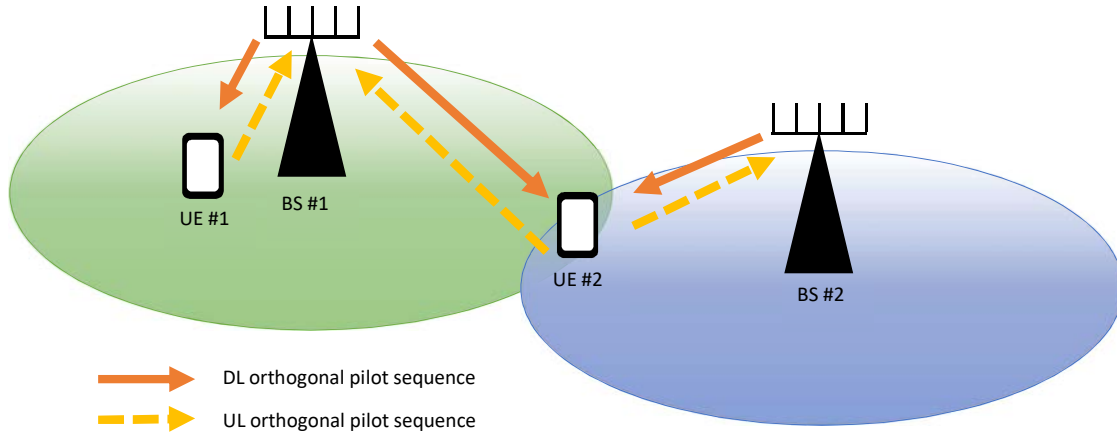


Figure 3.2: Example of pilot contamination.

After the reception of pilot sequences and the computation of CSI (assuming it is interference-free), the tasks of interpolation and computation of the precoding/postcoding matrices should be performed by the BS, due to the fact that UEs are low-cost devices which have not enough resources to operate with such demanding operations. In time division duplex (TDD) case [36], channel reciprocity is usually assumed, where the channel estimation is only performed in the UL and the computed CSI is also reused for the DL. However, in frequency division duplex (FDD) scenario [36], the CSI of DL and UL are completely different, and in the case of DL, all UEs must feed the estimated CSI back to the BS. Moreover, even assuming the BS has a high number of resources that allows a great computing capacity, when the number of antennas is moderately large, the delay caused by the computation of the precoding/postcoding matrices is very high. In TDD case, the BS must interpolate the CSI obtained in the UL for each antenna and each time-frequency resource, where a linear interpolation method is usually chosen in order to reduce the complexity. Then, for each time-frequency resource, the equalizer must be computed which involves a prohibitive matrix inversion if either ZF or MMSE criterion is chosen. Furthermore, in FDD scenario, the situation is even worse due to the fact that we must also compute the equalizers for the DL.

Thus, the implementation of massive MIMO is preferable in TDD rather than FDD [36], due to the channel reciprocity assumption. When the number of antennas is large, not only the great amount of CSI that should be fed-back to the BS is not affordable, but also the extra complexity in the interpolation and computation of equalization matrices will considerably increase the delay.

Unfortunately, nowadays, almost of all the bands dedicated for mobile communications are based on FDD, hence, an elegant solution for FDD must be found.

In the literature, there are two independent research lines in order to reduce the mentioned complexity of the computation of precoding/postcoding matrices. The first approach consists in interpolating the inverted channel matrix [37], where the matrix inversions are only performed at pilot subcarriers. In [37], a detailed analysis and numerical results of the complexity reduction is given. However, the performance degradation of its proposal is not shown in terms of either SINR or SER. The second one focuses on how to reduce the number of operations in the matrix inversion. To do that, there are two classes of methods: Neumann Series (NS) expansion [38] and numerical iterative schemes [39][40]. The former uses a low-complexity approximation of the inverse matrix, and the latter performs a successive interference cancellation (SIC), so it avoids the matrix inversion. According to [38], in order to reduce the complexity for massive MIMO-OFDM, it is preferable to reduce the number of iterations to one, so both NS and numerical iterative schemes present a similar performance in terms of complexity and SER.

### 3.3 FBMC

The main issue of FBMC-OQAM in order to obtain the CSI is related to the intrinsic self-interference caused by the surrounding symbols, due to the use of non-rectangular prototype filters, that must be taken into account before the equalization process. Two alternatives for placing the pilot information for channel estimation in FBMC-OQAM are proposed in the literature, namely preamble-based [41] and scattered pilot-based [42] [43], similar to OFDM.

Focusing on scattered pilot-based techniques, the two classical ones are auxiliary pilot (AP) [42] and pair of pilots (POP) [43]. AP consists in transmitting an additional auxiliary pilot along with the traditional one. By doing so, the received pilots become interference-free, and channel estimation can be performed in the same way as in OFDM systems. However, this technique has two main drawbacks, one of them is that the minimum required power of the auxiliary pilot is about 3.3dB higher than the power of data symbols, which means an additional waste of the valuable energy and increasing the PAPR; the second issue is the additional complexity added at the transmitter side which requires the computation of all the auxiliary pilots. POP transmits two precoded pilots which are capable of jointly compensating the self-interference. The receiver must perform a linear combination of the two received pilots in order to get the estimated channel. However, due to this combination, it may increase also the noise which compromises the global performance.

Lately, several modifications based on the combination of AP and POP are proposed in order

to solve the mentioned issues. Some of them are: precoded AP [44][45], composite pilot pair (CPP) [46], dual-dependant pilots (DDP) [47] and interference-dependant pair of pilots (IDPOP) [48]. Precoded AP solves the power overhead of AP by precoding totally or partially the neighboring data. Unfortunately, this method is computationally complex and it only can be used when the density of pilots is extremely low. The rest of proposals consist in jointly computing two or three pilots in order to try, as far as possible, to avoid the power overhead at the transmitter side. Additionally, at the receiver side, they take advantage of the artificially enhanced self-interference of the pilots (known as pseudo-pilots) in order to improve the MSE of the estimated channel. However, these improvements are made at the expense of increasing the complexity at both sides of the communication system. At the transmitter side, all the proposals are computing at least two pilots, instead of one as in AP. At the receiver side, CPP and IDPOP also require additional operations in order to get the channel estimation, similar to POP.

The complexity enhancement introduced by the mentioned techniques is not practical to be applied in some realistic communication systems. This is the case of MTC, where one of the constraints of UEs is to enlarge the battery cycle as long as possible. Hence, the needed computations in order to deal with the self-interference could drain the battery of the UEs and a new scheme should be deployed.

### 3.4 Millimeter wave

In mmWave bands, the propagation condition is not very stable due to the fact that there is a great path loss, and therefore, beam management process is a must in order to increase the quality of the link as far as possible, as we mentioned in the previous chapter. The channel estimation process is a very important task not only for performing the precoding/postcoding equalization, but also it improves the estimation of the location of UEs in order to obtain more accurate beams. Hence, the channel estimation procedure keeps being a challenging task due to the wide dynamic SNR ranges. Note that, even though the massive number of antennas at the BS will compensate the large and changing path loss, the channel must be estimated before this compensation is effective [49].

The channel model can be considered sparse in mmWave, where there are just a few paths thanks to the narrow beams produced by the high carrier frequency [50]. In the literature, there are several efficient channel estimation techniques for mm-Wave massive multiple antenna systems assuming the sparsity nature of the channel, such as compressive sensing [51] and subspace methods [52]. Compressive sensing based methods are more appealing due to the fact that they are low-complexity methods and they require a reduced number of training sequences, as compared to



other candidates. However, a common issue of all techniques consists in the bad adaptation to the different SNR conditions which is very common in mmWave radio links, as we mentioned before. Furthermore, these techniques have an important disadvantage, namely that they assume a parametric approach for the direction of arrival (DoA) of each tap of the frequency-selective channel. This fact implies the need of an antenna array calibration process [53] of the system in order to fully characterize any non-linear or unexpected effects in both array antenna and RF chains, caused by the manufacturing or installation issues.

One of the most appealing proposals given in [54] proposes a subspace method assuming that the spatial features are completely unknown, leading to non-parametric estimation in which antenna array calibration is no longer required. Furthermore, it exploits a low-rank (LR) algebraic structure of the channel by projecting the estimated channel on the spatial and temporal (ST) covariance matrices. When the SNR is not so high, the LR version of the estimated channel provides a better performance than the full-rank (FR) one in terms of bias-variance trade-off in the MSE. However, this method is not accurate enough due to the fact that they assumed that there is no correlation between spatial and temporal channel behavior. This assumption holds if and only if the receiving signal of all taps of the multi-path channel, with different time of arrival (ToA), have the same DoA at the BS, which is not true in realistic scenarios.

## 3.5 Other approaches

### 3.5.1 ST

Currently, PSAM is the most used technique in coherent detection. However, as we mentioned, PSAM reduces the efficiency of the link and some alternatives are proposed. ST is a semi-blind channel estimation technique, which achieves a better spectral efficiency. It consists in arithmetically superimposing a pilot over the data signal, allowing us to use all available resources to transmit information and, thus, enhance the bandwidth efficiency.

Firstly, OFDM combined with ST is proposed in [55]. Later, the combination of OFDM-OQAM and ST scheme has been addressed in [56], where a great improvement in the spectral efficiency is shown due to this combination. In this reference, the channel equalization is based on a correlated-based method in order to reduce the self-interference. However, it is difficult to evaluate the goodness of this proposal, since it does not show its effectiveness in terms of MSE of the channel estimation, or the SER of the entire system. Finally, we proposed the combination of FBMC-OQAM with ST in [16], where we can achieve even a better improvement in terms of spectral efficiency, compared to [55]. This extra improvement is due to the use of the well designed

prototype filter considered in FBMC-OQAM, that we mentioned before. Moreover, we proposed a novel channel estimation technique with self-interference cancellation. The performance of the system is evaluated through the MSE of channel estimation and SER, where it outperforms AP method [42]. Moreover, in [17], we analytically verified the superiority of FMBC-OQAM combined with ST through detailed capacity comparison between OFDM and FBMC-OQAM, where both are using either PSAM or ST.

### 3.5.2 Non-coherent demodulation scheme

Previously, we have seen that when a coherent demodulation scheme is adopted for MIMO-OFDM systems, it not only requires a significant amount of orthogonal pilot sequences to obtain the estimation of the channel between each UE and each antenna of the BS, but also the high number of operations in order to compute the precoding/postcoding matrices in every time-frequency resource. All these procedures are reducing the overall capacity and increasing the complexity of the system.

Given the mentioned issues, an alternative way is the use of non-coherent schemes. [57] has proposed this idea with the use of amplitude shift keying (ASK). However, the number of required antennas is excessively large for a reasonable performance. Later, [58] proposed the use of differential phase shift keying (DPSK), where two received contiguous symbols are properly combined in order to produce a joint-symbol. The final decision is done on this joint-symbol, which is a superposition of the transmitted symbol of each UE. This proposal significantly outperforms [57], showing that it does not require a huge number of antennas in order to achieve an acceptable performance. Later, assuming more realistic cases where the propagation channel is doubly dispersive, we proposed the extension of the scheme [58] to the use of OFDM in [18]. Additionally, due to the fact that OFDM implements a two dimensional resource grid, the differential encoding can be performed in either time or frequency domain, where we define them as time domain scheme (TDS) and frequency domain scheme (FDS), respectively. Comparing both schemes, TDS requires two OFDM symbols in order to perform the differential decoding, increasing the memory consumption and latency of the system. Hence, TDS has some shortcomings for either mMTC or URLLC. In FDS, the differential encoding can be performed for each pair of contiguous subcarriers, overcoming the mentioned disadvantages of TDS. However, the difference of the phase between the two contiguous subcarriers is not averaged out by the large number of antennas at the BS, causing an additional rotation in the received joint-symbol. Therefore, FDS needs a phase estimation method to compensate it. We develop such a scheme and we provide the expression of the SINR for both cases.

### 3.6 System model

In this section, we provide a generic system model which is valid for all the following chapters. Later, in each chapter, we will provide more specific details according to its particular scenario.

We consider a multi-user MIMO system, which is made up by one BS equipped with an array of  $N_v$  antennas and  $N_u$  UEs, where each of them is equipped with one single-antenna (see Fig. 3.3). In the DL scenario, the received signal at the single antenna of  $u$ -th UE can be obtained as

$$y_u[n] = \sum_{v=1}^{N_v} h_{uv}[n, \tau] * x_v[n] + w_u[n], \quad 1 \leq u \leq N_u, \quad (3.1)$$

where  $n$  denotes the time instants,  $x_v[n]$  represents the transmitted data stream by the  $v$ -th antenna of the BS, with unit average power  $\mathbb{E}\{x_v[n]\} = 1$ ;  $w_u[n]$  is the additive white Gaussian noise (AWGN) at the input of the single antenna of the  $u$ -th UE, where we assume that the noise is temporally and spatially uncorrelated and it is distributed according to  $w_u[n] \sim \mathcal{CN}(0, \sigma_{w_u}^2)$ ; and  $h_{uv}[n, \tau]$  denotes the channel impulse response of the multi-path channel with  $N_p$  coefficients from the  $v$ -th transmitter antenna of the BS to the single antenna of the  $u$ -th UE defined as

$$h_{uv}[n, \tau] = \sum_{p=1}^{N_p} d_p^{uv}[n] \delta[\tau - \tau_p], \quad 1 \leq u \leq N_u, 1 \leq v \leq N_v, \quad (3.2)$$

and assuming that the power delay profile (PDP) of all links among all UEs and all antennas of the BS are the same, hence, it satisfies that

$$d_p^{uv}[n] \sim \mathcal{CN}(0, \sigma_{d_p}^2), \quad \sum_{p=1}^{N_p} \sigma_{d_p}^2 = 1, \quad (3.3)$$

where  $\sigma_{d_p}^2$  denotes the power of the  $p$ -th tap.

Analogously, in the UL scenario, the received signal at the  $v$ -th antenna of the BS can be obtained as

$$y_v[n] = \sum_{u=1}^{N_u} h_{vu}[n, \tau] * x_u[n] + w_v[n], \quad (3.4)$$

where  $x_u[n]$  represents the transmitted data stream by the single-antenna of the  $u$ -th UE, with unit average power  $\mathbb{E}\{x_u[n]\} = 1$ ;  $w_v[n]$  is the AWGN at the input of  $v$ -th antenna of the BS and it is distributed according to  $w_v[n] \sim \mathcal{CN}(0, \sigma_{w_v}^2)$ .

The channel frequency response at  $n$ -th instant for the case of DL (or UL) can be defined as

$$\tilde{\mathbf{h}}_{uv,n}(K \times 1) = \mathbf{F}_K \mathbf{h}_{uv,n} \sim \mathcal{CN}(\mathbf{0}_{K \times 1}, \mathbf{I}_K), \quad (3.5)$$

where  $\mathbf{h}_n(N_p \times 1)$  is the vector representation of  $h_{v,u}[n, \tau]$  and  $\mathbf{F}_K$  is the  $K$ -point normalized FFT matrix with entries

$$[\mathbf{F}_K]_{a,b} = \frac{1}{\sqrt{K}} e^{-j \frac{2\pi}{K} (a-1)(b-1)}, \quad 1 \leq a, b \leq K. \quad (3.6)$$

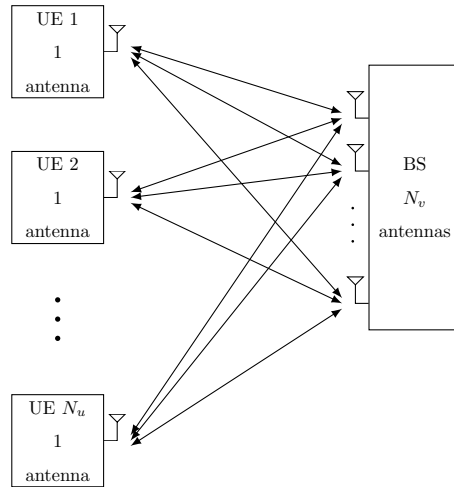


Figure 3.3: MU-MIMO scenario.

### 3.7 Channel model

The wireless channel is typically represented by a linear filter [34], where it is characterized by its impulse response, as we described in (3.2). This kind of channel description is known as tapped delay line (TDL) modeling, where the receiver (see Fig. 3.4) received different echoes produced by the existence of several obstacles between the transmitter and receiver. Furthermore, each tap is modeled according to a known distribution, typically Rayleigh for non-line of sight propagation scenarios or Rice for line of sight scenarios. Furthermore, if there is mobility, Doppler shift is also considered.

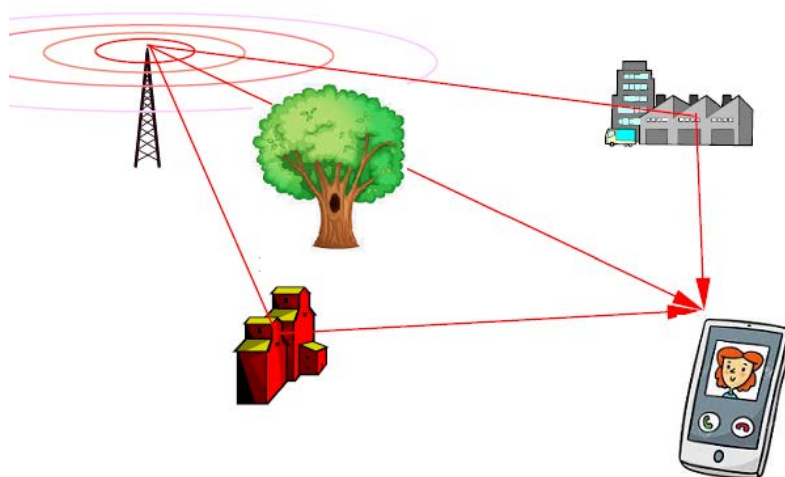


Figure 3.4: Example of wireless propagation environment

TDL modeling is very useful for lower frequency bands. However, when a high carrier frequency

is used, such as mmWave, the effect of clustering appears in the propagation, as illustrated in Fig. 3.5 [59]. The receiver will receive many echoes from some particular clusters, where each cluster has different rays with the same power due to the presence of several scatters in one cluster. This model is known as clustered delay line (CDL) modeling [60].

When MIMO is adopted, some correlation matrices are provided for lower frequency bands, where the correlation coefficients point out how correlated are the channel of one antenna to the others. For the case of mmWave, the correlation of antennas is additionally modeled by the diagram pattern of the antenna array, which imposes a spatial selectivity. Thus, it is important to provide the direction of departure (DoD) of the transmitted signal and the direction of arrival (DoA) to the receiver, in order to characterize the array response at those angles. More details are given in Chapter 6.

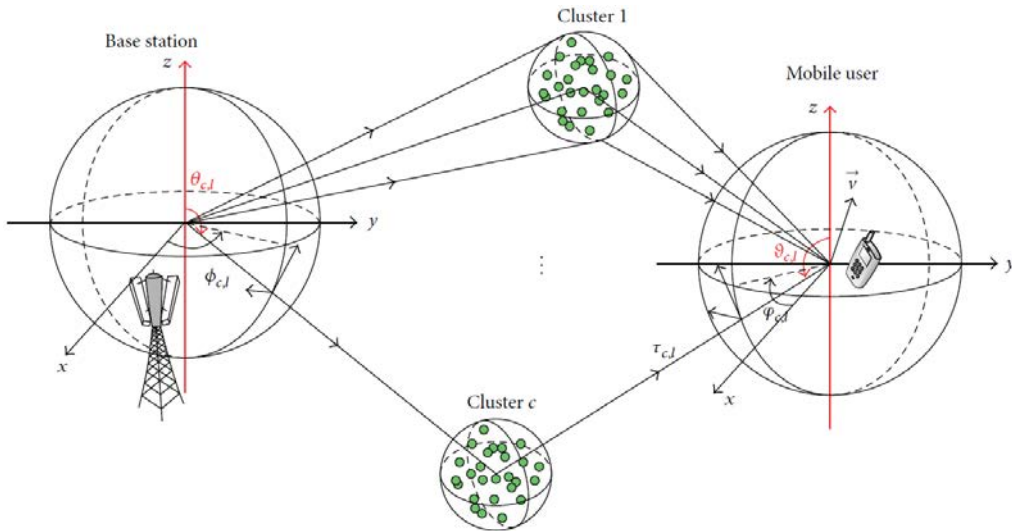


Figure 3.5: Example of wireless propagation environment

In LTE [23], three PDPs based on TDL modeling are proposed: Extended Pedestrian A (EPA), Extended Vehicular A (EVA) and Extended Typical Urban (ETU), with different values of Doppler frequency. They provide a good characterization of different propagation scenarios and they are widely used by the research community and the industry. Recently, 5G [7] proposed both TDL and CDL channel propagation models. Due to the fact that 5G is going to be used in different propagation environments, from indoor office to macro cell scenarios, the delay spread of these PDP can be adapted. Besides, in the case of CDL, it also provides different angle values of DoD and DoA for both azimuth and elevation.



## Chapter 4

# New pilot schemes for channel estimation in FBMC-OQAM

In the present chapter we propose two new pilot sequences which are capable of taking advantage of the self-interference produced by the well-localized prototype filter in FBMC-OQAM, and a novel channel estimation technique with an affordable complexity suitable for either devices powered by battery or URLLC communications.

Continuous pilot sequences (CPS) are widely used in many OFDM-based communication systems, such as DVB-T [20], or WiMax [21], among others. The main reason of using CPS is precisely when the channel is fast varying, because they provide a continuous tracking in order to improve the performance of the entire system. Additionally, besides the channel effects, there are other issues that should be taken into account as well, such as propagation attenuation, shadowing, antenna pattern, etc. CPS can be applied in the case of the recently proposed mmWave [9] and in vehicular communications [61].

To the best of our knowledge, CPS has not been proposed before for FBMC-OQAM. Hence, we propose an efficient combination of these two elements, which is not straightforward due to the presence of the self-interference in FBMC-OQAM, unlike in OFDM systems. At the transmitter side, the CPS must be specifically designed to work under this self-interference and avoid either any precoding procedures or enhancing the power overhead, that is present in the existing techniques. At the receiver side, due to the adequate-design of CPS, a low-complexity averaging process is only required in order to reduce the noise and data interference, combined with the advantage of using pseudo-pilots in order to achieve a better channel estimation in terms of MSE. Hence, the low-complexity of CPS fits well with MTC, not only due to energy concerns, but also it makes

low-cost devices even competitive in terms of price.

However, CPS is only advisable when the channel is quite unstable in order to provide a good tracking of it. On the contrary, when the variability of the channel is lower, CPS could be inefficient due to the considerable amount of allocated pilots in the system. Therefore, in order to face this inefficiency, we propose a variant of CPS denoted as burst pilot sequences (BPS). This scheme not only has the same benefits of CPS, but it also provides the flexibility to select the length of the pilot sequence depending on the variability of the channel in each moment, not only keeping the quality of the estimated channel, but also improving the number of available resources for data transmission. Moreover, we provide an analytical model to characterize the MSE of our proposed schemes that perfectly matches the simulation results. Finally, we compare our proposals to different schemes, available in the literature, in terms of computational complexity and SER.

The remainder of the chapter is organized as follows. Section 4.1 provides the system model of FBMC-OQAM. Sections 4.2 and 4.3 proposes the novel CPS and BPS, respectively, specifically designed for FBMC-OQAM. Section 4.4 describes the new channel estimation method. Section 4.5 provides the analytical expression of the MSE. Section 4.6 shows the comparison of different schemes in terms of complexity. Section 4.7 presents some numerical results to provide a better understanding of the performance of the entire system. Finally, in section 4.8 some conclusions are pointed out for this chapter.

## 4.1 System model

The system model of this chapter is focused on a single-user single-input single-output (SISO) link (point-to-point), where a FBMC-OQAM waveform is transmitted. Hence,  $N_v = N_u = 1$  and we omit the sub-indexes  $u$  and  $v$  for ease of the comprehension of the system model.

### 4.1.1 FBMC-OQAM

Let  $\mathbf{S}$  denote a matrix containing the set of  $K \times M/2$  complex data symbols to be transmitted, where  $K$  represents the number of parallel subcarriers and  $M$  is the number of time instants. The complex symbols belong to a QAM constellation with unit average power denoted as  $\sigma_s^2 = 1$ . Given  $\mathbf{S}$ , it is transformed into OQAM real symbols, where the real and imaginary parts of  $\mathbf{S}$  are separated to build  $\mathbf{S}_o$

$$\begin{aligned} [\mathbf{S}_o]_{k,m=2m'} &= \text{Re} \left\{ [\mathbf{S}]_{k,m'} \right\}, & [\mathbf{S}_o]_{k,m=2m'+1} &= \text{Im} \left\{ [\mathbf{S}]_{k,m'} \right\}, \\ k &= 0 \cdots K-1, & m' &= 0 \cdots \frac{M}{2} - 1, & m &= 0 \cdots M-1 \end{aligned} \quad (4.1)$$

Note that the size of  $\mathbf{S}_o$  is  $K \times M$ . Additionally, the average power of  $\mathbf{S}_o$  is  $\sigma_{s_o}^2 = 0.5$ .



The baseband model of the FBMC-OQAM transmitted signal is given by

$$x[n] = \sum_{k=0}^{K-1} \sum_{m=0}^{M-1} [\mathbf{S}_o]_{k,m} e^{j\phi_{k,m}} g \left[ n - m \frac{K}{2} \right] e^{j \frac{2\pi}{K} km \Delta f}, \quad (4.2)$$

where  $\Delta f = 1/T$  is the subcarrier spacing,  $T$  is the duration of the transmission of  $M$  samples,  $g[n]$  is the normalized real symmetric prototype filter impulse response and the phase  $\phi_{k,m}$  is given by

$$\phi_{k,m} = \begin{cases} 0, & k+m \text{ even} \\ \frac{\pi}{2}, & k+m \text{ odd} \end{cases}. \quad (4.3)$$

We define  $g_{k,m}[n]$  as a time-frequency shifted version of  $g[n]$ , which can be expressed by

$$g_{k,m}[n] = g \left[ n - m \frac{K}{2} \right] e^{j\phi_{k,m}} e^{j \frac{2\pi}{K} km \Delta f} = g_m[n] e^{j\phi_{k,m}} e^{j \frac{2\pi}{K} km \Delta f}. \quad (4.4)$$

Therefore, we can rewrite (4.2) as

$$x[n] = \sum_{k=0}^{K-1} \sum_{m=0}^{M-1} [\mathbf{S}_o]_{k,m} g_{k,m}[n]. \quad (4.5)$$

This operation is also known as the synthesis filter-bank (SFB) (see Fig. 4.1). Note that  $g[n]$  and  $\phi_{k,m}$  are designed so that  $g_{k,m}[n]$  is orthogonal in the real field satisfying

$$\text{Re} \{ \langle g_{k,m}[n], g_{k',m'}[n] \rangle \} = \begin{cases} 1, & k=k' \text{ and } m=m' \\ 0 & \text{otherwise} \end{cases}. \quad (4.6)$$

In the absence of channel effects (distortion-free and noiseless) and assuming that we are sampling at the optimal point, the demodulated signal at subcarrier  $k_0$  and symbol  $m_0$  can be expressed by

$$[\mathbf{R}_o]_{k_0,m_0} = \langle x[n], g_{k_0,m_0}[n] \rangle = \sum_{k=0}^{K-1} \sum_{m=0}^{M-1} [\mathbf{S}_o]_{k,m} \sum_n g_{k,m}[n] g_{k_0,m_0}^*[n]. \quad (4.7)$$

Applying (4.6), it is straightforward to show that the desired signal is always orthogonal to the self-interference, simplifying (4.7) in

$$[\mathbf{R}_o]_{k_0,m_0} = \underbrace{[\mathbf{S}_o]_{k_0,m_0}}_{\text{desired signal}} + \underbrace{\sum_{(k,m) \neq (k_0,m_0)} [\mathbf{S}_o]_{k,m} [\mathbf{\Gamma}_{k_0,m_0}]_{k,m}}_{\text{self-interference}} = [\mathbf{S}_o]_{k_0,m_0} + j [\mathbf{B}]_{k_0,m_0}, \quad (4.8)$$

where  $[\mathbf{\Gamma}_{k_0,m_0}]_{k,m} = \langle g_{k,m}[n], g_{k_0,m_0}[n] \rangle$  is the coefficient which represents the interference caused in  $[k_0, m_0]$  by each of the surrounding symbols placed at  $[k, m]$ , due to the joint effect of the residual components of the prototype filter  $g[n]$  and additional phase rotation  $\phi_{k,m}$ , and  $\mathbf{B}$  denotes the whole self-interference amplitude at  $[k_0, m_0]$ . The operation in (4.7) is also known as the analysis filter-bank (AFB) (see Fig. 4.2).

Finally, all the original symbols  $\mathbf{S}$  are recovered by

$$[\mathbf{S}]_{k_0,m'_0} = \text{Re} \{ [\mathbf{R}_o]_{k_0,m_0=2m'_0} \} + j \text{Im} \{ [\mathbf{R}_o]_{k_0,m_0=2m'_0+1} \}. \quad (4.9)$$

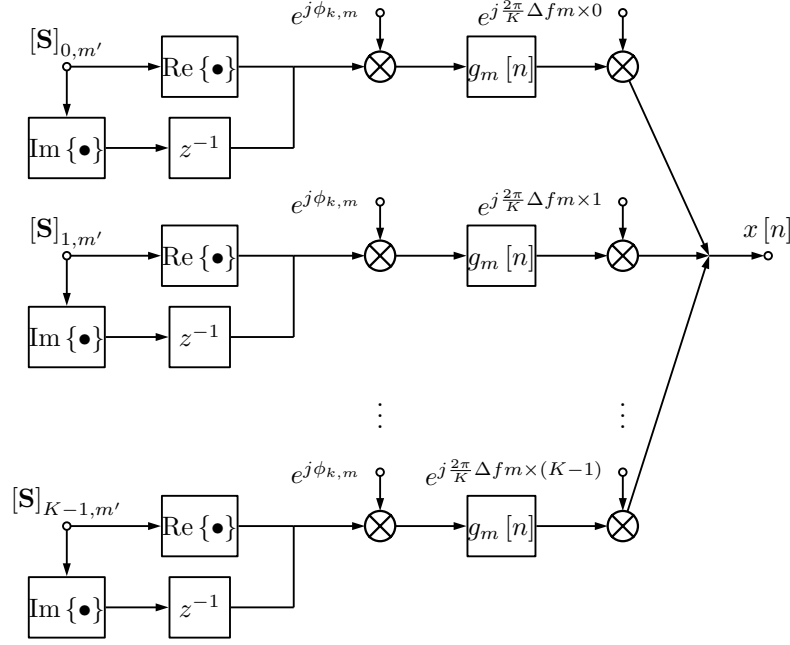


Figure 4.1: Transmitter baseband model of FBMC-OQAM.

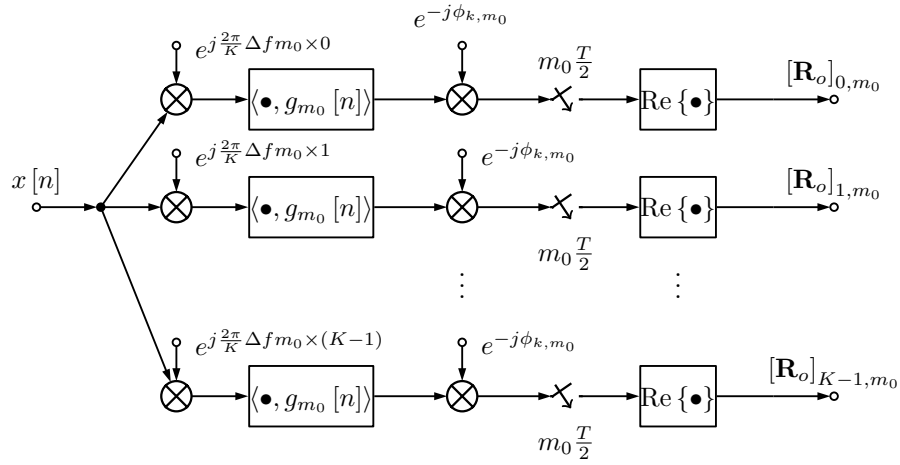


Figure 4.2: Receiver baseband model of FBMC-OQAM.

### 4.1.2 Effects of the channel in FBMC-OQAM

In the previous subsection, we have shown the analytical model for FBMC-OQAM under a scenario of absence of channel effects. However, in a realistic environment, the signal  $x[n]$  goes through a frequency-selective fading channel. According to (3.1) and (3.4), the received signal can be expressed as

$$y[n] = h[n, \tau] * x[n] + w[n]. \quad (4.10)$$

Therefore, (4.10), (4.8) will be also modified by the channel effects, where regarding [42] and other references, the received signal can be approximated by

$$\mathbf{R}_o \simeq \mathbf{H} \circ (\mathbf{S}_o + j\mathbf{B}) + \mathbf{W}, \quad (4.11)$$

where  $\mathbf{H} (K \times M)$  and  $\mathbf{W} (K \times M)$  are the frequency response of the channel and noise respectively. According to [62], each element of  $\mathbf{H}$  is defined by

$$[\mathbf{H}]_{k,m} = \left[ \tilde{\mathbf{h}}_m \right]_k, \quad (4.12)$$

and  $\mathbf{W}$  is the filtered noise, which is also a random variable with distribution  $[\mathbf{W}]_{k,m} \sim \mathcal{CN}(0, \sigma_w^2)$  defined in [28].

Finally, note that the error in the approximation taken in (4.11) is negligible when it satisfies  $K \gg \tau_{N_p}$  which always holds in multi-carrier systems.

## 4.2 Continuous pilot sequence (CPS)

Inspecting (4.11), we can see that FBMC-OQAM is using only half of the total amount of received power for transmitting data, since the other half is wasted by the self-interference term. In the particular case of channel estimation, the interference part must be taken into account in some way in order to get an accurate estimation, otherwise the performance of the entire system would be compromised.

We start analyzing how the interference is caused by the choice of the prototype filter in order to get some understanding of how to improve the channel estimation. To facilitate the analysis, we will use the PHYDYAS prototype filter [63], widely employed in the literature, as a particular case. In Table 4.1, we can see the  $\mathbf{\Gamma}_{k_0, m_0} (3 \times 7)$  coefficients when PHYDYAS prototype filter is used. We can clearly see that it is only well-localized in frequency since it only interferes two adjacent subcarriers. However, it is not localized in time, spreading the interference up to six contiguous symbols.

Let us define the vector  $\gamma_m$  of size  $(6 \times 1)$ , which represents the 6 black colored interference values of Table 4.1, and vectors  $\gamma_u$  and  $\gamma_l$  of size  $(N_\gamma \times 1)$ , which represent the  $N_\gamma = 7$  upper and lower gray colored interference values of Table 4.1 respectively. Note that the highest self-interference is caused by the symbol placed at  $(k_0, m_0 - 1)$  and  $(k_0, m_0 + 1)$ . Additionally, their coefficients satisfy the following condition

$$\text{tr}(\text{diag}(\gamma_m)) \simeq 1. \quad (4.13)$$

Keeping these properties in mind, we can design continuous pilot sequences placed at every time instant, also known as pilot tones, which are capable of taking advantage of the self-interference

Table 4.1: Intrinsic interference caused to data placed at  $[\mathbf{\Gamma}]_{k_0, m_0}$  using the PHYDYAS prototype filter.

	$n_0 - 3$	$n_0 - 2$	$n_0 - 1$	$n_0$	$n_0 + 1$	$n_0 + 2$	$n_0 + 3$
$m_0 - 1$	$-j0.0429$	0.125	$j0.2058$	0.2393	$-j0.2058$	$-0.125$	$j0.0429$
$m_0$	<b><math>-0.0668</math></b>	<b>0</b>	<b><math>0.5644</math></b>	<b>1</b>	<b><math>0.5644</math></b>	<b>0</b>	<b><math>-0.0668</math></b>
$m_0 + 1$	$j0.0429$	$-0.125$	$-j0.2058$	0.2393	$j0.2058$	0.125	$-j0.0429$

over the time domain in order to enhance the power of the received pilot sequences (pseudo-pilots) and, hence, to improve the channel estimation. The idea of using pseudo-pilots is already considered by preamble-based techniques and IDPOP. By allowing the simultaneous transmission of pseudo-pilots with data symbols and through an adequate design of the pilot sequences, our proposal reduces the computational complexity at the receiver side, compared to IDPOP technique, while maintaining a good error performance as we will show.

According to (4.13), let us define a known pilot sequence row vector  $\mathbf{p}$ , given by

$$\mathbf{p} = (p_s + jp_s) \mathbf{1}_{1, M/2}, \quad (4.14)$$

where  $p_s = 1/\sqrt{2}$ . Note that the proposed sequence has the same power as the data symbols, getting rid of the power overhead, unlike AP, and without any additional computation, unlike DDP. Applying (4.1) to (4.14), we obtain  $\mathbf{p}_o$  which is defined by

$$\mathbf{p}_o = p_s \mathbf{1}_{1, M}. \quad (4.15)$$

To better analyze this problem, let us assume that we are sending a pilot sequence in any subcarrier  $k_0$  (see Fig. 4.3a). Then in the absence of the channel effects, the received pseudo-pilot sequence  $\mathbf{q}_o$  can be computed using (4.7) and (4.13), which is given by

$$\mathbf{q}_o = \mathbf{p}_o + j\mathbf{p}_o. \quad (4.16)$$

Observing (4.16), we can clearly see that the received pseudo-pilot not only has twice the power of the transmitted one (4.15) due to the self-interference, but also this interference term is a known value due to the property described in (4.13) combined with the well-designed pilot sequence (4.15). Additionally, note that  $q_o[k_0, m]$  has the same value for any value of  $m$ , which facilitates the averaging process at the receiver side.

At the transmitter side, the  $K$  available subcarriers of  $\mathbf{S}_o$  are split into two groups: one for data  $\mathbf{S}_{o,d}$  of size  $(K_d \times M)$  and another one for pilots  $\mathbf{S}_{o,p}$  of size  $(K_p \times M)$ , where  $K = K_d + K_p$ . Although it may seem that CPS increments the pilot density, this is not so in the overall system. For the same pilot density in CPS as previous scattered pilot-based methods, CPS still outperforms those previous methods as we will show.

### 4.3 Burst pilot sequence (BPS)

When the channel is not highly time-varying, the length of the pilot sequence (4.15) can be reduced in order to make a more efficient design, with the proposal of BPS (see Fig. 4.3b). The new pilot sequence  $\mathbf{p}_o$  is defined by

$$\mathbf{p}_o = \begin{bmatrix} 0 & p_s \mathbf{1}_{1, N_b} & 0 \end{bmatrix}. \quad (4.17)$$

where  $N_b + 2$  is the length of the burst sequence, and the two zeros at the beginning and at the end of the sequence are added in order to avoid the interference caused by the left and right data symbols that have the highest interference.

Given (4.17), it is obvious to see that the main advantage of BPS consists in that  $N_b$  can be designed according to the variability of the channel, so incrementing the data rate when the channel conditions allow it. The value of  $N_b$  can be characterized by the density of the sequence ( $\nu$ ), which is defined as

$$\nu = \frac{N_b + 2}{N_c} \leq 1, \quad (4.18)$$

where  $N_c$  is the total number of contiguous symbols in the time domain that will use the estimated channel obtained by the  $N_b + 2$  pilots, where  $N_c$  includes the  $N_b + 2$  pilots. Note that, the equality of (4.18) holds for CPS.

Additionally,  $N_c$  should satisfy that

$$N_c \leq \frac{T_c}{T/2}, \quad (4.19)$$

where  $T_c$  is the channel coherence time [34]. Otherwise, the performance of BPS is compromised.

	m=1	m=2	m=3	m=4	m=5	m=6	m=7	m=8	m=9	m=10	m=11	m=12	m=13	m=14
k=1														
k=2														
k=3	p	p	p	p	p	p	p	p	p	p	p	p	p	p
k=4														
k=5														
k=6														
k=7	p	p	p	p	p	p	p	p	p	p	p	p	p	p
k=8														
k=9														
k=10														
k=11	p	p	p	p	p	p	p	p	p	p	p	p	p	p
k=12														
k=13														
k=14														
k=15	p	p	p	p	p	p	p	p	p	p	p	p	p	p
k=16														
k=17														

(a) CPS in FBMC-OQAM.

	m=1	m=2	m=3	m=4	m=5	m=6	m=7	m=8	m=9	m=10	m=11	m=12	m=13	m=14
k=1														
k=2														
k=3	0	p	p	p	p	p	0							
k=4														
k=5														
k=6														
k=7								0	p	p	p	p	p	0
k=8														
k=9														
k=10														
k=11	0	p	p	p	p	p	0							
k=12														
k=13														
k=14														
k=15								0	p	p	p	p	p	0
k=16														
k=17														

(b) BPS in FBMC-OQAM for  $\nu = 0.5$ .

Figure 4.3: Layout of the pilot symbols in the time-frequency grid.

## 4.4 Channel equalization for CPS and BPS

Given the system model detailed in the previous section, the received signal  $\mathbf{R}_o$  can also be split into  $\mathbf{R}_{o,d}$  and  $\mathbf{R}_{o,p}$  which correspond to the received data and pilot sequences respectively. In general, any element of  $\mathbf{R}_o$  can be expressed by (4.11). However, in the case of a received pilot sequence  $\mathbf{R}_{o,p}$  can be decomposed by

$$\mathbf{R}_{o,p} (K_p \times M) \simeq \mathbf{H} \circ ((\mathbf{q}_o \otimes \mathbf{1}_{K_p \times 1}) + j\mathbf{C}) + \mathbf{W}, \quad (4.20)$$

where  $\mathbf{C}$  is given by

$$j[\mathbf{C}]_{k_0, m_0} = \sum_{m=m_0-3}^{m_0+3} \sum_{\substack{k=k_0-1 \\ k \neq k_0}}^{k_0+1} [\mathbf{S}_o]_{k,m} [\mathbf{\Gamma}_{k_0, m_0}]_{k,m}, \quad (4.21)$$

which is the interference caused by data symbols only placed at subcarriers  $k_0 - 1$  and  $k_0 + 1$  (see Table 4.1). Comparing (4.8) and (4.21), it is obvious that  $\sigma_C^2 < \sigma_B^2$ , where  $\sigma_C^2$  and  $\sigma_B^2$  correspond

to the average power of  $\mathbf{C}$  and  $\mathbf{B}$  respectively, because the six interference terms from subcarrier  $k_0$  are not included in the sum.

In order to estimate the channel,  $\mathbf{R}_{o,p}$  is averaged over the variable  $m$ , as follows

$$\mathbb{E}_{N_g} \{\mathbf{R}_{o,p}\} = \mathbb{E}_{N_g} \{\mathbf{H} \circ ((\mathbf{q}_o \otimes \mathbf{1}_{K_p \times 1}) + j\mathbf{C})\} + \mathbb{E}_{N_g} \{\mathbf{W}\}, \quad (4.22)$$

where  $N_g$  is the number of averaged symbols. In the case of BPS, considering  $N_g \leq N_b$ ,  $N_g = N_b$  is a preferred choice, because a higher value of  $N_g$  corresponds to a lower interference due to the averaging process.

Without loss of generality, we focus in any  $N_g$  consecutive symbols out of  $M$ , ( $m = m_0 \cdots m_0 + N_g - 1$ ). Assuming that the channel frequency response is quasi-stationary in  $N_g$  symbols and the pseudo-pilot sequence for the  $k$ -th subcarrier always contains the same value at every time instant, the expression (4.22) can be simplified as

$$\mathbb{E}_{N_g} \{\mathbf{R}_{o,p}\} = \tilde{\mathbf{h}}_p \circ ((p_s + jp_s) \otimes \mathbf{1}_{K_p \times 1}) + \tilde{\mathbf{h}}_p \circ \underbrace{j\mathbb{E}_{N_g} \{\mathbf{C}\}}_{C_{N_g}} + \underbrace{j\mathbb{E}_{N_g} \{\mathbf{W}\}}_{W_{N_g}}, \quad (4.23)$$

Given the expression in (4.23), we can apply a LS technique [64] in order to estimate the channel using the pseudo-pilot  $p_s + jp_s$ , which is given by

$$\hat{\mathbf{h}}_p = (\mathbb{E}_{N_g} \{\mathbf{R}_{o,p}\}) (p_s + jp_s)^{-1}. \quad (4.24)$$

Once we have the estimated channel  $\hat{\mathbf{h}}_p$  for the pilot positions, we have to interpolate to obtain the values for the data indexes, according to

$$\hat{\mathbf{h}}_i (K_d \times 1) = \mathbf{\Omega} (K_d \times K_p) \hat{\mathbf{h}}_p (K_p \times 1), \quad (4.25)$$

where  $\mathbf{\Omega}$  is the matrix of interpolation coefficients.

Finally, in order to obtain the equalized symbols with a ZF technique, we just need to apply the following expression

$$\left[ \hat{\mathbf{S}}_{o,d} \right]_{k,m} = \left( \left[ \hat{\mathbf{h}}_i \right]_k \right)^{-1} [\mathbf{R}_{o,d}]_{k,m}, \quad 1 \leq m \leq M, \quad 1 \leq k \leq K. \quad (4.26)$$

## 4.5 Analysis the of estimation error

The estimated channel differs from the original one due to not only the noise, but also the self-interference. Let us define the matrix  $\hat{\mathbf{H}}_p$  which contains  $K_p$  rows and,  $\lceil M/N_g \rceil$  columns for CPS and  $\lceil \nu M / (N_b + 2) \rceil$  for BPS when considering  $N_g = N_b$ ; and  $\mathbf{H}_p$  corresponds to the actual channel coefficients of the same size. Therefore, the MSE can be defined and simplified by

$$MSE = \mathbb{E} \left\{ \left| \hat{\mathbf{H}}_p - \mathbf{H}_p \right|^2 \right\} = \sigma_H^2 \mathbb{E} \left\{ |C_{N_g}|^2 \right\} + \mathbb{E} \left\{ |W_{N_g}|^2 \right\}, \quad (4.27)$$

where we have used the fact that  $|p_s + jp_s|^2 = 1$  and  $\mathbb{E}\{|\mathbf{H}_p|^2\} = \sigma_H^2$ . Using some Normal distribution properties [65], the probability density function (PDF) of  $W_{N_g}$  is given by

$$W_{N_g} \sim \mathcal{CN}\left(0, \frac{\sigma_w^2}{N_g}\right). \quad (4.28)$$

In order to characterize the term  $C_{N_g}$ , we will reformulate the total self-interference term. Let us compute the self-interference  $\mathbf{c}_\phi$  at the  $m$ -th subcarrier for any  $N_g$  consecutive instants ( $m = m_0 \cdots m_0 + N_g - 1$ ) as

$$\mathbf{c}_\phi(N_g \times 1) = \mathbf{\Gamma}_e(N_g \times 2N_T) \mathbf{s}_\phi(2N_T \times 1) = \begin{bmatrix} \mathbf{\Gamma}_u(N_g \times N_T) & \mathbf{\Gamma}_l(N_g \times N_T) \end{bmatrix} \mathbf{s}_\phi, \quad (4.29)$$

where  $N_T = N_\gamma + N_g - 1$ ,

$$\mathbf{c}_\phi = \begin{bmatrix} [\mathbf{C}_\phi]_{k,m_0} \\ [\mathbf{C}_\phi]_{k,m_0+1} \\ \vdots \\ [\mathbf{C}_\phi]_{k,m_0+N_g-1} \end{bmatrix}, \quad [\mathbf{C}_\phi]_{k,m} = [\mathbf{C}]_{k,m} e^{j\phi_{k,m}}, \quad (4.30)$$

$$\mathbf{s}_\phi = \begin{bmatrix} [\mathbf{S}_\phi]_{k-1,m_0-3} \\ \vdots \\ [\mathbf{S}_\phi]_{k-1,m_0+N_T-4} \\ [\mathbf{S}_\phi]_{k+1,m_0-3} \\ \vdots \\ [\mathbf{S}_\phi]_{k+1,m_0+N_T-4} \end{bmatrix}, \quad [\mathbf{S}_\phi]_{k,m} = [\mathbf{S}_o]_{k,m} e^{j\phi_{k,m}}, \quad (4.31)$$

$$\mathbf{\Gamma}_l = \begin{bmatrix} [\gamma_l]_1 & \cdots & [\gamma_l]_{N_\gamma} & 0 & \cdots & 0 \\ 0 & [\gamma_l]_1 & \cdots & [\gamma_l]_{N_\gamma} & \cdots & 0 \\ \vdots & \ddots & \ddots & \ddots & \ddots & \vdots \\ 0 & \cdots & 0 & [\gamma_l]_1 & \cdots & [\gamma_l]_{N_\gamma} \end{bmatrix}. \quad (4.32)$$

Note that  $\mathbf{\Gamma}_u$  is built in the same way as  $\mathbf{\Gamma}_l$  with  $\gamma_u$  replacing  $\gamma_l$ , which are defined in Section 4.2.

Given (4.29), we can rewrite  $C_{N_g}$  as

$$C_{N_g} = \frac{1}{N_g} \text{tr}(\text{diag}(\mathbf{c}_\phi)) = \frac{1}{N_g} \boldsymbol{\gamma}_s^T \mathbf{s}_\phi, \quad (4.33)$$

where  $\boldsymbol{\gamma}_s$  is defined by

$$\boldsymbol{\gamma}_s(2N_T \times 1) = \mathbf{\Gamma}_e^T \mathbf{1}_{N_g \times 1}. \quad (4.34)$$

In (4.33),  $C_{N_g}$  is a sum of  $2N_T$  independent non-identically distributed discrete uniform random variables, whose PDF can be approximated by a Normal distribution using the central limit theorem (CLT) [66], so that

$$C_{N_g} \sim \mathcal{CN}\left(0, \frac{\sigma_{so}^2 \boldsymbol{\gamma}_s^H \boldsymbol{\gamma}_s}{N_g^2}\right). \quad (4.35)$$



Hence, if we use the Gaussian approximation, (4.27) can be simplified by

$$MSE = \frac{\sigma_{so}^2 \gamma_s^H \gamma_s}{N_g^2} \sigma_H^2 + \frac{\sigma_w^2}{N_g}. \quad (4.36)$$

However, in a realistic scenario,  $N_T$  is not only a finite number, but also it is probably small, which may make the approximation inaccurate. In order to verify the accuracy of the approximation, we use the Berry-Essen theorem [67] that gives an upper-bound of the maximal error of approximation between the cumulative distribution function (CDF) of the normal distribution  $\Phi(C_{N_g})$  and the true CDF distribution  $F(C_{N_g})$  that we want to approximate, whose expression is given by

$$\varepsilon_{N_g} = \sup_{C_{N_g} \in \text{Re}} |F(C_{N_g}) - \Phi(C_{N_g})| \leq 6 \frac{\sum_{i=0}^{2N_T-1} \rho_i}{\left(\sum_{i=0}^{2N_T-1} \sigma_i^2\right)^{\frac{3}{2}}}, \quad (4.37)$$

where  $\rho_i$  and  $\sigma_i^2$  are defined by

$$\rho_i = \left| \frac{\sqrt{\rho_{so}} [\gamma_s]_i}{N_g} \right|^3, \quad \sigma_i^2 = \left( \frac{\sqrt{\rho_{so}} [\gamma_s]_i}{N_g} \right)^2. \quad (4.38)$$

The result of (4.37) is measured by the Kolmogorov-Smirnov distance [68], so we have to check if this measure satisfies the criteria of Kolmogorov-Smirnov test, which evaluates the similarity of two distributions. According to [68], the approximation is good enough when it satisfies

$$Pr\left(\sqrt{2N_T} \varepsilon_{N_g} \leq U_\alpha\right) = \frac{\sqrt{2\pi}}{U_\alpha} \sum_{i=1}^{\infty} \exp\left(-\frac{\pi^2(2k-1)^2}{8i^2}\right) = 1 - \alpha, \quad (4.39)$$

where  $U_\alpha$  is the confidence margin and  $\alpha$  is typically 5%. Applying (4.39) to our case, it is straightforward to obtain that the result of the Gaussian approximation is accurate even for  $N_T$  as small as 7.

## 4.6 Analysis of the complexity

We evaluate the number of real operations required by our proposals, CPS and BPS, and other previously proposed schemes. Our references for the comparison are AP and DDP, because they are the schemes with the lowest number of required operations in the literature.

Without loss of generality, we only focus on one subcarrier of  $\mathbf{S}_{o,p}$ . In the case of AP [42] and DDP [47], their complexities depend on the number of pilots  $N_d$  placed during  $N$  symbols. On the contrary, CPS and BPS depend on  $N_g$  and  $M$ . Additionally, we also show the case of AP combined with the averaging of every two contiguous estimated channel values (AP2) in order to reduce the noise, which is a very common technique applied in OFDM [69]. In Table 4.2, we show the evaluation of the complexity in terms of number of operations, before applying (4.24). Note that all methods require interpolation so it will add the same complexity.

Focusing on these schemes, DDP has twice the number of operations than AP and AP2. However, according to [47], DDP outperforms AP in terms of SER performance approximately by 2.5dB, which is almost the same improvement achieved by AP2 with half the number of operations.

Before comparing our proposed schemes with these ones, we should guarantee the same processing delay at the receiver side for all the schemes in order to make a fair comparison. This implies that  $N_d = \lceil M/N_g \rceil$  (CPS) and  $\lceil \nu M / (N_b + 2) \rceil$  (BPS) and, in the case of AP and DDP, the estimated channel remains valid for  $N_g$  consecutive symbols. Moreover, we have also adopted this strategy for the simulations results. Under this assumption, it is clear that CPS and BPS require a much lower number of operations compared to the other schemes proposed in the literature. Additionally, as we will see later in Section 4.7, CPS and BPS also outperform AP and AP2 for several values of  $N_g$  in terms of SER. These results make CPS and BPS an ideal candidate for low-consumption devices or delay-sensitive applications.

Table 4.2: Number of real operations per subcarrier.

	#real multiplications	#real adds
AP	$18 \times N_d$	$17 \times N_d$
AP2	$18.5 \times N_d$	$17.5 \times N_d$
DDP	$36 \times N_d$	$38 \times N_d$
CPS	$1 \times \left\lceil \frac{M}{N_g} \right\rceil$	$2(N_g - 1)$
BPS	$1 \times \left\lceil \nu \frac{M}{N_b+2} \right\rceil$	$2(N_b - 1)$

## 4.7 Numerical results

In this section we show some numerical results comparing the performance of AP, CPS and BPS schemes. We have discarded DDP due to the fact that it is a technique with the highest computational complexity, while it has a similar performance in terms of SER to AP2.

### 4.7.1 Simulation Parameters

In table 4.3, we can see the numerical values for the parameters that we defined in the previous sections for CPS and BPS in FBMC-OQAM. We choose EVA channel model [23] for the PDP. Additionally, we model time-variability with the Jakes Doppler spectrum [70], with 100Hz and

5KHz Doppler frequency. The coherence time [34] are 4.23 ms and 84.6  $\mu$ s respectively. Also, according to (3.3), the channel is normalized to  $\sigma_H^2 = 1$ .

Table 4.3: Simulation parameters for CPS and BPS.

<b>K</b>	64	<b>Overlap. Factor</b>	4
<b>K<sub>d</sub></b>	48	<b>Prototype Filter</b>	PHYDYAS
<b>K<sub>p</sub></b>	16	<b><math>\Delta f</math></b>	15 KHz
<b>Channel Model</b>	LTE EVA	<b>Data Constellation</b>	QPSK
4 Slots $\rightarrow$ <b>M</b> = $4 \times 2 \times 7$ FBMC-OQAM symbols			

In the case of AP scheme, we are placing a total of  $4 \times K_p$  pilot symbols ( $2 \times K_p$  traditional and  $2 \times K_p$  auxiliary pilots) for every slot, equally distributed over  $K$  subcarriers.

### 4.7.2 Definition of SNR

The SNR is defined by

$$\text{SNR} = \frac{\mathbb{E} \left\{ |x[n]|^2 \right\}}{\sigma_w^2}. \quad (4.40)$$

Commonly, when comparing schemes with different spectral efficiency (e.g. due to the presence of CP in OFDM [71] or to coding [72]), the performance of the different channel estimation methods is evaluated by a comparison of the SER as a function of the  $E_S/N_0$  ratio, where  $E_S$  is the useful symbol energy and  $N_0$  the noise power spectral density. The computation of  $E_S/N_0$  for the different proposals should take into account the energy wasted by the allocated pilot symbols, which means a reduction of the data efficiency. The expression is given by

$$\frac{E_S}{N_0} = \text{SNR} \frac{B_w}{R_S} \left( 1 - \frac{K_p \times M_p}{K \times M} \right)^{-1}, \quad (4.41)$$

where  $R_S$  and  $B_w$  are the symbol rate and bandwidth respectively, and we assume that  $R_S = B_w$ ;  $N_p$  is the number of pilots per subcarrier in one slot. In the case of AP  $N_p = 16$ , in CPS  $M_p = M$ , and in BPS is  $M_p = \nu \times M$ .

### 4.7.3 Results

In Fig. 4.4, we present the comparative of the MSE, as defined in (4.27), for AP and CPS without considering Doppler effects. Moreover, in order to make a fair comparison, we also averaged two contiguous estimated channel values (AP2). It must be highlighted that results are plotted as a function of  $E_S/N_0$ , and thus, even though CPS and BPS may consider more pilot

symbols, this is accounted in (4.41) for a fair comparison. For all the considered values of  $N_g$ , CPS significantly outperforms AP and AP2. Moreover, we can see that our analytical Gaussian approximation is quite accurate even for  $N_g = 1$ , validating our theoretical analysis.

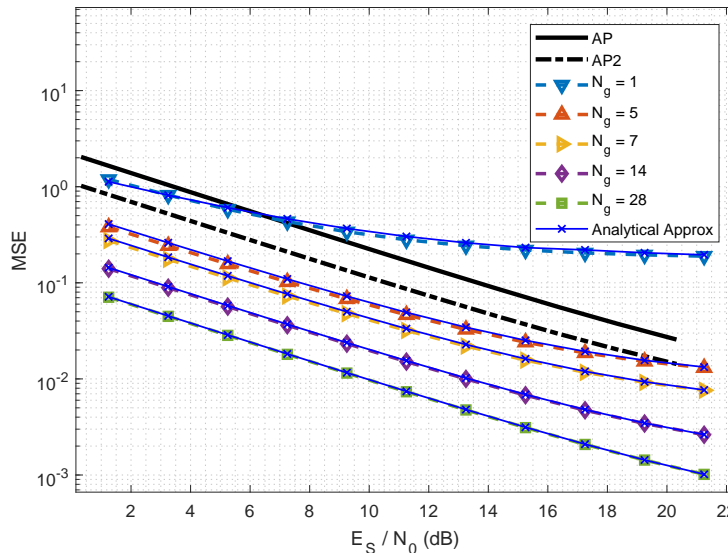


Figure 4.4: MSE comparative of AP and CPS for different values of  $N_g$  and  $7 \times 10^3$  channel realizations without any Doppler effects.

In Fig. 4.5, we show the comparative in terms of SER for AP and CPS without considering Doppler effects. We can see that CPS outperforms AP and AP2 for all the considered values of  $N_g$ . In the best case, CPS with  $N_g = 28$  outperforms AP2 by 2dB. Note that the choice of  $N_g = 28$  corresponds to 2 slots which is the minimum number of contiguous slots that are allocated to a given UE in LTE, making it a feasible value.

In Fig. 4.6, we provide the behavior of BPS, in terms of SER, compared to AP and CPS without considering Doppler effects. Theoretically, according to Section 4.4, if the channel remains quasi-stationary for  $N_c$  symbols and  $N_g$  is the same value for both schemes, the performance also must be the same for both techniques. However, BPS is more efficient than CPS in terms of pilot density  $\nu$ , and therefore, the definition of  $E_S/N_0$  (4.41) benefits BPS improving its performance by almost 1dB compared to CPS.

Additionally, in Fig. 4.7, we provide the same comparative that we have made in Fig. 4.6 with an additional effect of carrier frequency offset (CFO), where  $\epsilon \in [0, 1]$  is the normalized residual CFO at the receiver, after a proper CFO estimation and compensation has been performed. We can see that CFO adds an additional time variability to the system degrading the performance of all techniques. However, CPS provides the best SER thanks to its continuous tracking, and AP approaches are a worse solution than our proposals.

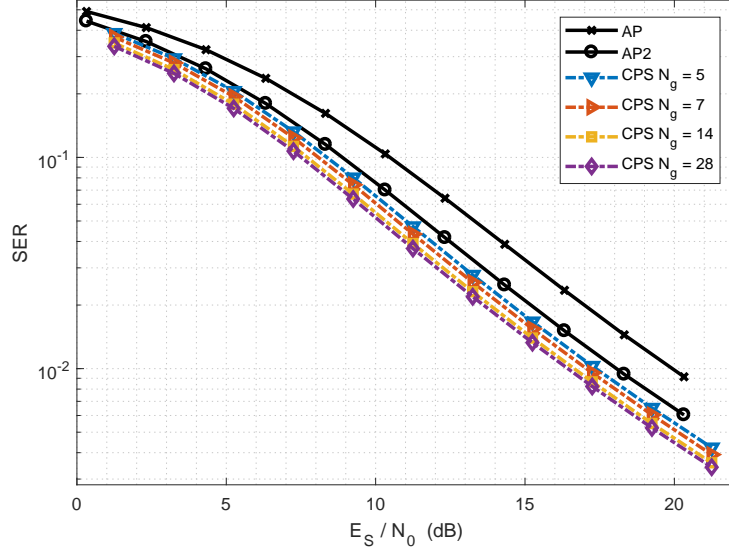


Figure 4.5: SER comparative of AP and CPS for different values of  $N_g$  and  $7 \times 10^3$  channel realizations without any Doppler effects.

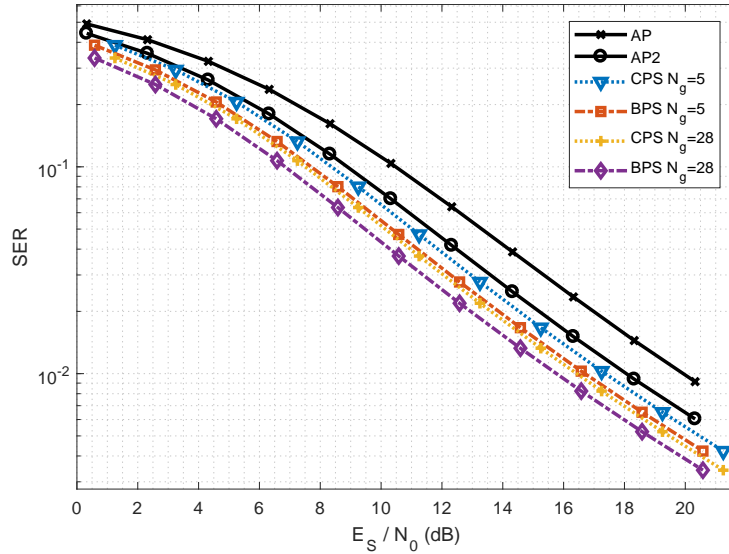


Figure 4.6: SER comparative of AP, CPS and BPS with  $\nu = 0.5$  and  $7 \times 10^3$  channel realizations without any Doppler effects.

In Fig. 4.8, we illustrate the same comparative as in Fig. 4.6 with 100Hz Doppler frequency. In general, the performance suffers a significant degradation for every method compared to the case without any Doppler frequency. Nevertheless, the relative performance remains as in the previous cases. Analogously, our proposals CPS and BPS outperform AP and also BPS provides better results than CPS, as stated before.

In Fig. 4.9, we present the performance of BPS for different values of  $\nu$  with 100Hz Doppler

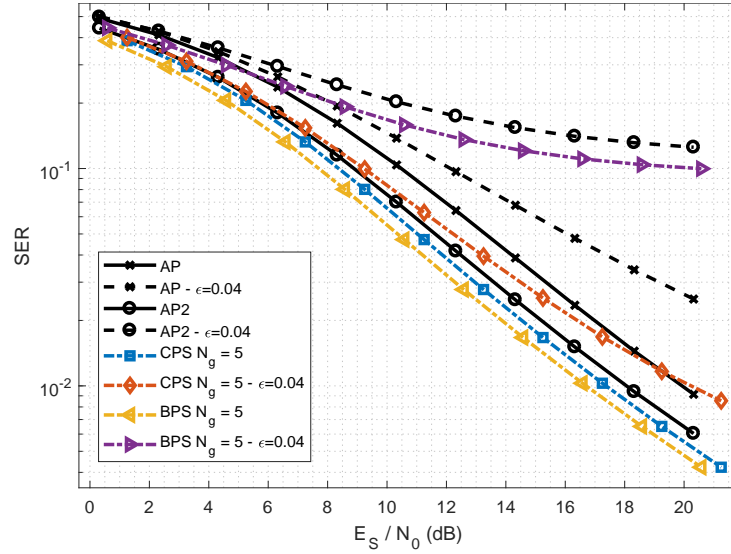


Figure 4.7: SER comparative of AP, CPS and BPS under CFO effects with  $\epsilon = 0.04$ ,  $\nu = 0.5$  and  $7 \times 10^3$  channel realizations without any Doppler effects.

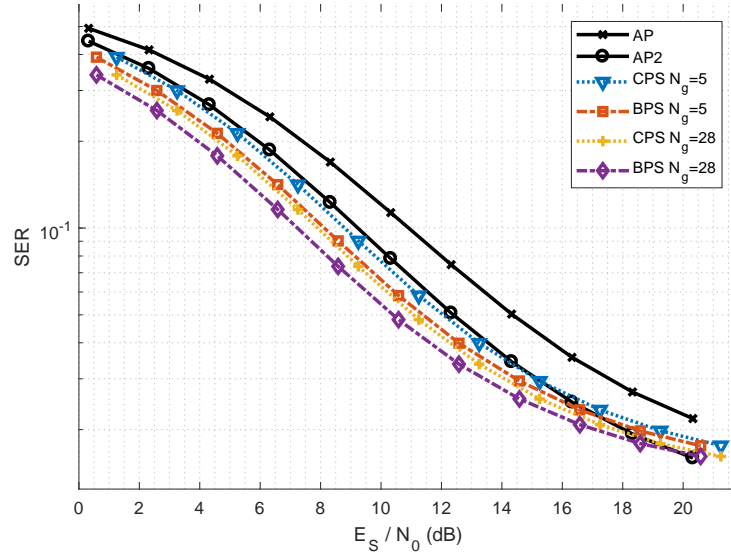


Figure 4.8: SER comparative of AP, CPS and BPS with  $\nu = 0.5$  in the presence of 100Hz Doppler frequency.

frequency. We can see that BPS with  $N_g = 14$  and  $\nu = 0.25$  achieves the same result as BPS with  $N_g = 28$  and  $\nu = 0.5$ . This means that we can not only increment  $N_g$  to improve the behavior, but also we can reduce the pilot density  $\nu$ , which implies the increase of the efficiency in terms of data rate when the channel is slowly-varying.

In Fig. 4.10, we show the comparative of CPS and BPS with 5KHz Doppler frequency which corresponds to a fast time-varying channel. We can clearly see that CPS has the same performance

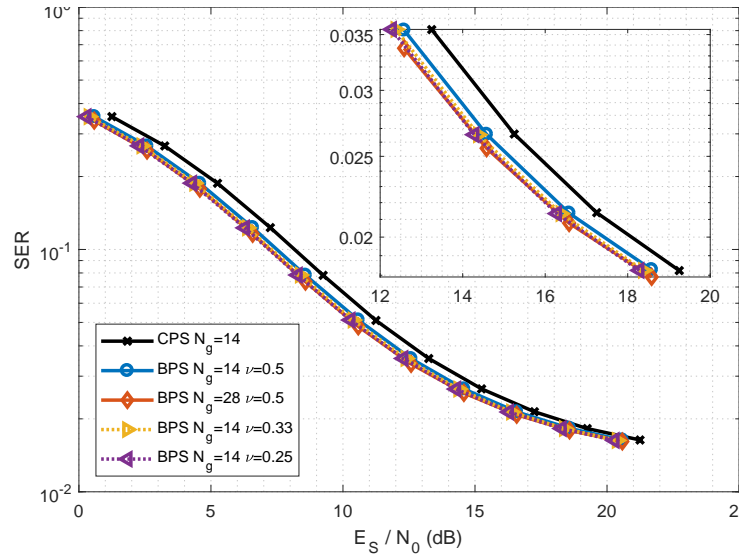


Figure 4.9: SER comparative of CPS and BPS in the presence of 100Hz Doppler frequency.

as BPS for low SNR, however when SNR is high, CPS outperforms all BPS variants. When the channel is very unstable, the continuous channel tracking performed in CPS is crucial, otherwise the performance of the system is compromised.

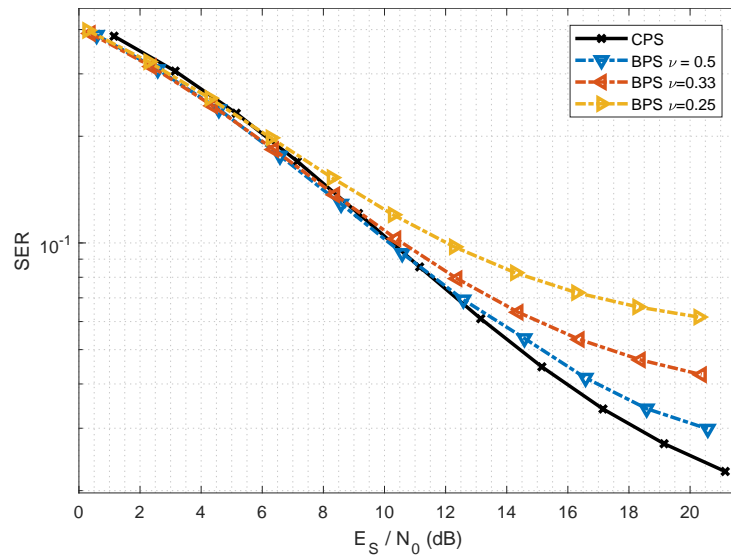


Figure 4.10: SER comparative of CPS and BPS with  $N_g = 14$  in the presence of 5KHz Doppler frequency.

## **4.8 Conclusions**

In this chapter we have proposed a combined technique based on the use of CPS or BPS with FBMC-OQAM. In this combination, we have introduced a specifically designed pilot sequence and an effective low-complexity technique to estimate the channel, which could be applied in any realistic communication system.

Numerical results show that the theoretical analysis using a Gaussian approximation is accurate to compute the channel estimation error. Additionally, they validate the behavior of our proposed system and its improvement compared to AP with its classical pilot scheme.



## Chapter 5

# Low-complexity channel estimation for massive MIMO-OFDM

Channel estimation and equalization are demanding tasks in terms of complexity when MIMO is considered, as we previously mentioned in Chapter 3. After obtaining the estimated channel using the transmitted pilots in several training periods, the estimators are interpolated to all time-frequency resources and a prohibitive channel inversion is required for each resource to get its own equalizer. In order to reduce the overall complexity, there are two independent research lines. The first one consists in replacing the matrix inversion by NS expansion, which is a low-complexity approximation. The second one focuses on exchanging the order of interpolation and channel inversion stages, in order to reduce the number of matrix inversions.

In this chapter, we propose the use of NS to compute the matrix inversion, combined with the linear interpolation of the inverted channel matrix, under the scenario of massive MIMO-OFDM. To the best of our knowledge, this joint scheme has never been proposed before. Note that, we have chosen the linear interpolation method due to the fact that it provides a good trade-off between complexity and performance [73]. Taking advantage of the properties of the channel matrix for the massive MIMO regime, we will show that our proposals, denoted as low-complexity schemes, require a lower number of operations and maintain the performance of the system as good as the TS. Additionally, they are applicable for either TDD or FDD scenarios. We will provide a comparison of the complexity in terms of required operations, and a detailed analytical description of the obtained average square euclidean distance (ASED) between the traditional

scheme and low-complexity schemes, which becomes zero when the number of antennas is large enough. Moreover, we will show some numerical results in terms of ASER, SINR and SER for all schemes that validate the analysis.

The remainder of the chapter is organized as follows. Section 5.1 provides the model of the considered MIMO-OFDM system. Section 5.2 describes the channel estimation and equalization techniques using linear interpolation for the traditional scheme and low-complexity schemes. Section 5.3 and Section 5.4 provide the analysis of the ASER and a comparison of complexity for both schemes, respectively. Section 5.5 presents some numerical results to verify our theoretical analysis and provides a better understanding of the system performance. Finally, in section 5.6, some conclusions are pointed out for this chapter.

## 5.1 System model

In this chapter, we consider a multi-user MIMO-OFDM system (see Fig. 3.3). For illustration purposes, we focus on the UL in TDD mode, where the BS estimates the channel and computes the equalization matrix using the received pilot-symbols, and the BS uses it as both precoding and postcoding matrices. Note that our proposal equally applies for FDD, where the procedure is the same as in TDD for the UL; and for the DL, the UE can compute the equalizer with the same procedure using the pilot-symbols transmitted by the BS, if needed.

### 5.1.1 OFDM

According to Section 3.6, the stream of  $u$ -th UE  $x_u[n]$  is made of consecutive OFDM symbols  $\mathbf{x}_{u,m} ((K + N_{CP}) \times 1)$ ,  $1 \leq m \leq M$ , which is defined as

$$\mathbf{x}_{u,m} = \left[ (\mathbf{x}_{u,m}^{cp})^T \quad (\mathbf{x}_{u,m}^d)^T \right]^T, \quad (5.1)$$

where  $K$  is the number of subcarriers,  $M$  denotes the number of time instants,  $N_{CP}$  represents the length of CP,  $\mathbf{x}_{u,m}^{cp}$  is the CP which is a copy of the last  $N_{CP}$  samples of the data vector  $\mathbf{x}_{u,m}^d$ , whose expression is given by

$$\mathbf{x}_{u,m}^d = \mathbf{F}_K^H \mathbf{s}_{u,m}, \quad (5.2)$$

where  $\mathbf{s}_{u,m}$  is the vector containing the set of  $K$  complex data symbols to be transmitted, and these complex symbols belong to a QAM constellation with unit average power denoted as  $\sigma_s^2 = 1$ . Furthermore, we assume that the length of CP is long enough in order to mitigate the effects of the frequency selective channel ( $N_{CP} \geq N_P - 1$ ).

At the receiver side, assuming perfect synchronization, the received stream at  $v$ -th antenna of the BS  $y_v[n]$ , is split in blocks  $\mathbf{y}_{v,m} ((K + N_{CP}) \times 1)$ ,  $1 \leq m \leq M$ . Then, the CP of each block

is suppressed and the FFT is performed in order to obtain  $\mathbf{r}_{v,m} (K \times 1)$ , which can be modeled as

$$[\mathbf{r}]_{k,m} = \mathbf{H}_{k,m} [\mathbf{s}]_{k,m} + [\mathbf{w}]_{k,m}, \quad \forall k \in \mathcal{A} = \{1, 2, \dots, K\}, \quad (5.3)$$

where  $\mathcal{A}$  represents the set of subcarrier indexes,  $\mathbf{w} (N_v \times 1)$  is the AWGN vector with each element distributed according to  $\mathcal{CN}(0, \sigma_w^2)$  and  $\mathbf{H}_k (N_v \times N_u)$  denotes the channel frequency response matrix with each element given by

$$[\mathbf{H}_{k,m}]_{vu} = [\tilde{\mathbf{h}}_{vu,m}]_k. \quad (5.4)$$

For the sake of simplicity and without loss of generality, we omit the sub-index  $m$  in the following sections of this chapter.

## 5.2 Channel estimation and equalization using linear interpolation

Let us define the subset  $\mathcal{A}_p \subseteq \mathcal{A}$  that contains the  $K_p$  pilot subcarrier indexes, equally spaced over the  $K$  resources, where the distance in the frequency domain between any two contiguous ones is  $N_f$ ; and  $\mathcal{A}_d \subseteq \mathcal{A}$ , where  $\mathcal{A}_p \cap \mathcal{A}_d = \emptyset$ , that contains the  $K - K_p$  data subcarrier indexes.

We assume that the BS will perform a LS method [64], in order to obtain the estimated channel at each pilot position which can be expressed as

$$\hat{\mathbf{H}}_k = \mathbf{H}_k + \Delta\mathbf{H}_k, \quad k \in \mathcal{A}_p, \quad (5.5)$$

where  $\Delta\mathbf{H}_k$  denotes the channel estimation error due to the presence of noise with each element distributed according to  $\mathcal{CN}(0, \sigma_{\Delta H}^2)$ . In our analysis, we assume perfect channel estimation ( $\Delta\mathbf{H}_k = \mathbf{0}_{N_v \times N_u}$ ). However, in the simulation results we will consider the general case ( $\Delta\mathbf{H}_k \neq \mathbf{0}_{N_v \times N_u}$ ).

Once the channel is estimated at  $\mathcal{A}_p$  and interpolated [73] to  $\mathcal{A}_d$ , when ZF criterion is chosen, the equalizer for each subcarrier  $k \in \mathcal{A}_d$  is given by the Moore-Penrose pseudo-inverse as

$$\mathbf{G}_k = \mathbf{Q}_k \mathbf{H}_k^H = (\mathbf{L}_k)^{-1} \mathbf{H}_k^H = (\mathbf{H}_k^H \mathbf{H}_k)^{-1} \mathbf{H}_k^H, \quad \forall k \in \mathcal{A}_d. \quad (5.6)$$

Inspecting (5.6), the most complex element is to compute the inverse of  $\mathbf{L}_k$ . Following [37], we will focus on the different ways to compute  $\mathbf{Q}_k$  in order to reduce the complexity and maintain the performance.

### 5.2.1 Traditional scheme

Once that the channel is estimated at each pilot subcarrier,  $\mathbf{L}_k \forall k \in \mathcal{A}_p$  is computed and linearly interpolated as

$$\begin{aligned} \mathbf{L}_k^{ZF} &= \left(\frac{k-p}{N_f}\right) \mathbf{L}_q + \left(1 - \frac{k-p}{N_f}\right) \mathbf{L}_p, \\ q &= p + N_f, \quad \forall \{q, p\} \in \mathcal{A}_p \quad p < k < q, \quad \forall k \in \mathcal{A}_d. \end{aligned} \quad (5.7)$$

Then,  $\mathbf{Q}_k^{ZF}$ ,  $\forall k \in \mathcal{A}_d$  is computed according to

$$\mathbf{Q}_k^{ZF} = \frac{\text{adj}(\mathbf{L}_k^{ZF})}{\det(\mathbf{L}_k^{ZF})}, \quad \forall k \in \mathcal{A}_d, \quad (5.8)$$

where

$$\det(\mathbf{L}_k) = \sum_{b=1}^{N_u} (-1)^{a+b} [\mathbf{L}_k]_{a+b} \det(\mathbf{L}_k^{(a,b)}), \quad 1 < a < N_u, \quad (5.9)$$

$$[\text{adj}(\mathbf{L}_k)]_{a,b} = (-1)^{a+b} \det(\mathbf{L}_k^{(a,b)}), \quad 1 < a, b < N_u, \quad (5.10)$$

and  $\mathbf{L}_k^{(a,b)}$  is obtained by removing the  $a$ -th row and  $b$ -th column of  $\mathbf{L}_k$ .

Commonly, (5.8) is computed by applying the Gauss-Jordan (GJ) elimination method on  $\mathbf{L}_k^{ZF}$ . Hence, we denote this scheme as ZF-GJ.

### 5.2.2 Proposed low-complexity schemes

In the low-complexity schemes,  $\mathbf{Q}_k^{ZF} \forall k \in \mathcal{A}_p$  is firstly computed. Then, the linear interpolation is applied as

$$\begin{aligned} \mathbf{Q}_k^{LZF} &= \left(\frac{k-p}{N_f}\right) \mathbf{Q}_q^{ZF} + \left(1 - \frac{k-p}{N_f}\right) \mathbf{Q}_p^{ZF} = \left(\frac{k-p}{N_f}\right) (\mathbf{L}_q^{ZF})^{-1} + \left(1 - \frac{k-p}{N_f}\right) (\mathbf{L}_p^{ZF})^{-1} = \\ &= \left(\frac{k-p}{N_f}\right) \frac{\text{adj}(\mathbf{L}_q^{ZF})}{\det(\mathbf{L}_q^{ZF})} + \left(1 - \frac{k-p}{N_f}\right) \frac{\text{adj}(\mathbf{L}_p^{ZF})}{\det(\mathbf{L}_p^{ZF})}, \\ q &= p + N_f, \quad \forall \{q, p\} \in \mathcal{A}_p \quad p < k < q, \quad \forall k \in \mathcal{A}_d, \end{aligned} \quad (5.11)$$

where  $LZF$  stands for low-complexity ZF. Note that, comparing to traditional scheme, the number of inversions is reduced from  $K$  to  $K_p$  in low-complexity schemes.

Additionally, instead of using the GJ method, we can use the NS to obtain a good approximation with an even more reduced complexity. NS is a generalization of geometric series and it is used to solve Fredholm integrals by approximation. Taking this approach, the inverted channel matrix can also be rewritten by a polynomial expansion (simple matrix multiplications and summations). According to [38], we also constrain the NS to only two terms, so the inversion can be expressed as

$$\mathbf{Q}_k^{ZF} \approx 2\mathbf{T}_k^{-1} - \mathbf{T}_k^{-1} \mathbf{L}_k^{ZF} \mathbf{T}_k^{-1}, \quad \forall k \in \mathcal{A}_p, \quad (5.12)$$

where  $\mathbf{T}_k$  is the precondition matrix, whose design is crucial to obtain a trade-off between complexity and quality of the matrix inversion. Note that, [74] has shown that the approximation error of (5.12) is negligible, and we will not provide more details that can be found in [74].

For illustration purposes and the sake of conciseness, we choose only two NS schemes, namely diagonal NS (DNS) [74] and tri-diagonal (TNS) [75], among all existing ones. Note that, any NS scheme can be applied in our proposal. Hence,  $\mathbf{T}_k$  for both cases can be expressed as

$$\mathbf{T}_k^{DNS} = \text{diag}_0(\mathbf{L}_k^{ZF}), \quad (5.13)$$

$$\mathbf{T}_k^{TNS} = \text{diag}_0(\mathbf{L}_k^{ZF}) + \text{diag}_1(\mathbf{L}_k^{ZF}), \quad (5.14)$$

respectively, where

$$[\text{diag}_n(\mathbf{L}_k)]_{u,v} = \begin{cases} [\mathbf{L}_k]_{u,v} & |u-v| = n \\ 0 & \text{otherwise} \end{cases}. \quad (5.15)$$

Finally, the combination of the interpolation of the inverted channel (5.11) with GJ, DNS and TNS, are denoted as LZF-GJ, LZF-DNS and LZF-TNS, respectively.

### 5.3 Asymptotic analysis of the average square euclidean distance (ASED)

We define the ASED denoted by  $\epsilon$  between the traditional scheme and low-complexity schemes as

$$\epsilon = \frac{1}{K - K_p} \sum_{k \in \mathcal{A}_d} \mathbb{E} \left\{ \left\| \mathbf{Q}_k^{ZF} - \mathbf{Q}_k^{LZF} \right\|_F^2 \right\}. \quad (5.16)$$

Given (5.8) and (5.11), the two schemes would have the same performance if the channel matrix were the same for all pilot and data positions, so that

$$\mathbf{H}_p = \mathbf{H}_q \implies \mathbf{L}_p = \mathbf{L}_q \iff \epsilon = 0, \quad q = p + N_f, \quad \forall \{q, p\} \in \mathcal{A}_p. \quad (5.17)$$

However,  $\mathbf{H}_p = \mathbf{H}_q$  is not possible in real scenarios because the channel is frequency-selective.

Given the fact that  $\mathbf{H}_p \neq \mathbf{H}_q$ , (5.16) becomes unmanageable due to the presence of a large number of terms. However, it might be reduced for massive MIMO, by increasing the number of antennas at the BS to satisfy  $N_v \gg N_u$ . Under this scenario, we can perform the following asymptotic analysis. According to [29],  $\frac{1}{N_v} \mathbf{L}_q^{ZF}$  and  $\frac{1}{N_v} \mathbf{L}_p^{ZF}$  follow a Wishart distribution and they converge to the identity matrix for a large number of antennas, so they satisfy that

$$\frac{1}{N_v} \mathbf{L}_q^{ZF}, \frac{1}{N_v} \mathbf{L}_p^{ZF} \xrightarrow{N_v \gg N_u} \mathbf{I}_{N_u} \implies \epsilon \xrightarrow{N_v \gg N_u} 0. \quad (5.18)$$

Hence, we can see that when the number of antennas at the BS is much larger than the number of UEs, the difference between using the traditional scheme and low-complexity schemes is asymptotically negligible, where the low-complexity schemes require a lower number of operations as we see in the following section.

We analyze numerically the ASER between traditional scheme and low-complexity schemes in Section 5.5 to verify how many antennas are required for the conditions of (5.18) to hold.

## 5.4 Analysis of the complexity

In Table 5.1 we show the computational complexity of the schemes presented in the previous sections. The complexity is evaluated in terms of the required number of complex multiplications (NCM), since it is the most frequently used metric.

Table 5.1: Comparison of the complexity in terms of NCM

Technique	NCM
ZF-GJ	$K((N_u^3 + N_u^2) + 2N_v N_u^2)$
LZF-GJ	$K_p((N_u^3 + N_u^2) + 2N_v N_u^2)$
LZF-DNS	$K_p(N_u^2 + 2N_v N_u^2)$
LZF-TNS	$K_p(6N_u^2 + 2N_v N_u^2)$

The first term of the sum for all cases accounts for the computation of  $\mathbf{Q}_k$  (based on [38]). The second term accounts for the computation of  $\mathbf{L}_k$  and the multiplication by  $\mathbf{H}_k^H$  (see (5.6)). Comparing them, any of the low-complexity schemes requires a lower NCM than the traditional scheme, since not only it requires less operations in the inversion, but also we are only performing  $K_p$  matrix inversion operations instead of  $K$ , as we mentioned before.

Note that the complexity related to the linear interpolation is not taken into account, because the NCM of these operations are the same for all techniques, and also they are negligible compared to the matrix inversion.

## 5.5 Numerical results

In this section we show some numerical results comparing the performance of our proposed low-complexity schemes with the traditional scheme [73][76].

We define the SNR as

$$\text{SNR} = \frac{N_u}{\sigma_w^2}. \quad (5.19)$$

After equalization, the SINR averaged over all UEs can be expressed as

$$\text{SINR} = \frac{1}{N_u} \sum_{u=1}^{N_u} \frac{\text{SNR}}{N_v} \frac{1}{[\mathbf{Q}_k]_{u,u}}, \quad k \in \mathcal{A}_d. \quad (5.20)$$

Assuming that the pilots and symbols have the same power, we set  $\sigma_{\Delta H}^2 = \sigma_w^2$ .

In Table 5.2, we can see the default numerical values for the parameters that we defined in the previous sections. We choose EVA channel model [23] for the PDP, and we consider spatially uncorrelated channels.

Table 5.2: Simulation parameters for low-complexity ZF equalization.

<b><math>K</math></b>	128	<b><math>M</math></b>	7
<b><math>\Delta f</math></b>	15 KHz	<b><math>N_f</math></b>	8
<b><math>N_v</math></b>	10, 100	<b><math>N_p</math></b>	5
<b><math>N_u</math></b>	2	<b><math>N_{CP}</math></b>	9
<b>Channel Model</b>	LTE EVA	<b>Constellation</b>	QPSK

### 5.5.1 Verification of the theoretical analysis of the ASED

Fig. 5.1 provides the curves of ASED for different values of  $N_v$  for  $N_u = 2, 4$  and  $8$  when  $\Delta \mathbf{H}_k = \mathbf{0}_{N_v \times N_u}$ . We can see that when the condition  $N_v \gg N_u$  is satisfied, no matter how many UEs there are, the ASED of all of the schemes tends to zero, so that our proposed low-complexity schemes provide the same performance as the traditional scheme with lower number of operations. Additionally, note that even for the worst case of LZFDNS with  $N_u = 8$  and  $N_v = 30$ , the ASED  $\approx 10^{-5}$ , which shows that low-complexity schemes do not really need a very large number of antennas at the BS in order to get an acceptable error.

### 5.5.2 Verification of the complexity

In Fig. 5.2, we show the complexity comparison for different values of  $N_v$  in terms of NCM using the expression of Table 5.1, for  $N_u = 2$  and  $8$  and  $K_p = 8$ . We can see that any proposed low-complexity scheme outperforms the traditional one in one magnitude order.

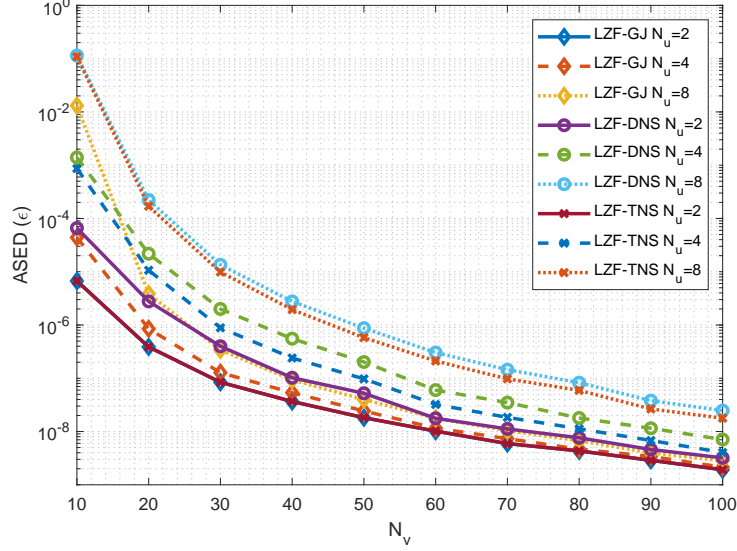


Figure 5.1: ASED between traditional scheme and low-complexity schemes for  $N_u = 2, 4$  and  $8$  when  $\Delta\mathbf{H}_k = \mathbf{0}_{N_v \times N_u}$ .

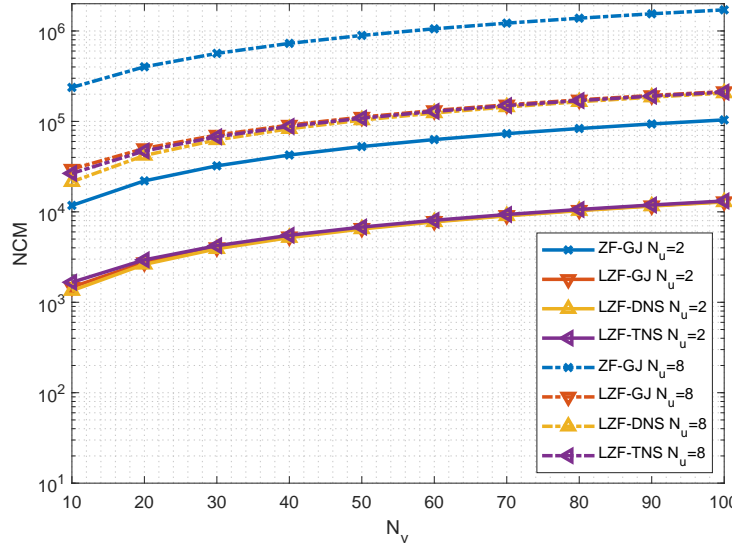


Figure 5.2: Comparison of complexity in terms of NCM for  $K_p = 8$  and  $N_u = 2$  and  $8$ .

### 5.5.3 Performance comparison

Fig. 5.3 represents the SER for all techniques when  $N_v = 10$  and  $\sigma_{\Delta\mathbf{H}}^2 = \sigma_w^2$ . We can see that no matter which matrix inversion technique is used, our low-complexity schemes and the traditional scheme have the same performance in terms of SER, verifying that the benefits of our proposal are also kept under the presence of noise in the channel estimation process.

Fig. 5.4 and 5.5 provide the SINR after equalization for all the techniques for  $N_v = 10$  and



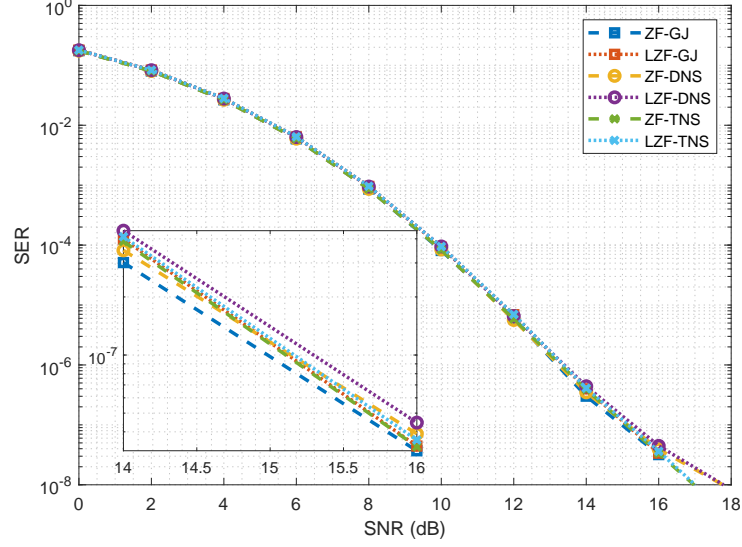


Figure 5.3: SER performance results for  $\sigma_{\Delta \mathbf{H}}^2 = \sigma_w^2$  and  $N_v = 10$ .

100, respectively. Same conclusions can be obtained regarding the performance as in Fig. 5.3, where the difference between the traditional scheme and low-complexity schemes, for the high SNR regime, are approximately 0.4dB and 0.2dB, respectively. These results are an alternative way to show that the ASER between the traditional scheme and our proposed ones is reduced as the  $N_v \gg N_u$ . We can also see, that DNS is worse than GJ and TNS for  $N_v = 10$  and moderate to high SNR. However, when  $N_v = 100$ , all the inversion techniques have practically the same performance.

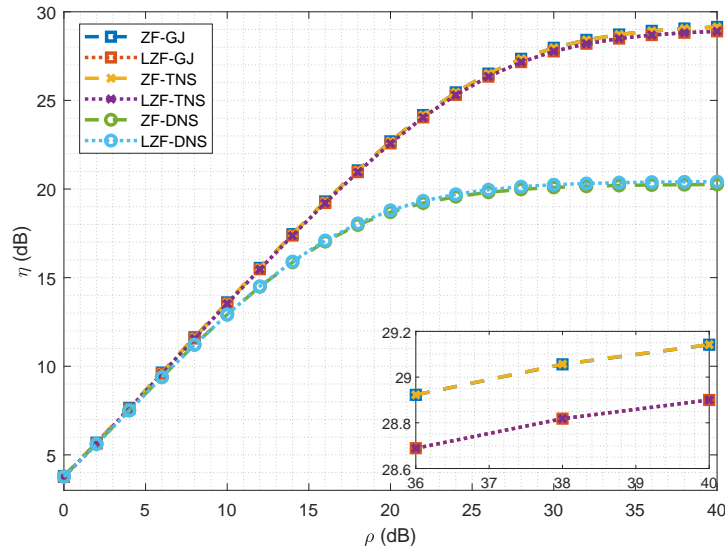


Figure 5.4: SINR performance results for  $\sigma_{\Delta \mathbf{H}}^2 = \sigma_w^2$  and  $N_v = 10$ .

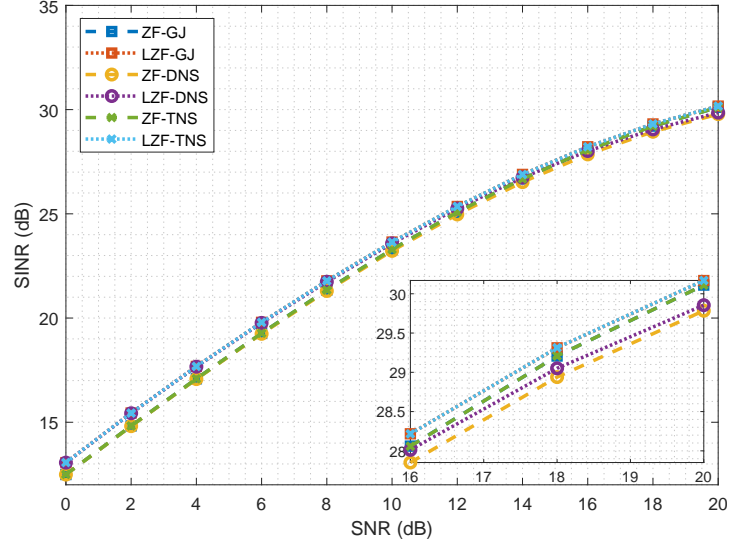


Figure 5.5: SINR performance results for  $\sigma_{\Delta\mathbf{H}}^2 = \sigma_w^2$  and  $N_v = 100$ .

## 5.6 Conclusions

In this chapter we have proposed low-complexity schemes to compute the ZF equalizer for massive MIMO-OFDM, which consist in the efficient combination of computing matrix inversions using NS with the interpolation of these inverted matrices. The numerical results, in terms of SINR and SER, have shown that our proposal requires a significantly lower computational complexity while maintaining the same performance as the traditional scheme. The proposed schemes are useful for the practical implementation of systems that combine OFDM and massive MIMO.

## Chapter 6

# Low-rank channel estimation for mmWave

Channel estimation in mmWave bands is a difficult task because the propagation of the signal is quite unstable due to the high carrier frequencies. However, the channel model can be considered sparse thanks to the narrow beams, where only few paths must be estimated. Several existing estimation techniques for mmWave not only do not adapt to the different SNR conditions, but also they are parametric approaches, where channel calibration is required. Recently, [54] proposed a non-parametric approach, where channel calibration is no longer needed, and it also exploits the LR algebraic structure of the channel by projecting the estimated channel on the independent ST covariance matrices.

In this chapter we will improve the performance of the LR estimated channel given in [54], where we assume the same system model and assumptions. A multi-slot scenario is used, where the slow-varying components of the channel response (angles and delays) are estimated, while the fast-varying ones (fading coefficients) are tracked at each slot. Unlike [54], we obtain a joint ST covariance matrix, which is capable of obtaining the full ST features of the massive multiple antenna scenario. Moreover, given the computed joint ST covariance matrix, we propose three estimation methods of DoA and ToA considering a semi-parametric spatial response and delay estimation. The first method is based on one dimension (1D) multiple signal classification (MUSIC) [77] algorithm, that it is a low-complexity method that provides a very good performance in high SNR scenarios. The second method is based on iterative maximum likelihood estimation (MLE) [78], where it provides a very good performance in any scenario. However, its complexity is higher than the previous one. Hence, the third method is the hybrid one, which combines the previous two methods and is capable of obtaining a good performance with a reduced complexity. Finally,

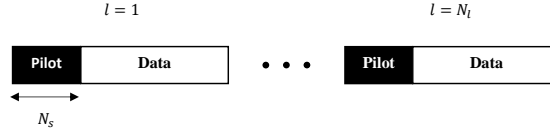


Figure 6.1: Multiple antenna scenario.

we also propose an automatic rank selection (ARS) method which is able to select the best LR channel estimation each scenario based on the computation of the MSE.

The remainder of the chapter is organized as follows. Section 6.1 provides the model of the considered multiple antenna scenario. Section 6.2 describes the estimation of the joint ST covariance matrix. Section 6.3 provides the different methods for the estimation of DoA and ToA. Section 6.4 describes the ARS method. Section 6.5 presents some numerical results to verify our theoretical analysis and provides a better understanding of the system performance. Finally, in section 6.6, some conclusions are pointed out for this chapter.

## 6.1 System model

We consider a time-slotted wireless communication system (see Fig. 6.1) where a single-antenna UE ( $N_u = 1$ ) transmits data to a BS equipped with  $N_v$  antennas. The received signal at the BS in the  $l$ -th pilot sequence  $\mathbf{Y}(l)$  ( $N_v \times N_s$ ) out of  $N_l$  pilot sequences is given by

$$\mathbf{Y}(l) = \mathbf{H}(l) \mathbf{X}(l) + \mathbf{W}(l), \quad (6.1)$$

where  $\mathbf{H}(l)$  ( $N_v \times N_t$ ) is the block-fading frequency-selective single-input multiple-output (SIMO) channel with temporal support  $N_t$ ,  $\mathbf{X}(l)$  ( $N_t \times N_s$ ) denotes the training sequence of length  $N_s$  organized in a form of  $N_t$  one sample-delayed replicas and  $\mathbf{W}(l)$  ( $N_v \times N_s$ ) =  $[\mathbf{w}_1(l) \ \cdots \ \mathbf{w}_{N_v}(l)]$  denotes the AWGN, and we assume that the noise is temporally and spatially uncorrelated. Hence,  $\mathbb{E}\{\mathbf{w}_i(l) \mathbf{w}_{i+m}^H(l)\} = \delta(m) \sigma_w^2 \mathbf{I}_{N_v}$ , where we consider that all antennas have the same noise power  $\sigma_w^2$ .

The channel  $\mathbf{H}(l)$  can be modeled as

$$\mathbf{H}(l) = \mathbf{A} \mathbf{D}(l) \mathbf{G}^T, \quad (6.2)$$

where

$$\mathbf{D}(l) (N_p \times N_p) = \text{diag}(\mathbf{d}(l)), \quad (6.3)$$

and  $\mathbf{d}(l)$  is a vector that contains the  $N_p$  coefficients of the multi-path channel, according to (3.3), it is distributed as

$$\mathbf{d}(l) (N_p \times 1) \sim \mathcal{CN}(\mathbf{0}_{N_p \times 1}, \mathbf{\Sigma}_d), \quad (6.4)$$

$$\boldsymbol{\Sigma}_d = \mathbb{E} \left\{ \mathbf{d}(l) (\mathbf{d}(l))^H \right\} = \text{diag} \left( \left[ \sigma_{d_1}^2, \dots, \sigma_{d_{N_p}}^2 \right] \right). \quad (6.5)$$

Additionally,  $\mathbf{A}$  and  $\mathbf{G}$  are defined as

$$\mathbf{A} (N_v \times N_p) = \begin{bmatrix} \mathbf{a}_1 & \cdots & \mathbf{a}_{N_p} \end{bmatrix}, \quad (6.6)$$

$$\mathbf{G} (N_t \times N_p) = \begin{bmatrix} \mathbf{g}_1 & \cdots & \mathbf{g}_{N_p} \end{bmatrix}, \quad (6.7)$$

where  $\mathbf{a}_i = \mathbf{a}(\theta_i)$  denotes the array response of the BS at the  $i$ -th tap, and  $\mathbf{g}_i = \mathbf{g}(\tau_i) = [\mathbf{g}_\alpha(\tau - \tau_i)]_{\downarrow \alpha}$  represents the convolution of the transmitter pulse and the matched filter at the receiver side of the  $i$ -th tap, where  $\alpha$  is the decimation factor. Note that we assume that the shape of  $\mathbf{g}_i$  is perfectly known. However,  $\tau_i$  and  $\mathbf{a}_i$  are completely unknown and they must be estimated.

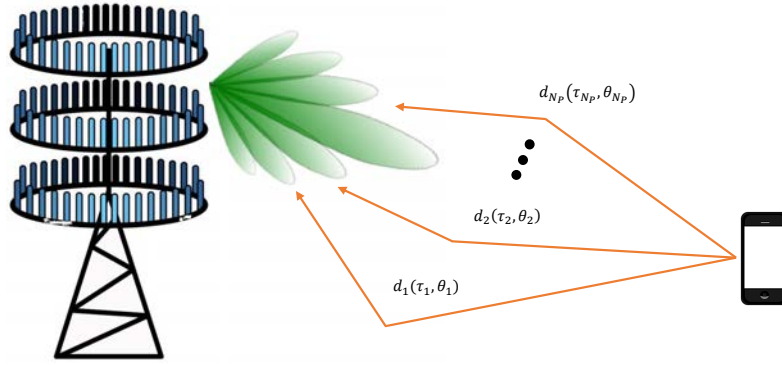


Figure 6.2: Multiple antenna scenario.

Given (6.1), the MLE of the channel in the  $l$ -pilot block is given as

$$\widehat{\mathbf{H}}(l) = \mathbf{R}_{yx}(l) \mathbf{R}_{xx}^{-1} = \mathbf{H}(l) + \Delta \mathbf{H}(l), \quad (6.8)$$

$$\mathbf{R}_{yx}(l) = \frac{1}{N_s} \mathbf{Y}(l) \mathbf{X}^H(l), \quad (6.9)$$

$$\mathbf{R}_{xx} = \frac{1}{N_s} \mathbf{X}(l) \mathbf{X}^H(l). \quad (6.10)$$

The MSE of the channel estimation  $\sigma_{\Delta h}^2$  can be derived as

$$\sigma_{\Delta h}^2 = \mathbb{E} \left\{ \left\| \widehat{\mathbf{H}}(l) - \mathbf{H}(l) \right\|_F^2 \right\} = \text{tr} \left( \mathbb{E} \left\{ \Delta \mathbf{h}(l) \Delta \mathbf{h}^H(l) \right\} \right) = \frac{N_v \sigma_n^2}{N_s} \text{tr} \left( \mathbf{R}_{xx}^{-1} \right), \quad (6.11)$$

where  $\Delta \mathbf{h}(l) = \text{vec} \left( \widehat{\mathbf{H}}(l) - \mathbf{H}(l) \right)$ .

## 6.2 Estimation of the joint ST covariance matrix

Given (6.2), its vectored version is given by

$$\mathbf{h}(l) (N_h \times 1) = \text{vec} \left( \mathbf{H}(l) \right) = (\mathbf{G} \odot \mathbf{A}) \mathbf{d}(l) = \mathbf{S} \mathbf{d}(l), \quad (6.12)$$

where  $N_h = N_v N_t$  and

$$\mathbf{S}(N_h \times N_p) = \begin{bmatrix} \mathbf{g}_1 \otimes \mathbf{a}_1 & \dots & \mathbf{g}_{N_p} \otimes \mathbf{a}_{N_p} \end{bmatrix}. \quad (6.13)$$

The joint ST covariance matrix of  $\hat{\mathbf{h}}(l) = \mathbf{h}(l) + \Delta \mathbf{h}(l)$  can be defined as

$$\boldsymbol{\Sigma}_{\hat{\mathbf{h}}} = \mathbb{E} \left\{ \hat{\mathbf{h}}(l) \hat{\mathbf{h}}^H(l) \right\} = \boldsymbol{\Sigma}_h + \boldsymbol{\Sigma}_{\Delta h}, \quad (6.14)$$

where

$$\boldsymbol{\Sigma}_h = \mathbb{E} \left\{ \mathbf{h}(l) \mathbf{h}^H(l) \right\} = \mathbf{S} \boldsymbol{\Sigma}_d \mathbf{S}^H = \mathbf{V} \boldsymbol{\Lambda} \mathbf{V}^H = \sum_{i=1}^{N_h} \lambda_i v_i v_i^H = \sum_{i=1}^{N_p} \lambda_i v_i v_i^H = \mathbf{V}_S \boldsymbol{\Lambda}_S \mathbf{V}_S^H, \quad (6.15)$$

where we can see that only  $N_p$  out of  $N_h$  eigen-values are different from zero. This fact enables the reduction of the noise by using a subspace technique.

Applying  $\mathbf{V}^H \mathbf{V} = \mathbf{I}_{N_h}$ , (6.14) can be developed as

$$\boldsymbol{\Sigma}_{\hat{\mathbf{h}}} = \mathbf{V} \boldsymbol{\Lambda} \mathbf{V}^H + \frac{\sigma_{\Delta h}^2}{N_h} \mathbf{I}_{N_h} = \mathbf{V} \left( \boldsymbol{\Lambda} + \frac{\sigma_{\Delta h}^2}{N_h} \mathbf{I}_{N_h} \right) \mathbf{V}^H. \quad (6.16)$$

Regarding (6.15),  $\mathbf{V} = \begin{bmatrix} \mathbf{V}_S & \mathbf{V}_{\Delta} \end{bmatrix}$  and

$$\boldsymbol{\Lambda} + \frac{\sigma_{\Delta h}^2}{N_h} \mathbf{I}_{N_h} = \begin{bmatrix} \boldsymbol{\Lambda}_S & \mathbf{0}_{N_p \times (N_h - N_p)} \\ \mathbf{0}_{(N_h - N_p) \times N_p} & \mathbf{0}_{(N_h - N_p) \times (N_h - N_p)} \end{bmatrix} + \frac{\sigma_{\Delta h}^2}{N_h} \begin{bmatrix} \mathbf{I}_{N_p} & \mathbf{0}_{N_p \times (N_h - N_p)} \\ \mathbf{0}_{(N_h - N_p) \times N_p} & \mathbf{I}_{(N_h - N_p)} \end{bmatrix}. \quad (6.17)$$

Therefore, (6.16) can be derived as

$$\boldsymbol{\Sigma}_{\hat{\mathbf{h}}} = \mathbf{V}_S \left( \boldsymbol{\Lambda}_S + \frac{\sigma_{\Delta h}^2}{N_h} \mathbf{I}_{N_p} \right) \mathbf{V}_S^H + \frac{\sigma_{\Delta h}^2}{N_h} \mathbf{V}_{\Delta} \mathbf{V}_{\Delta}^H = \mathbf{V}_S \boldsymbol{\Lambda}'_S \mathbf{V}_S^H + \frac{\sigma_{\Delta h}^2}{N_h} \mathbf{V}_{\Delta} \mathbf{V}_{\Delta}^H. \quad (6.18)$$

Inspecting (6.12) and (6.18), we can see that  $\mathbf{S}$  and  $\mathbf{V}_S$  belong to the same subspace, due to the fact that both of them contain the full information of all DoA and ToA of each tap.

However, in a realistic scenario, we do not have as many slots as needed in order to compute (6.16). Hence, given  $N_l$  slots, the estimated version of (6.16) is given by

$$\hat{\boldsymbol{\Sigma}}_{\hat{\mathbf{h}}} = \frac{1}{N_l} \sum_{l=1}^{N_l} \hat{\mathbf{h}}(l) \hat{\mathbf{h}}^H(l) = \hat{\mathbf{V}} \hat{\boldsymbol{\Lambda}}' \hat{\mathbf{V}}^H = \hat{\mathbf{V}}_S \hat{\boldsymbol{\Lambda}}'_S \hat{\mathbf{V}}_S^H + \hat{\mathbf{V}}_{\Delta} \hat{\boldsymbol{\Lambda}}_{\Delta} \hat{\mathbf{V}}_{\Delta}^H. \quad (6.19)$$

### 6.3 Estimation of DoA and ToA

In order to obtain the DoA and the ToA of each tap, we must obtain  $\hat{\mathbf{S}}$ , which requires to solve the following LS minimization problem

$$\min_{\mathbf{a}_i, \tau_i, \mathbf{d}(l)} \sum_{l=1}^{N_l} \left\| \hat{\mathbf{h}}(l) - \mathbf{S} \mathbf{d}(l) \right\|_F^2. \quad (6.20)$$

Placing  $\widehat{\mathbf{d}}(l) = (\mathbf{S}^H \mathbf{S})^{-1} \mathbf{S}^H \widehat{\mathbf{h}}(l)$  in (6.20), the argument of the minimization problem can be transformed as

$$\sum_{l=1}^{N_l} \left\| \widehat{\mathbf{h}}(l) - \mathbf{P}_S \widehat{\mathbf{h}}(l) \right\|_F^2 = \sum_{l=1}^{N_l} \left\| \mathbf{P}_S^\perp \widehat{\mathbf{h}}(l) \right\|_F^2 = \sum_{l=1}^{N_l} \text{tr} \left( \widehat{\mathbf{h}}^H(l) \mathbf{P}_S^\perp \widehat{\mathbf{h}}(l) \right), \quad (6.21)$$

where  $\mathbf{P}_S = \mathbf{S} (\mathbf{S}^H \mathbf{S})^{-1} \mathbf{S}^H$  is the matrix projector of  $\mathbf{S}$  and  $\mathbf{P}_S^\perp = \mathbf{I}_{N_p} - \mathbf{P}_S$  is its orthogonal matrix projector.

Using (6.21) and the property  $\text{tr}(\mathbf{AB}) = \text{tr}(\mathbf{BA})$ , (6.20) can be simplified as

$$\min_{\mathbf{a}_i, \tau_i} \text{tr} \left( \mathbf{P}_S^\perp \sum_{l=1}^{N_l} \widehat{\mathbf{h}}(l) \widehat{\mathbf{h}}^H(l) \right) = \min_{\mathbf{a}_j, \tau_j} \text{tr} \left( \mathbf{P}_S^\perp \widehat{\Sigma}_{\widehat{\mathbf{h}}} \right). \quad (6.22)$$

Inspecting (6.22), we can see that the true  $\mathbf{S}$  will guarantee that projecting the estimated joint ST covariance matrix  $\widehat{\Sigma}_{\widehat{\mathbf{h}}}$  in the orthogonal projector of  $\mathbf{S}$  ( $\mathbf{P}_S^\perp$ ) will produce a global minimum.

### 6.3.1 MUSIC-1D method

Given (6.22), we realize that it is very complicated to optimize it in terms of  $\mathbf{S}$ . Hence, as we mentioned before, using the property that  $\mathbf{S}$  and  $\widehat{\mathbf{V}}_S$  belong to the same subspace, an equivalent minimization problem to (6.22) can be formulated as

$$\min_{\mathbf{a}_i, \tau_i} \left\| \mathbf{S} - \mathbf{P}_{\widehat{\mathbf{V}}_S} \mathbf{S} \right\|_F^2, \quad \text{s.t. } \|\mathbf{a}_i\| = 1. \quad (6.23)$$

Note that we added a constraint to our minimization problem in order to avoid the trivial solution.

The argument of (6.23) can be simplified as

$$\left\| \mathbf{S} - \mathbf{P}_{\widehat{\mathbf{V}}_S} \mathbf{S} \right\|_F^2 = \left\| \mathbf{P}_{\widehat{\mathbf{V}}_S}^\perp \mathbf{S} \right\|_F^2 = \text{tr} \left( \mathbf{S}^H \mathbf{P}_{\widehat{\mathbf{V}}_S}^\perp \mathbf{S} \right) = \text{tr} \left( \mathbf{P}_{\widehat{\mathbf{V}}_S}^\perp \mathbf{S} \mathbf{S}^H \right), \quad (6.24)$$

where we use that

$$\mathbf{P}_{\widehat{\mathbf{V}}_S}^\perp = \mathbf{I}_{N_h} - \widehat{\mathbf{V}}_S \widehat{\mathbf{V}}_S^H = \widehat{\mathbf{V}}_\Delta \widehat{\mathbf{V}}_\Delta^H = \mathbf{P}_{\widehat{\mathbf{V}}_\Delta}. \quad (6.25)$$

Inspecting in (6.24), we can clearly see that it is quadratic in  $\mathbf{S}$ , reducing the complexity of the minimization problem. Moreover, the trace operator decouples (6.24) into the sum of  $N_p$  cost functions as

$$\sum_{i=1}^{N_p} f(\mathbf{a}_i, \tau_i) = \text{tr} \left( \mathbf{S}^H \mathbf{P}_{\widehat{\mathbf{V}}_\Delta} \mathbf{S} \right) = \sum_{i=1}^{N_p} \mathbf{s}_i^H \mathbf{P}_{\widehat{\mathbf{V}}_\Delta} \mathbf{s}_i. \quad (6.26)$$

Using the definition given in (6.13),  $f(\mathbf{a}_i, \tau_i)$  can be manipulated as

$$f(\mathbf{a}_i, \tau_i) = (\mathbf{g}_i^H \otimes \mathbf{a}_i^H) \mathbf{P}_{\widehat{\mathbf{V}}_\Delta} (\mathbf{g}_i \otimes \mathbf{a}_i) = \mathbf{a}_i^H (\mathbf{g}_i^H \otimes \mathbf{I}_{N_v}) \mathbf{P}_{\widehat{\mathbf{V}}_\Delta} (\mathbf{g}_i \otimes \mathbf{I}_{N_v}) \mathbf{a}_i = \mathbf{a}_i^H \mathbf{F}(\tau_i) \mathbf{a}_i. \quad (6.27)$$

Hence, (6.23) can be simplified as

$$\min_{\mathbf{a}_i, \tau_i} \sum_{i=1}^{N_p} \mathbf{a}_i^H \mathbf{F}(\tau_i) \mathbf{a}_i, \quad \text{s.t. } \|\mathbf{a}_i\| = 1. \quad (6.28)$$

As we mentioned before, we assume that the  $\mathbf{a}_i$  is completely generic. Hence, (6.24) can be solved by the eigen-value and eigen-vector decomposition as

$$\mathbf{F}(\tau_i) \mathbf{V}_F = \mathbf{V}_F \Lambda_F, \quad (6.29)$$

$$\Lambda_F = \text{diag} \left( \left[ \lambda_1^F \quad \dots \quad \lambda_{N_v}^F \right] \right), \quad \mathbf{V}_F = \left[ \mathbf{v}_1^F \quad \dots \quad \mathbf{v}_{N_v}^F \right], \quad (6.30)$$

where the optimum vector for  $\mathbf{a}_i$  is given by the eigen-vector of  $\mathbf{F}(\tau_i)$  which corresponds to the lowest eigen-value as

$$\mathbf{a}_i^{opt} = \mathbf{v}_q^F, \quad q = \underset{1 < q < N_v}{\text{argmin}} \left[ \lambda_1^F \quad \dots \quad \lambda_{N_v}^F \right]. \quad (6.31)$$

Substituting  $\mathbf{a}_i^{opt}$  in (6.28), we can estimate all the values of  $\hat{\tau}_i$  performing one dimensional search as

$$\hat{\tau}_i = \min_{\tau_i} f(\mathbf{a}_i^{opt}, \tau_i) = \min_{\tau_i} f(\tau_i), \quad \forall i \in \{1, \dots, N_p\}. \quad (6.32)$$

Once we have obtained all values of  $\hat{\tau}_i$ , we can compute its corresponding vector  $\hat{\mathbf{a}}_i^{opt}$  and the matrix  $\hat{\mathbf{S}}$ .

In Fig. (6.3), we provide the algorithm description of our method. We can see that there is only one for-loop responsible for building the function  $f(\tau)$ , making it a low-complexity method. Under the absence of noise,  $f(\tau) \geq 0, \forall \tau$  only contains  $N_p$  zeros. However, under a realistic scenario,  $f(\tau)$  is quite sensitive to the noise effects, forcing us to compute its first derivative in order to obtain all  $\tau_i$  that corresponds to its local minimum points. Moreover, when the SNR is not high enough,  $f(\tau)$  may produce  $N'_p \neq N_p$  minimum points. In our algorithm, we assume that  $N_p$  is a known parameter and if  $N'_p > N_p$ , we will consider only  $N_p$  out  $N'_p$  with the lowest value of  $f(\tau_i), 1 < \tau_i < N'_p$ .

### 6.3.2 Iterative MLE method

In order to obtain the best performance of the estimated channel, we propose an iterative method based on MLE. The argument of (6.22) can be manipulated as

$$\text{tr} \left( \mathbf{P}_S^\perp \hat{\Sigma}_{\hat{h}} \right) = \text{tr} \left( \hat{\Sigma}_{\hat{h}} \right) - \text{tr} \left( \mathbf{P}_S \hat{\Sigma}_{\hat{h}} \right). \quad (6.33)$$

Hence, (6.22) can be transformed into

$$\max_{\mathbf{a}_i, \tau_i} \text{tr} \left( \mathbf{P}_S \hat{\Sigma}_{\hat{h}} \right), \quad \text{s.t.} \|\mathbf{a}_i\| = 1. \quad (6.34)$$

We propose an alternative way of defining  $\mathbf{P}_S$  as

$$\mathbf{P}_S = \mathbf{P}_{S_{\hat{i}}} + \mathbf{P}_{p_i}, \quad (6.35)$$



---

**Algorithm 1** MUSIC 1D algorithm
 

---

- 1: *Inputs:*
  - 2:  $\widehat{\boldsymbol{\Sigma}}_{\widehat{h}}$
  - 3: *Execution:*
  - 4: Compute  $\widehat{\mathbf{V}}_{\Delta}$  and  $\mathbf{P}_{\widehat{\mathbf{V}}_{\Delta}}$
  - 5: **for all**  $1 \leq j \leq \alpha N_t$  **do**
  - 6:      $\mathbf{g}(\tau_j) = [\mathbf{g}_{\alpha}(\tau - \tau_j)]_{\downarrow \alpha}$
  - 7:     Compute  $\mathbf{F}(\tau_j)$
  - 8:     Compute  $\mathbf{V}_F$  and  $\boldsymbol{\Lambda}_F$
  - 9:      $q = \underset{1 < q < N_v}{\operatorname{argmin}} [\lambda_1^F \ \cdots \ \lambda_{N_v}^F]$
  - 10:     Select the  $q$ -th eigen-vector out of  $\mathbf{V}_F$  as  $\mathbf{a}_j^{opt}$
  - 11:     Compute  $f(\tau_j)$
  - 12:      $\left. \frac{df(\tau)}{d\tau} \right|_{\tau_i} = 0 \rightarrow \tau_i, \quad 1 < i < N'_p$
  - 13: **if**  $N'_p > N_p$  **then**
  - 14:     Keep only  $N_p$   $\tau_i$  with lowest  $f(\tau_i)$
  - 15:      $N'_p = N_p$
  - 16: **for all**  $1 \leq i \leq N'_p$  **do**
  - 17:      $\mathbf{s}_i = \mathbf{g}_i \otimes \mathbf{a}_i$
  - 18: **return**  $\mathbf{S}$
- 

Figure 6.3: MUSIC 1D algorithm.

where  $\mathbf{S}_{\bar{i}}(N_h \times N_p - 1)$  is  $\mathbf{S}$  deleting its  $i$ -th column and  $\mathbf{P}_{p_i}$  denotes the matrix projector of  $\mathbf{p}_i(N_h \times 1) = \mathbf{P}_{\mathbf{S}_{\bar{i}}}^{\perp} \mathbf{s}_i$ .

This alternative way of defining  $\mathbf{P}_S$  is forcing us to sequentially compute each column of  $\widehat{\mathbf{S}}$  and at the same time canceling the effects of the other taps for each iteration. Hence, the argument of (6.34) for each iteration and the  $i$ -th column of  $\widehat{\mathbf{S}}$  is transformed into

$$\operatorname{tr} \left( \frac{\mathbf{P}_{\mathbf{S}_{\bar{i}}}^{\perp} \mathbf{s}_i \mathbf{s}_i^H \mathbf{P}_{\mathbf{S}_{\bar{i}}}^{\perp} \widehat{\boldsymbol{\Sigma}}_{\widehat{h}}}{\mathbf{s}_i^H \mathbf{P}_{\mathbf{S}_{\bar{i}}}^{\perp} \mathbf{s}_i} \right) = \frac{\mathbf{s}_i^H \mathbf{P}_{\mathbf{S}_{\bar{i}}}^{\perp} \widehat{\boldsymbol{\Sigma}}_{\widehat{h}} \mathbf{P}_{\mathbf{S}_{\bar{i}}}^{\perp} \mathbf{s}_i}{\mathbf{s}_i^H \mathbf{P}_{\mathbf{S}_{\bar{i}}}^{\perp} \mathbf{s}_i}. \quad (6.36)$$

Note that this method implies that we have to execute the minimization problem (6.36)  $N_p$  times for each iteration, and in each iteration we improve the estimation of  $\mathbf{S}$ . Hence, if we compare the complexity of this method with the previous one, the complexity is increased by  $N_p \times N_i$  times where  $N_i$  denotes the number of iterations.

Given (6.36), using again the definition of (6.13), we obtain that

$$\max_{\mathbf{a}_i, \tau_i} f_i(\mathbf{a}_i, \tau_i) \quad \text{s.t.} \quad \|\mathbf{a}_i\| = 1, \quad (6.37)$$

where

$$f_i(\mathbf{a}_i, \tau_i) = \frac{\mathbf{a}_i^H \mathbf{F}_i^n(\tau_i) \mathbf{a}_i}{\mathbf{a}_i^H \mathbf{F}_i^d(\tau_i) \mathbf{a}_i}, \quad (6.38)$$

$$\mathbf{F}_i^n(\tau_i) = (\mathbf{g}_i^H \otimes \mathbf{I}_{N_v}) \mathbf{P}_{\mathbf{S}_{\bar{i}}}^{\perp} \widehat{\boldsymbol{\Sigma}}_{\widehat{h}} \mathbf{P}_{\mathbf{S}_{\bar{i}}}^{\perp} (\mathbf{g}_i \otimes \mathbf{I}_{N_v}), \quad (6.39)$$

$$\mathbf{F}_i^d(\tau_i) = (\mathbf{g}_i^H \otimes \mathbf{I}_{N_v}) \mathbf{P}_{\mathbf{S}_{\bar{i}}}^{\perp} (\mathbf{g}_i \otimes \mathbf{I}_{N_v}), \quad (6.40)$$

Finally, we assume again that  $\mathbf{a}_i$  is generic, therefore, (6.36) can be solved by the generalized eigen-value and eigen-vector decomposition as

$$\mathbf{F}_i^n(\tau_i) \mathbf{V}_F = \mathbf{F}_i^d(\tau_i) \mathbf{V}_F \Lambda_F, \quad (6.41)$$

where the optimum vector for  $\mathbf{a}_i$  is given by the eigen-vector which corresponds to the highest eigen-value as

$$\mathbf{a}_i^{opt} = \mathbf{v}_q^F, \quad q = \underset{1 < q < N_v}{\operatorname{argmax}} \left[ \lambda_1^F \quad \dots \quad \lambda_{N_v}^F \right]. \quad (6.42)$$

Substituting  $\mathbf{a}_i^{opt}$  in (6.38), we can estimate only one  $\hat{\tau}_i$  searching in  $f_i(\tau_i)$ . Hence, the expression is given as

$$\hat{\tau}_i = \max_{\tau_i} f_i(\mathbf{a}_i^{opt}, \tau_i) = \max_{\tau_i} f_i(\tau_i). \quad (6.43)$$

The estimation of  $\{\hat{\mathbf{a}}_i, \hat{\tau}_i\} \forall 1 \leq i \leq N_p$  must be improved in the following iterations.

In Fig. (6.4), we provide the algorithm description of this method. We can see that there are two additional outer for-loops, as compared to MUSIC-1D, one for  $N_i$  and another for  $N_p$ , as we mentioned before. For this particular case, we set  $\mathbf{S}^{pre} = \mathbf{0}_{N_h \times N_p}$  at the beginning of the execution. Additionally, note that it is possible the use of any low-complexity software method to find the maximum value of  $f_i(\tau_j)$ , instead of using a derivative operation, due to the fact that we are searching a unique global maximum for each tap and iteration.

Moreover, we also propose an accelerated method of searching for the single global maximum of  $f_i(\tau_j)$  in the iterative MLE method, described in Alg. (6.5). Instead of computing  $f_i(\tau_j)$  in  $\alpha N_t$  different values for each tap and iteration, we propose to evaluate it in only a subset of  $\alpha N_t$  in several iterations, taking advantage of the fact that it is a band-limited function. This is mainly due to the fact that the shape of transmitter and receiver pulses are also band-limited ones. As we see in Fig. (6.5), we have  $N_\beta$  decimation factors  $> 1$ , except the last one, which is 1. In the first iteration, we are only evaluating  $f_i(\tau_j)$  in  $\alpha N_t / \beta_1$  equally spaced points of  $\tau_j$ . We obtain  $j_1^{opt}$  which is the index that corresponds to the maximum value of  $f_i(\tau_j)$  in the first iteration. In the following iterations, we only evaluate  $f_i(\tau_j)$  in the neighbor points of  $j_1^{opt}$  up to reaching  $\beta_{N_\beta} = 1$ , which retrieves the  $\tau_j^{opt}$ . Therefore, the number of execution in our accelerated method  $N_e^a$  is given by

$$N_e^a = \sum_{i=1}^{N_\beta} N_{e,i}^a = \frac{\alpha N_t}{\beta_1} + 3 \frac{\beta_1 - 1}{\beta_2} + 3 \frac{\beta_2 - 1}{\beta_3} + \dots = \frac{\alpha N_t}{\beta_1} + 3 \sum_{i=2}^{N_\beta} \frac{\beta_{i-1} - 1}{\beta_i} \ll \alpha N_t. \quad (6.44)$$

### 6.3.3 Hybrid method

The two previous methods have their own strengths and weaknesses. MUSIC-1D is a low-complexity method which only has a great performance in high SNRs. Iterative MLE provides

**Algorithm 2** Iterative ML algorithm

---

```

1: Inputs:
2:  $\widehat{\mathbf{S}}_h$ 
3:  $\mathbf{S}^{pre}$  ( $N_h \times N'_p$ ) denotes the pre-computed  $\mathbf{S}$ 
4:  $N_i > 0$  denotes the number of iterations
5: Initialization:
6:  $\mathbf{S} = [\mathbf{S}^{pre} \quad \mathbf{0}_{N_h \times N_p - N'_p}]$ 
7: Execution:
8: for all  $1 \leq k \leq N_i$  do
9:   Computing the  $\mathbf{s}_i^k$ :
10:  for all  $1 \leq i \leq N_p$  do
11:     $\mathbf{P}_{S_i}$  at the first iteration:
12:    if  $k == 1$  then
13:      if  $i > N'_p$  then
14:        if  $i == 1$  then
15:           $\mathbf{P}_{S_i} = \mathbf{0}_{N_h \times N_h}$ 
16:        else
17:           $\mathbf{S}_i = [\mathbf{s}_1^k \quad \cdots \quad \mathbf{s}_{i-1}^k]$ 
18:          Compute  $\mathbf{P}_{S_i}$ 
19:     $\mathbf{P}_{S_i}$  at the following iterations:
20:    else
21:       $\mathbf{S}_i = [\mathbf{s}_1^k \quad \cdots \quad \mathbf{s}_{i-1}^k \quad \mathbf{s}_{i+1}^{k-1} \quad \cdots \quad \mathbf{s}_{N_p}^{k-1}]$ 
22:      Compute  $\mathbf{P}_{S_i}$ 
23:    Computation of orthogonal projector:
24:    Compute  $\mathbf{P}_{S_i}^\perp = \mathbf{I}_{N_h} - \mathbf{P}_{S_i}$ 
25:    Compute  $\mathbf{P}_{S_i}^\perp \widehat{\mathbf{S}}_h \mathbf{P}_{S_i}^\perp$ 
26:    Seeking the best  $\tau_j$ :
27:    for all  $1 \leq j \leq \alpha N_t$  do
28:       $\mathbf{g}(\tau_j) = [\mathbf{g}_\alpha(\tau - \tau_j)]_{\downarrow \alpha}$ 
29:      Compute  $\mathbf{F}_i^n(\tau_j)$  and  $\mathbf{F}_i^d(\tau_j)$ 
30:      Compute  $\mathbf{V}_F$  and  $\mathbf{\Lambda}_F$ 
31:       $q = \operatorname{argmax}_{1 < q < N_v} [\lambda_1^F \quad \cdots \quad \lambda_{N_v}^F]$ 
32:      Select the  $q$ -th eigen-vector out of  $\mathbf{V}_F$  as  $\mathbf{a}_j^{opt}$ 
33:      Compute  $f_i(\mathbf{a}_j^{opt}, \tau_j) = f_i(\tau_j)$ 
34:      Search  $\tau_j^{opt} = \operatorname{argmax}_{\tau_j} f_i(\tau_j)$ 
35:    Storage the  $\mathbf{s}_i^k$ :
36:     $\tau_i \leftarrow \tau_j^{opt}$ 
37:     $\mathbf{s}_i^k = \mathbf{g}_i \otimes \mathbf{a}_i$ 
38: return  $\mathbf{S}$ 

```

---

Figure 6.4: Iterative MLE algorithm.

a great performance in any scenario with a considerable complexity. Therefore, we propose the hybrid one which consists in the combination of both of them in order to trade-off performance and complexity.

Firstly, we use the MUSIC-1D method in order to compute a preliminary  $\widehat{\mathbf{S}}$ . Then, we use the iteration MLE method in order to improve the estimation, setting  $\mathbf{S}^{pre}$  as the output of MUSIC-1D. Note that, as we mentioned before,  $\widehat{\mathbf{S}}$  provided by MUSIC-1D method may have  $N'_p \neq N_p$  columns. If  $N'_p > N_p$  we keep only the best  $N_p$  ones which correspond to the lowest values of  $f(\widehat{\tau}_i)$ . However, if  $N'_p < N_p$ , the iterative MLE method will compute first the missing columns, and then,

---

**Algorithm 3** Accelerated search
 

---

```

1: Inputs:
2: Initialization:
3:  $\beta_i > 1$ ,  $1 \leq i \leq N_\beta - 1$  denotes decimation factor
4:  $\beta_{N_\beta} = 1$ 
5: Execution:
6:  $j_{ini} = 1$ ,  $j_{mid} = \infty$ ,  $j_{end} = \alpha N_t$ ,  $j_{stp} = \beta_1$ 
7: Seeking the best  $\tau_j$ :
8: for all  $1 \leq i \leq N_\beta$  do
9:   for all  $j \in \{j_{ini} : j_{stp} : j_{end}\}$  do
10:    if  $j \neq j_{mid}$  then
11:      Compute  $f_i(\tau_j)$ 
12:    Search  $j_i^{opt} \leftarrow \tau_j^{opt} = \underset{\tau_j}{\operatorname{argmax}} f_i(\tau_j)$ 
13:    if  $i \neq N_\beta$  then
14:       $j_{ini} = j_i^{opt} - 1$ ,  $j_{end} = j_i^{opt} + 1$ 
15:       $j_{mid} = j_i^{opt}$ ,  $j_{stp} = \beta_{i+1}$ 
16: Storage the  $\mathbf{s}_i^k$ :
17:  $\tau_i \leftarrow \tau_j^{opt}$ 
18:  $\mathbf{s}_i^k = \mathbf{g}_i \otimes \mathbf{a}_i$ 
19: return  $\mathbf{S}$ 
    
```

---

Figure 6.5: Accelerated search algorithm.

it will improve the estimation in the following iterations. As we can see later in the numerical results, only one additional iteration of MLE is needed in order to achieve the convergence of  $\widehat{\mathbf{S}}$ .

## 6.4 Automatic-rank selector (ARS)

Once we have  $\widehat{\mathbf{S}}$ , we propose an ARS algorithm based on the selection of the best columns of  $\widehat{\mathbf{S}}$  in order to minimize the MSE. Note that the number of selected columns (rank) is denoted by  $N_k$ , where  $1 \leq N_k < N_p$ . Therefore, (6.12) can be decomposed as

$$\mathbf{h}(l) = \mathbf{S}\mathbf{d}(l) = \begin{bmatrix} \mathbf{S}_k & \mathbf{S}_{\bar{k}} \end{bmatrix} \begin{bmatrix} \mathbf{d}_k(l) \\ \mathbf{d}_{\bar{k}}(l) \end{bmatrix}, \quad (6.45)$$

where  $\mathbf{S}_k(N_h \times N_k)$  and  $\mathbf{d}_k(l)(N_k \times 1)$  denote the LR version of  $\mathbf{S}$  and  $\mathbf{d}(l)$ , respectively; and  $\mathbf{S}_{\bar{k}}(N_h \times N_p - N_k)$  and  $\mathbf{d}_{\bar{k}}(l)(N_p - N_k \times 1)$  are the complementary ones. Note that, the  $N_k$  columns of  $\mathbf{S}_k$  correspond with the strongest coefficients of  $\boldsymbol{\Sigma}_d$  (see (6.5)).

In order to reduce the complexity of the algorithm, we analyze the MSE to obtain some insight on the best rank to use. For the ease of the analysis, we assume that  $\widehat{\mathbf{S}} = \mathbf{S}$ . Hence, the MSE of the FR projected version of the estimated channel is given by

$$\sigma_{S\Delta h}^2 = \mathbb{E} \left\{ \left\| \mathbf{P}_S \widehat{\mathbf{h}} - \mathbf{h} \right\|_F^2 \right\} = \mathbb{E} \left\{ \left\| \mathbf{P}_S \Delta \mathbf{h} \right\|_F^2 \right\} = \frac{N_p}{N_h} \sigma_{\Delta h}^2, \quad (6.46)$$

and the MSE of the LR projected version can be expressed as

$$\sigma_{S_k \Delta h}^2 = \mathbb{E} \left\{ \left\| \mathbf{P}_{S_k} \hat{\mathbf{h}} - \mathbf{h} \right\|_F^2 \right\}, \quad (6.47)$$

where its argument can be derived as

$$\begin{aligned} \mathbf{P}_{S_k} \hat{\mathbf{h}} - \mathbf{h} &= -(\mathbf{S}_k \mathbf{d}_k(l) + \mathbf{S}_{\bar{k}} \mathbf{d}_{\bar{k}}(l)) + (\mathbf{S}_k \mathbf{d}_k(l) + \mathbf{P}_{S_k} \mathbf{S}_{\bar{k}} \mathbf{d}_{\bar{k}}(l) + \mathbf{P}_{S_k} \Delta \mathbf{h}) = \\ &= -\mathbf{P}_{S_k}^\perp \mathbf{S}_{\bar{k}} \mathbf{d}_{\bar{k}}(l) + \mathbf{P}_{S_k} \Delta \mathbf{h}. \end{aligned} \quad (6.48)$$

Assuming that the channel estimation error (noise) is independent of the channel itself, (6.47) can be derived as

$$\sigma_{S_k \Delta h}^2 = \mathbb{E} \left\{ \left\| \mathbf{P}_{S_k}^\perp \mathbf{S}_{\bar{k}} \mathbf{d}_{\bar{k}}(l) \right\|_F^2 \right\} + \frac{N_k}{N_h} \sigma_{\Delta h}^2 = \mathbb{E} \{ f_{\text{bias}}(N_k, l) \} + \frac{N_k}{N_h} \sigma_{\Delta h}^2. \quad (6.49)$$

Inspecting (6.49), its second term can be easily computed given the SNR. However, the first term involves an expectation operator and it will cause a negative impact in the system in terms of latency. Therefore, we propose to use directly  $f_{\text{bias}}(N_k, l)$  for each iteration and each rank, instead of computing its expected value, as described in Fig. (6.6).

---

**Algorithm 4** ARS
 

---

```

1: Inputs:
2:  $\hat{\mathbf{h}}, \mathbf{S}$  and  $\sigma_{\Delta h}^2$ 
3: Execution:
4: Estimation of the PDP:
5: for all  $1 \leq l \leq N_l$  do
6:   Compute  $\hat{\mathbf{d}}(l) = [\hat{d}_1(l) \ \cdots \ \hat{d}_{N_p}(l)]^T$ 
7:   Averaging  $\|\hat{\mathbf{d}}\|_F^2 = \|\hat{\mathbf{d}}\|_F^2 + \frac{1}{N_l} \|\hat{\mathbf{d}}(l)\|_F^2$ 
8: Sort  $\|\hat{\mathbf{d}}\|_F^2$  in descend mode  $\rightarrow$  indices  $\mathbf{u}$ 
9: Sort the columns of  $\mathbf{S}$  using indices  $\mathbf{u} \rightarrow \mathbf{S}^{sort}$ 
10: ARS:
11: for all  $1 \leq l \leq N_l$  do
12:   Sort the values of  $\hat{\mathbf{d}}(l)$  using indices  $\mathbf{u}_l \rightarrow \hat{\mathbf{d}}^{sort}(l)$ 
13:   for all  $1 \leq i \leq N_p$  do
14:     if  $i == N_p$  then
15:        $e_i = \frac{i}{N_r} \sigma_{\Delta h}^2$ 
16:     else
17:        $\mathbf{S}_i \leftarrow$  first  $i$  columns of  $\mathbf{S}^{sort}$ 
18:       Compute  $\mathbf{P}_{S_k}$  and  $\mathbf{P}_{S_k}^\perp$ 
19:        $\mathbf{S}_{\bar{i}} \leftarrow$  last  $N_p - i$  columns of  $\mathbf{S}^{sort}$ 
20:        $\mathbf{d}_{\bar{i}}(l) \leftarrow$  last  $N_p - i$  values of  $\hat{\mathbf{d}}^{sort}(l)$ 
21:       Compute  $f_{bias}$ 
22:        $e_i = f_{bias} + \frac{i}{N_h} \sigma_{\Delta h}^2$ 
23:    $k_l = \underset{1 < k_l < N_p}{\operatorname{argmin}} [e_1 \ \cdots \ e_{N_p}]$ 
24:   Select  $\mathbf{S}_{k_l}(l)$ 
25: return  $\mathbf{S}_{k_l} \ \forall 1 < l < N_l$ 
    
```

---

Figure 6.6: ARS algorithm.

## 6.5 Numerical results

In this section, we show several simulation results in order to provide a better understanding the performance of our proposals.

### 6.5.1 Simulation parameters

In Table 6.1 we provide the numerical values to our defined parameters. The selected multi-path channel model is given in Table 6.2. The SNR is defined as  $\text{SNR} = \mathbb{E} \left\{ \|\mathbf{H}(l)\|_F^2 \right\} / (N_v \sigma_n^2)$ .

According to [54], the antenna array response is given by

$$[\mathbf{a}(\theta_i)]_v = a_d(\theta_i, v) a_m(\theta_i, v), \quad 1 \leq i \leq N_p, \quad 1 \leq v \leq N_v, \quad (6.50)$$

where  $a_d(\theta_i, v)$  and  $a_m(\theta_i, v)$  are the directivity and the array manifold, respectively. We assume that the structure of the antenna array at the BS is circular, hence, the directivity and manifold

Table 6.1: Simulation parameters for LR channel estimation.

$N_r$	10 antennas	$\alpha \Delta f$	$10 \times 60\text{KHz}$
$N_l$	20 slots	<b>Constellation</b>	QPSK
$N_s$	100 symbols	$\beta_1$	10
$N_p$	5 taps	$\beta_2$	2
<b>Tx-Rx pulse shape</b>		Raised cosine filter roll-off 0.25	

Table 6.2: PDP

$i$	1	2	3	4	5
$\sigma_i^2[\text{dB}]$	-1	0	-3	-5	-7
$\tau_i[\text{ms}]$	0	0.5	1.7	2.4	5

are detailed as

$$a_d(\theta, v) = 1.8 \cos^{1.6} \left( \theta - \frac{2\pi}{N_v} (v-1) \right), \quad (6.51)$$

$$a_m(\theta, v) = \exp \left( j \frac{d_r N_r}{\lambda} \left( 1 - \cos \left( \theta - \frac{2\pi}{N_v} (v-1) \right) \right) \right), \quad (6.52)$$

where  $\lambda$  denotes the wavelength and  $d_r = \lambda/2$  is the distance between two contiguous elements. The carrier frequency is  $f_c = 28\text{GHz}$  and DoA is modeled as  $\theta \sim U[-\pi/3, \pi/3]$ .

## 6.5.2 Results and discussion

In Fig. 6.7, we plot the channel estimation error  $\sigma_{\Delta h}^2$  and the idealistic FR channel estimation error  $\sigma_{S\Delta h}^2$  ( $\hat{\mathbf{S}} = \mathbf{S}$ ) as reference and the MSE performance of the algorithm MUSIC-1D. We can see that the projected version of the estimated channel using the theoretical  $\mathbf{S}$  significantly outperforms the non-projected one thanks to the subspace method. Moreover, regarding the MUSIC-1D performance, it clearly shows that the performance at low SNR regimes is compromised, obliging us to find other alternatives.

In Fig. 6.8, we show the performance of the iterative MLE algorithm. We can see that this method can achieve a very good performance at the expense of iterating up to four times. Additionally, we can see that there is a small gap error between the fourth iteration of MLE and the  $\sigma_{S\Delta h}^2$ , which is due to the estimation error in  $\hat{\mathbf{S}}$ .

In Fig. 6.9, we provide the performance of the hybrid solution. It shows that the first iteration is better than the regular MUSIC-1D we mentioned before, MUSIC-1D may provide  $N'_p \neq N_p$  and, when  $N'_p < N_p$  the iterative MLE may compute the missing columns of  $\hat{\mathbf{S}}$ . Furthermore, the

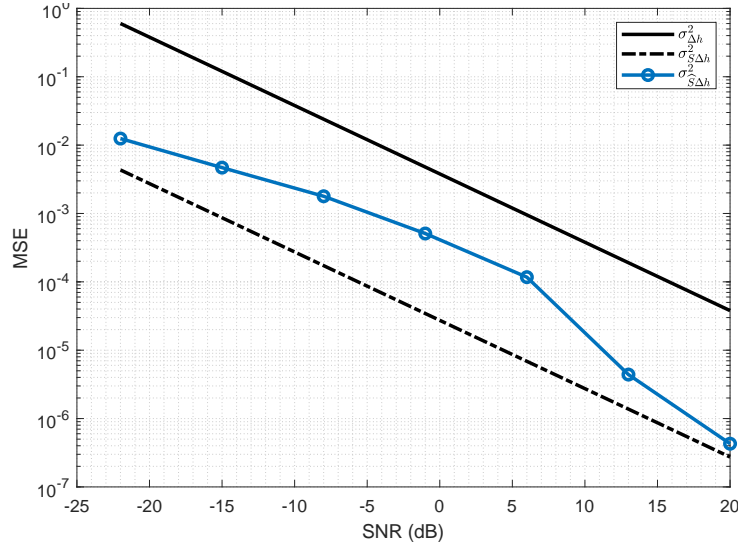


Figure 6.7: MSE of MUSIC-1D algorithm.

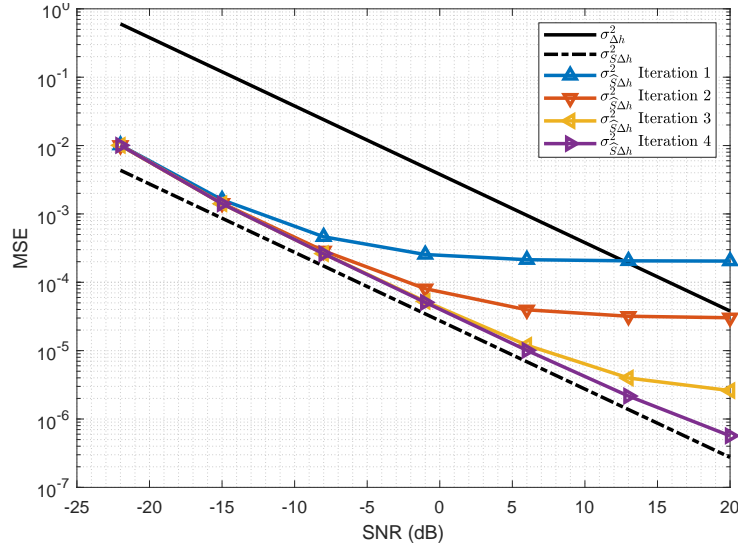


Figure 6.8: MSE of iterative MLE algorithm.

hybrid method only requires an additional iteration in order to saturate the performance, showing the superiority of this method which is capable of trading-off the performance and complexity.

For the hybrid method with two iterations, in Fig. 6.10, we show the performance comparison of FR and LR estimated channels between using  $\mathbf{S}$  (idealistic case), as a benchmark and  $\widehat{\mathbf{S}}$  (realistic case). In extreme low SNR scenarios, as expected, the performance of the realistic case is worse than the idealistic one due to the presence of strong noise in the estimation of  $\widehat{\Sigma}_{\widehat{h}}$ . Note that, when the SNR is moderate, there is a gap in the FR case due to the estimation error in  $\mathbf{S}$  caused by the noise; and for the LR scenarios, the gap is negligible due to the fact that the approximation



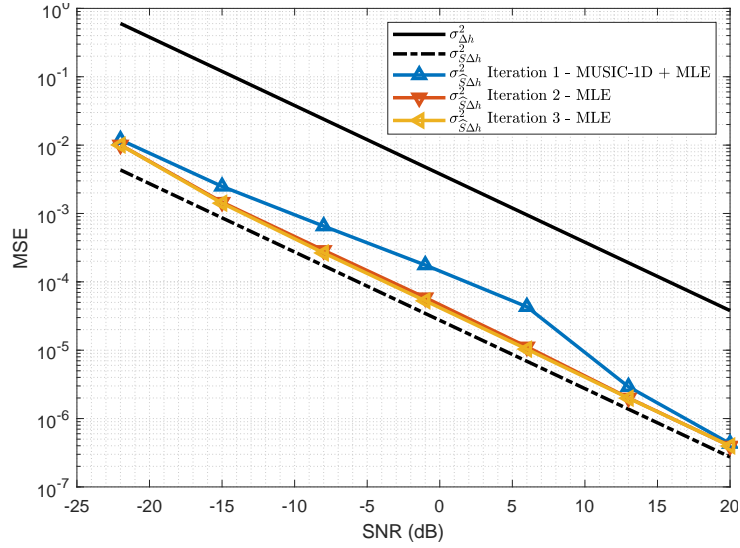
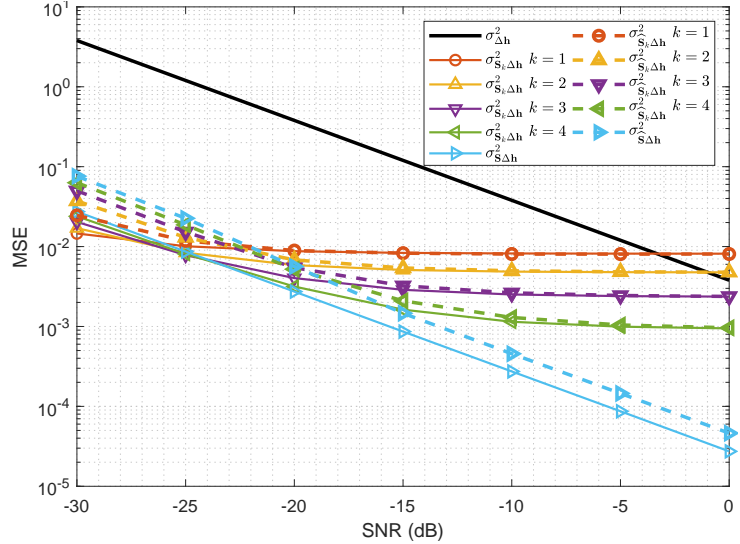


Figure 6.9: MSE of hybrid algorithm.

error is much bigger than the noise effects. This means that LR approximation is not affected by the noise when the SIR is moderate or high.


 Figure 6.10: Comparison of the MSE among FR and LR estimated channel using  $\mathbf{S}$  and  $\hat{\mathbf{S}}$ .

In Fig. 6.11, we plot a performance comparison of our proposed scheme against the proposed in [54]. Note that in order to implement [54] and make a fair comparison, we have considered the absence of any interference source, so we have removed its whitening part. We can see that our proposed scheme significantly outperforms [54] in extremely low SNR scenarios and for moderate SNR, our FR also outperforms the referenced one.

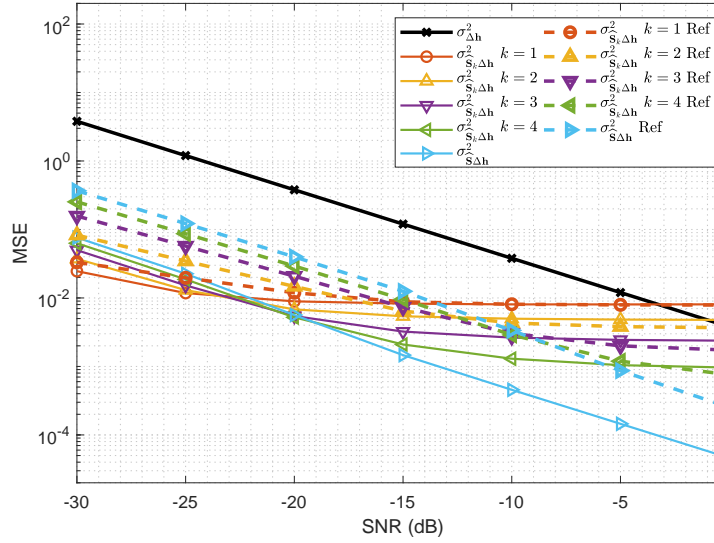


Figure 6.11: Comparison of the MSE between our proposal and the reference.

In Fig. 6.12, we show the validity of (6.49), when perfect  $\mathbf{S}$  is considered. We can see that all theoretical curves (dashed line) match perfectly to the simulated ones (solid lines). Note that, the minimum gap between them is due to the fact that for the theoretical case, we assume that  $\text{tr}(\mathbf{R}_{xx}^{-1}) = 1$ , where it does not hold for a realistic scenario.

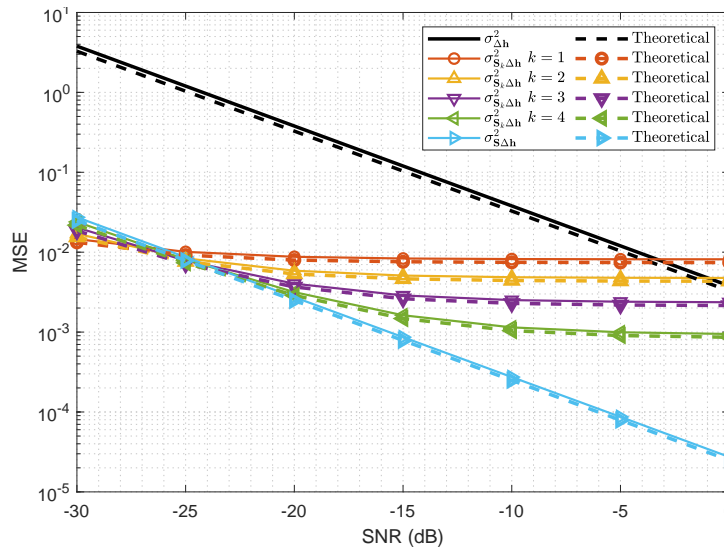


Figure 6.12: Comparison of the MSE among simulation and theoretical analysis results for FR and LR assuming perfect  $\mathbf{S}$ .

Finally, we provide the performance of the ARS algorithm. We can see that using the instantaneous error  $f_{\text{bias}}(N_k, l)$ , that involves the error estimation in  $\hat{\mathbf{d}}_k(l)$ , is good enough to select always the best LR estimated channel.

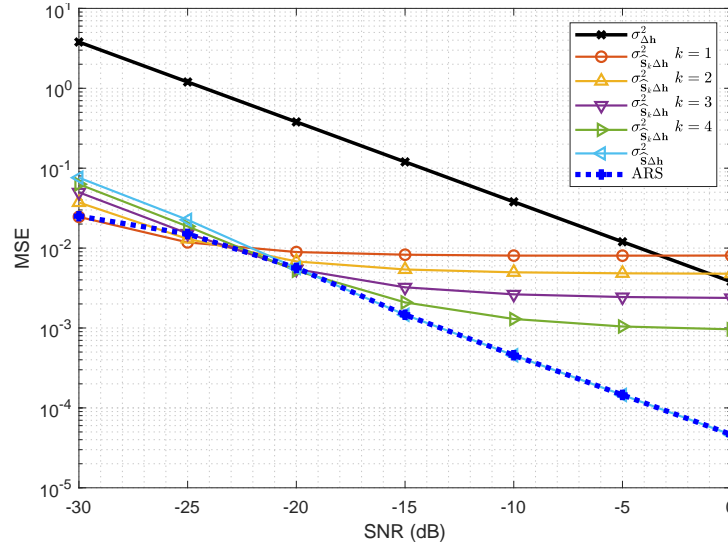


Figure 6.13: MSE of the ARS algorithm.

## 6.6 Conclusions

In the present chapter we have proposed a novel method to perform the channel estimation in massive multiple antenna scenarios. Our method is based on the estimation of a joint ST covariance matrix; and then, applying a subspace method to obtain the DoA and ToA of each tap using an effective searching method. We have shown that our proposal outperforms the existing techniques, either FR and LR ones and we also provided a novel ARS which is capable of selecting the best LR channel for each scenario providing the lowest MSE. Thus, the proposed schemes are suitable for the dynamic SNR environment often found in mmWave.



# Chapter 7

## Conclusions

### 7.1 Conclusions

In this thesis, we focused on providing some new channel estimation techniques for the different key technologies for the next generation of mobile communications, such as: FBMC-OQAM, massive MIMO-OFDM and mmWave. For all of them, our novel proposed techniques outperform the existing ones and, as far as possible, decrease the overall complexity.

Firstly, we proposed new pilot sequences for FBMC-OQAM, namely CPB and BPS. CPB provides a robust channel tracking, suitable for fast-varying or strong fading channels. BPS is capable of adapting its length according to the variability of the channel, increasing the overall efficiency. Both, techniques allow a estimation process by using an averaging operation, which is simple and effective to obtain the estimators. According to our analysis, our technique is not only better than the existing ones, such as AP; but also significantly reduces the complexity.

Later, we provided a practical framework for the channel estimation and equalization process for massive MIMO-OFDM. When the number of antennas is large, it is possible to compute first the precoding/postcoding matrices at the pilot positions. Then, these matrices are interpolated over time-frequency resources using a simple linear interpolation. Furthermore, this technique can be combined with the use of NS to approximate the matrix inverse needed for the ZF criterion. We have shown that the gap between using the proposed technique and the traditional one is negligible when the number of antennas is considerably high.

Finally, we introduced a new FR and LR channel estimation technique for massive MIMO in mmWave. This technique is based on the estimation of a joint ST covariance matrix and using the subspace method to reduce the noise effect. The computation of an accurate projector for the

subspace method relies on a hybrid technique, which is designed to trade-off between performance and complexity of the system. Furthermore, we also provided a ARS which is capable of choosing the best LR channel estimator depending on the quality of the link.

Given all these proposals, we have contributed to the implementation of 5G paving the way towards satisfying the three main requirements: eMBB, massive MTC and URLLC. eMBB can be achieved with the operation of mmWaves that provide hundreds of megahertz of bandwidth, which is only possible with the use of MIMO techniques. Massive MTC and URLLC can be only deployed by using low-complexity channel estimation and equalization techniques, which can reduce either the delay of the computations and the battery consumption. Thus, we contribute to fulfilling the demands of the society by providing novel signal processing techniques for 5G.

## 7.2 Future work

In order to successfully deploy either 5G or beyond 5G networks, many new techniques must be taken into account in order to satisfy all the demands and provide new experiences to the society. Following the topic of these thesis, we provide some future work related to the field of channel estimation techniques.

We proposed some novel pilot sequences and estimation technique for FBMC-OQAM under a single-user SISO scenario. A straightforward research line consists in the expansion of this topic to multi-user MIMO case, where new orthogonal sequences must be designed in order to efficiently deal with self-interference of FMBC-OQAM in a multi-user scenario. Later, it should also be explored the case of massive MIMO, as we did for OFDM.

We showed that channel estimation and equalization processes for very large MIMO can be approximated by low-complexity techniques, which also achieve a good performance. However, the channel propagation profile used in our proposal is uncorrelated among the antennas at the BS and the carrier frequency is below 6GHz. An interesting research consists of analyzing how to reduce the number of operations for channel estimation and equalization processes using mm-Wave channel models combined with the effects of the array response, under different SNR scenarios.

We provided a new FR and LR channel estimation technique for mmWave combined with a massive number of antennas at the BS. Firstly, in order to work in a more realistic scenario, we should consider the pilot-contamination or any other source of interference, where the covariance matrix is no longer a diagonal one. Thus, we must propose some additional processing techniques such as a whitening transformation. Additionally, we assumed a single-user case using a single-carrier waveform. It would be interesting to explore the extension of our technique to the multi-user case combined with some multi-carrier waveform, such as OFDM and FBMC-OQAM. Finally, we

have only provided the performance of the FR and LR channel estimation in terms of MSE. Hence, it is very important to find out a low-complexity technique to compute the precoding/postcoding matrices for the LR case and obtain some results based on SER, due to the fact that under some environments, no matter how better is the MSE of the estimated channel, the SER does not show a great improvement.





# Bibliography

- [1] 3GPP. Evolved universal terrestrial radio access (E-UTRA), physical channels and modulation, 2016. 1, 2, 4, 8, 18, 19
- [2] 3GPP. Evolved universal terrestrial radio access (E-UTRA), physical channels and modulation, 2019. 1, 2, 3, 4, 8
- [3] TVS. 5G usage scenarios in non-standalone (NSA) and standalone (SA) operation. <https://www.testandverification.com/telecommunications/5g-usage-scenarios-nsa-sa/>, 2019. 1
- [4] T. Hwang, C. Yang, G. Wu, S. Li, and G. Y. Li. OFDM and its wireless applications: A survey. *IEEE Transactions on Vehicular Technology*, 58(4):1673–1694, May. 2009. 2, 8
- [5] S. Yang and L. Hanzo. Fifty years of MIMO detection: The road to large-scale MIMOs. *IEEE Communications Surveys Tutorials*, 17(4):1941–1988, Fourthquarter 2015. 3, 13
- [6] L. Lu, G. Y. Li, A. L. Swindlehurst, A. Ashikhmin, and R. Zhang. An overview of Massive MIMO: Benefits and challenges. *IEEE Journal of Selected Topics in Signal Processing*, 8(5):742–758, Oct 2014. 3, 13
- [7] 3GPP. Evolved universal terrestrial radio access (E-UTRA), base station (BS) radio transmission and reception, 2019. 3, 27
- [8] CableFree. 5G frequency bands: Spectrum allocations for next-gen LTE. <https://www.cablefree.net/wirelesstechnology/4glte/5g-frequency-bands-lte/>, 2019. 3
- [9] B. Yang, Z. Yu, J. Lan, R. Zhang, J. Zhou, and W. Hong. Digital beamforming-based massive MIMO transceiver for 5G millimeter-wave communications. *IEEE Transactions on Microwave Theory and Techniques*, 66(7):3403–3418, July 2018. 4, 29
- [10] K. C. Hu and A. G. Armada. SINR analysis of OFDM and f-OFDM for machine type communications. In *2016 IEEE 27th Annual International Symposium on Personal, Indoor, and Mobile Radio Communications (PIMRC)*, pages 1–6, Sep. 2016. 4, 9

- [11] K. Chen-Hu, R. P. Leal, and A. G. Armada. Reducing the interference by adapting the power of OFDM for mMTC. In *2018 IEEE 87th Vehicular Technology Conference (VTC Spring)*, pages 1–5, June 2018. 4, 12
- [12] K. Chen-Hu, F. Kaltenberger, and A. Garcia Armada. Implementation and measurement of power adapted-OFDM using openairinterface. In *2018 IEEE 19th International Workshop on Signal Processing Advances in Wireless Communications (SPAWC)*, pages 1–5, June 2018. 4, 12
- [13] K. Chen-Hu, J. C. Estrada-Jiménez, M. J. F. García, and A. G. Armada. Continuous and burst pilot sequences for channel estimation in FBMC-OQAM. *IEEE Transactions on Vehicular Technology*, 67(10):9711–9720, Oct 2018. 4
- [14] K. Chen-Hu and A. Garcia Armada. Low-complexity computation of zero-forcing equalizers for massive MIMO-OFDM. In *2019 IEEE 89th Vehicular Technology Conference (VTC-Spring)*, Apr. 2019. 5
- [15] K. Chen-Hu, D. T. M. Slock, and A. G. Armada. Low-rank channel estimation for mm-wave multiple antenna systems using joint spatio-temporal covariance matrix. *2019 IEEE International Conference on Communications Workshops (ICC Workshops): Workshop on Millimeter-Wave Communications for 5G and B5G, Shanghai*, pages 1–6, May 2019. 5
- [16] K. Chen-Hu, J. C. Estrada-Jimenez, M. J. F. Garcia, and A. G. Armada. Superimposed training for channel estimation in FBMC-OQAM. In *2017 IEEE 86th Vehicular Technology Conference (VTC-Fall)*, pages 1–5, Sep. 2017. 5, 23
- [17] J. C. Estrada-Jiménez, K. Chen-Hu, M. J. F. García, and A. G. Armada. Power allocation and capacity analysis for FBMC-OQAM with superimposed training. *IEEE Access*, 7:46968–46976, 2019. 5, 24
- [18] K. Chen-Hu and A. G. Armada. Non-coherent multiuser massive MIMO-OFDM with differential modulation. In *2019 IEEE International Conference on Communications (ICC), Shanghai*, pages 1–6, May. 2019. 5, 24
- [19] Wikipedia. 5G. <https://en.wikipedia.org/wiki/5G>, 2019. 7
- [20] ETSI. Digital video broadcasting (DVB); framing structure, channel coding and modulation for digital terrestrial television, 2008. 8, 29
- [21] IEEE. IEEE standard for local and metropolitan area networks, part 16: Air interface for broadband wireless access systems, 2005. 8, 29

- 
- [22] IEEE. Ieee standard for local and metropolitan area networks, part 11: Wireless LAN medium access control (MAC) and physical layer (PHY), 2018. 8
- [23] 3GPP. Evolved universal terrestrial radio access (E-UTRA), base station (BS) radio transmission and reception, 2016. 8, 27, 40, 53
- [24] P. Siohan, C. Siclet, and N. Lacaille. Analysis and design of OFDM/OQAM systems based on filterbank theory. *IEEE Transactions on Signal Processing*, 50(5):1170–1183, May 2002. 8
- [25] X. Zhang, M. Jia, L. Chen, J. Ma, and J. Qiu. Filtered-OFDM - enabler for flexible waveform in the 5th generation cellular networks. In *2015 IEEE Global Communications Conference (GLOBECOM)*, pages 1–6, Dec 2015. 8, 9
- [26] X. Wang, T. Wild, F. Schaich, and A. Fonseca dos Santos. Universal filtered multi-carrier with leakage-based filter optimization. In *European Wireless 2014; 20th European Wireless Conference*, pages 1–5, May 2014. 8, 9
- [27] A. Farhang, N. Marchetti, and L. E. Doyle. Low-complexity modem design for GFDM. *IEEE Transactions on Signal Processing*, 64(6):1507–1518, March 2016. 8, 11
- [28] L. Zhang, P. Xiao, A. Zafar, A. u. Quddus, and R. Tafazolli. FBMC system: An insight into doubly dispersive channel impact. *IEEE Transactions on Vehicular Technology*, 66(5):3942–3956, May. 2017. 9, 33
- [29] Antonia M. Tulino and Sergio Verdú. Random matrix theory and wireless communications. *Foundations and Trends in Communications and Information Theory*, 1(1):1–182, 2004. 13, 51
- [30] M. Giordani, M. Mezzavilla, and M. Zorzi. Initial access in 5G mmWave cellular networks. *IEEE Communications Magazine*, 54(11):40–47, November 2016. 14
- [31] Sheri De Tomasi. Fact or fiction: What’s real in 5G new radio. <https://www.ecnmag.com/article/2018/05/fact-or-fiction-whats-real-5g-new-radio>, 2019. 14
- [32] A. F. Molisch, V. V. Ratnam, S. Han, Z. Li, S. L. H. Nguyen, L. Li, and K. Haneda. Hybrid beamforming for massive MIMO: A survey. *IEEE Communications Magazine*, 55(9):134–141, Sep. 2017. 14
- [33] R. Nilsson, O. Edfors, M. Sandell, and P. O. Borjesson. An analysis of two-dimensional pilot-symbol assisted modulation for OFDM. In *1997 IEEE International Conference on Personal Wireless Communications (Cat. No.97TH8338)*, pages 71–74, Dec 1997. 18

- [34] Theodore S. Rappaport. *Wireless Communications: Principles and Practice, Second Edition*. Prentice Hall, 2002. 18, 26, 35, 41
- [35] O. Elijah, C. Y. Leow, T. A. Rahman, S. Nunoo, and S. Z. Iliya. A comprehensive survey of pilot contamination in massive MIMO-5G system. *IEEE Communications Surveys Tutorials*, 18(2):905–923, Secondquarter 2016. 19
- [36] J. Flordelis, F. Rusek, F. Tufvesson, E. G. Larsson, and O. Edfors. Massive mimo performance, TDD versus FDD: What do measurements say? *IEEE Transactions on Wireless Communications*, 17(4):2247–2261, April 2018. 20
- [37] M. Borgmann and H. Bolcskei. Interpolation-based efficient matrix inversion for MIMO-OFDM receivers. In *Conference Record of the Thirty-Eighth Asilomar Conference on Signals, Systems and Computers, 2004.*, volume 2, pages 1941–1947 Vol.2, Nov 2004. 21, 49
- [38] C. Zhang, Y. Jing, Y. Huang, and L. Yang. Performance analysis for massive MIMO downlink with low complexity approximate zero-forcing precoding. *IEEE Transactions on Communications*, pages 1–1, 2018. 21, 50, 52
- [39] T. Xie, L. Dai, X. Gao, X. Dai, and Y. Zhao. Low-complexity ssor-based precoding for massive MIMO systems. *IEEE Communications Letters*, 20(4):744–747, April 2016. 21
- [40] L. Dai, X. Gao, X. Su, S. Han, C. L. I, and Z. Wang. Low-complexity soft-output signal detection based on gauss-seidel method for uplink multiuser large-scale MIMO systems. *IEEE Transactions on Vehicular Technology*, 64(10):4839–4845, Oct 2015. 21
- [41] E. Kofidis and D. Katselis. Improved interference approximation method for preamble-based channel estimation in FBMC/OQAM. In *2011 19th European Signal Processing Conference*, pages 1603–1607, Aug. 2011. 21
- [42] J. P. Javaudin, D. Lacroix, and A. Rouxel. Pilot-aided channel estimation for OFDM/OQAM. In *the 57th IEEE Semiannual Vehicular Technology Conference, 2003. VTC 2003-Spring.*, volume 3, pages 1581–1585 vol.3, Apr. 2003. 21, 24, 33, 39
- [43] C. Lele, P. Siohan, R. Legouable, and J. P. Javaudin. Preamble-based channel estimation techniques for OFDM/OQAM over the powerline. In *2007 IEEE International Symposium on Power Line Communications and Its Applications*, pages 59–64, Mar. 2007. 21
- [44] C. Lele, R. Legouable, and P. Siohan. Channel estimation with scattered pilots in OFDM/OQAM. In *2008 IEEE 9th Workshop on Signal Processing Advances in Wireless Communications*, pages 286–290, Jul. 2008. 22

- [45] W. Cui, D. Qu, T. Jiang, and B. Farhang-Boroujeny. Coded auxiliary pilots for channel estimation in FBMC-OQAM systems. *IEEE Transactions on Vehicular Technology*, 65(5):2936–2946, May. 2016. 22
- [46] Z. Zhao, N. Vucic, and M. Schellmann. A simplified scattered pilot for FBMC/OQAM in highly frequency selective channels. In *2014 11th International Symposium on Wireless Communications Systems (ISWCS)*, pages 819–823, Aug. 2014. 22
- [47] B. Yu, S. Hu, P. Sun, S. Chai, C. Qian, and C. Sun. Channel estimation using dual-dependent pilots in FBMC/OQAM systems. *IEEE Communications Letters*, 20(11):2157–2160, Nov. 2016. 22, 39, 40
- [48] J. M. Choi, Y. Oh, H. Lee, and J. S. Seo. Interference-dependent pair of pilots for channel estimation in FBMC systems. In *2016 IEEE International Symposium on Broadband Multimedia Systems and Broadcasting (BMSB)*, pages 1–4, Jun. 2016. 22
- [49] R. W. Heath, N. González-Prelcic, S. Rangan, W. Roh, and A. M. Sayeed. An overview of signal processing techniques for millimeter wave MIMO systems. *IEEE Journal of Selected Topics in Signal Processing*, 10(3):436–453, April 2016. 22
- [50] Yurong Wang, Xiaochen Xia, Kui Xu, Wei Xie, and Minghai Wang. Channel estimation for FDD massive MIMO system by exploiting the sparse structures in angular domain. *EURASIP Journal on Wireless Communications and Networking*, 2019(1):32, Feb 2019. 22
- [51] Z. Gao, C. Hu, L. Dai, and Z. Wang. Channel estimation for millimeter-wave massive MIMO with hybrid precoding over frequency-selective fading channels. *IEEE Communications Letters*, 20(6):1259–1262, June 2016. 22
- [52] S. Haghghatshoar and G. Caire. Massive MIMO channel subspace estimation from low-dimensional projections. *IEEE Transactions on Signal Processing*, 65(2):303–318, Jan 2017. 22
- [53] X. Luo and X. Wang. How to calibrate massive MIMO? In *2015 IEEE International Conference on Communication Workshop (ICCW)*, pages 1119–1124, June 2015. 23
- [54] G. Soatti, A. Murtada, M. Nicoli, J. Gambini, and U. Spagnolini. Low-rank channel and interference estimation in mm-wave massive antenna arrays. In *2018 26th European Signal Processing Conference (EUSIPCO)*, pages 922–926, 09 2018. 23, 57, 68, 71
- [55] W. C. Huang, C. P. Li, and H. J. Li. On the power allocation and system capacity of OFDM systems using superimposed training schemes. *IEEE Transactions on Vehicular Technology*, 58(4):1731–1740, May 2009. 23

- [56] A. Goljahani, L. Vangelista, and M. Maso. Superimposed technique for OFDM/OQAM based digital terrestrial television broadcasting. In *2008 IEEE 25th Convention of Electrical and Electronics Engineers in Israel*, pages 323–327, Dec 2008. 23
- [57] A. Manolakos, M. Chowdhury, and A. J. Goldsmith. CSI is not needed for optimal scaling in multiuser massive SIMO systems. In *2014 IEEE International Symposium on Information Theory*, pages 3117–3121, June 2014. 24
- [58] A. G. Armada and L. Hanzo. A non-coherent multi-user large scale SIMO system relaying on M-ary DPSK. In *2015 IEEE International Conference on Communications (ICC)*, pages 2517–2522, June 2015. 24
- [59] Yawei Yu, Jianhua Zhang, Mansoor Shafi, Min Zhang, and Jawad Mirza. Statistical characteristics of measured 3-dimensional MIMO channel for outdoor-to-indoor scenario in China and New Zealand,. *Chinese Journal of Engineering*, 2016:10, 2016. 27
- [60] Fjolla Ademaj, Martin Taranetz, and Markus Rupp. 3GPP 3D MIMO channel model: a holistic implementation guideline for open source simulation tools. *EURASIP Journal on Wireless Communications and Networking*, 2016(1):55, Feb 2016. 27
- [61] X. Ge, H. Cheng, G. Mao, Y. Yang, and S. Tu. Vehicular communications for 5G cooperative small-cell networks. *IEEE Transactions on Vehicular Technology*, 65(10):7882–7894, Oct. 2016. 29
- [62] C. Lele, P. Siohan, R. Legouable, and J. P. Javardin. Preamble-based channel estimation techniques for OFDM/OQAM over the powerline. In *2007 IEEE International Symposium on Power Line Communications and Its Applications*, pages 59–64, Mar. 2007. 33
- [63] M. G. Bellanger. Specification and design of a prototype filter for filter bank based multicarrier transmission. In *2001 IEEE International Conference on Acoustics, Speech, and Signal Processing. Proceedings (Cat. No.01CH37221)*, volume 4, pages 2417–2420 vol.4, May. 2001. 33
- [64] Y. R. Zheng and C. Xiao. Channel estimation for frequency-domain equalization of single-carrier broadband wireless communications. *IEEE Transactions on Vehicular Technology*, 58(2):815–823, Feb 2009. 37, 49
- [65] Bennett Eisenberg and Rosemary Sullivan. Why is the sum of independent normal random variables normal? *Mathematics Magazine*, 81(5):362–366, Dec. 2008. 38
- [66] John A. Rice. *Mathematical Statistics and Data Analysis*. Belmont, CA: Duxbury Press., third edition, 2006. 38

- 
- [67] William Feller. *An Introduction to Probability Theory and Its Applications, Vol. 2*, volume Volume 2. Wiley, 2 edition, 1971. 39
- [68] Frank J. Massey. The Kolmogorov-Smirnov Test for Goodness of Fit. *Journal of the American Statistical Association*, 46(253):68–78, 1951. 39
- [69] You-Seok Lee, Hyoung-Nam Kim, Sung Ik Park, and Soo In Lee. Noise reduction for channel estimation based on pilot-block averaging in DVB-T receivers. *IEEE Transactions on Consumer Electronics*, 52(1):51–58, Feb. 2006. 39
- [70] William C. Jakes and Donald C. Cox, editors. *Microwave Mobile Communications*. Wiley-IEEE Press, 1994. 40
- [71] A. Ikhlef and J. Louveaux. An enhanced MMSE per subchannel equalizer for highly frequency selective channels for FBMC/OQAM systems. In *2009 IEEE 10th Workshop on Signal Processing Advances in Wireless Communications*, pages 186–190, June 2009. 41
- [72] V. Monzon Baeza, A. Garcia Armada, W. Zhang, M. El-Hajjar, and L. Hanzo. A non-coherent multi-user large scale SIMO system relying on M-ary DPSK and BICM-ID. *IEEE Transactions on Vehicular Technology*, PP(99):1–1, 2017. 41
- [73] X. Dong, W. s. Lu, and A. C. K. Soong. Linear interpolation in pilot symbol assisted channel estimation for OFDM. *IEEE Transactions on Wireless Communications*, 6(5):1910–1920, May 2007. 47, 49, 52
- [74] M. Wu, B. Yin, G. Wang, C. Dick, J. R. Cavallaro, and C. Studer. Large-scale MIMO detection for 3GPP LTE: Algorithms and FPGA implementations. *IEEE Journal of Selected Topics in Signal Processing*, 8(5):916–929, Oct 2014. 51
- [75] H. Prabhu, O. Edfors, J. Rodrigues, L. Liu, and F. Rusek. Hardware efficient approximate matrix inversion for linear pre-coding in massive MIMO. In *2014 IEEE International Symposium on Circuits and Systems (ISCAS)*, pages 1700–1703, June 2014. 51
- [76] A. J. Al-Askery, C. C. Tsimenidis, S. Boussakta, and J. A. Chambers. Performance analysis of coded massive MIMO-OFDM systems using effective matrix inversion. *IEEE Transactions on Communications*, 65(12):5244–5256, Dec 2017. 52
- [77] Z. Guo, X. Wang, and W. Heng. Millimeter-wave channel estimation based on 2-D beamspace MUSIC method. *IEEE Transactions on Wireless Communications*, 16(8):5384–5394, Aug 2017. 57

- [78] M. Abuthinien, S. Chen, and L. Hanzo. Semi-blind joint maximum likelihood channel estimation and data detection for MIMO systems. *IEEE Signal Processing Letters*, 15:202–205, 2008. 57